

UNIVERSITY OF MIAMI

EXPERIMENTAL AND NUMERICAL INVESTIGATIONS OF A HIGH
PERFORMANCE CO-FLOW JET AIRFOIL

By

Danah Kirk

A THESIS

Submitted to the Faculty
of the University of Miami
in partial fulfillment of the requirements for
the degree of Master of Science

Coral Gables, Florida

December 2009

UNIVERSITY OF MIAMI

A thesis submitted in partial fulfillment of
the requirements for the degree of
Master of Science

EXPERIMENTAL AND NUMERICAL INVESTIGATIONS OF A HIGH
PERFORMANCE CO-FLOW JET AIRFOIL

Danah Kirk

Approved:

Gecheng Zha, Ph.D.
Associate Professor of
Mechanical & Aerospace Engineering

Terri A. Scandura, Ph.D.
Dean of the Graduate School

Hongtan Liu, Ph.D.
Professor of
Mechanical & Aerospace Engineering

Manuel A. Huerta, Ph.D.
Professor of
Physics

Na Li, Ph.D.
Assistant Professor of
Mechanical & Aerospace Engineering

KIRK, DANA H
Experimental and Numerical Investigations of a
High Performance Co-Flow Jet Airfoil

(M.S., Mechanical Engineering)
(December 2009)

Abstract of a thesis at the University of Miami.

Thesis supervised by Professor Gecheng Zha.
No. of pages in text. (156)

The work reflected in this thesis includes a detailed study of co-flow jet (CFJ) technologies as they are applied to a typical thin airfoil, NACA 6415, at take-off and landing speeds. Numerical analysis and experimental testing were conducted on baseline and co-flow jet airfoils of the same plan form. The CFJ mechanism employs high pressure air injected along the span at the leading edge while a low pressure source removes the same amount of air along the span at the trailing edge. Hence, the net mass flux of the system is zero energy loss is minimized. The jet produced along the upper surface of the airfoil mixes with and excites the free stream flow resulting in increased lift, augmented stall margin, and decreased drag. At certain angles of attack the decreased drag is negative and thrust is produced. The research was comprised of four phases including computational fluid dynamics (CFD) simulations, design and manufacturing of a transformable baseline and adjustable slot size CFJ airfoil, implementation of a CFJ Wind Tunnel Laboratory, and wind tunnel testing.

A computational fluid dynamics code, developed at the University of Miami, was used to study flow fields and to obtain analytical results of aerodynamic properties for the baseline and CFJ airfoils. Modeling of both wing shapes utilized the baseline ordinates of a cambered NACA 6415 airfoil. The free stream steady state flow was set

to Mach=0.1 to simulate take-off and landing speeds where the co-flow jet mechanism would demonstrate its largest increase in performance. CFD simulations of both models provided aerodynamic coefficients as well as mass flow and jet effect data specifically useful to the CFJ airfoil.

The NACA 6415 model used for wind tunnel testing was designed and produced to provide both baseline and CFJ results with adjustable injection and suction slot sizes. Connections for a side-mounted force balance and an air delivery system for the co-flow jet were included in the airfoil model. The design and manufacturing of a wind tunnel test section extension was necessary to provide support for the additional aerodynamic loads induced by the CFJ airfoil and to house various air connections and test sensors. A CFJ Wind Tunnel Laboratory was designed and constructed during the course of the research and included selection of proper air delivery apparatus for the injection and suction air for the CFJ jet. All testing controls and sensor equipment were acquired and installed to obtain various data needed for experimental analysis. Finally, a data acquisition system was designed to consolidate all testing information for ease of use. Wind tunnel testing of the baseline and CFJ airfoils provided the aerodynamic loads and coefficients needed to demonstrate the performance enhancements of the co-flow jet flow control method. Experimental and numerical results were examined to understand the benefits of the co-flow jet as it compares to a similar baseline airfoil. The CFD simulations and experimental measurements agree fairly well. All results indicate that the CFJ flow control method is very effective for a typical thin airfoil with 15% maximum thickness.

Acknowledgment

For the countless experiences and invaluable knowledge gained during the course of this work, I would like to sincerely thank my professor and advisor, Dr. Gecheng Zha.

For the guidance and assistance received when faced with numerous tribulations, I would like to express gratitude toward my colleagues in the CFD and Wind Tunnel Laboratories.

For all of the love, blessings, and support, I would like to thank the most selfless and giving people, my parents.

For being my partner, my best friend, and my husband; for willingness to listen and lend words of encouragement; for believing in me, I would like to thank Michael.

This research is supported under ARO/AFOSR Grant 50827-RT-1SP monitored by Dr. Rhett Jefferis, Dr. John Schmisser, Dr. Douglas Smith at AFOSR, Dr. Jenny Haire, and Peggy A. Carewell at ARO.

Contents

List of Figures	vi
List of Tables	x
List of Symbols	xi
Chapter 1:	Introduction
1.0.1 Background	1
1.1 Benefits of Co-Flow Jet as a Flow Control Method	3
1.1.1 Objective	6
Chapter 2:	CFJ Airfoil Design
2.1 External Geometry for Baseline and Co-Flow Jet Airfoils	8
2.2 Internal Geometry for Co-Flow Jet Airfoil	10
2.3 Model Design of Baseline and CFJ Airfoils	15
Chapter 3:	CFD Analysis of Co-Flow Jet and Baseline Airfoils
3.1 Governing Equations	27
3.2 Scheme Selection for CFD Computation	30
3.3 Mesh Generation	30
3.3.1 Original Wind Tunnel Mesh	33
3.3.2 Final Mesh	35
3.4 Initial and Boundary Conditions for CFD	40
3.4.1 Preliminary CFD Initial Conditions	40
3.4.2 Initial Conditions for Final CFD Simulations	41
3.4.3 Boundary Conditions for CFD Simulations	45
3.4.4 Adjusting Mass Flow Rates	46
3.5 Post-Processing of CFD Results	47
3.5.1 Baseline Lift and Drag	47
3.5.2 CFJ Lift & Drag Including Jet Effects	48
3.5.3 Flow Rates and C_μ	50
Chapter 4:	Wind Tunnel Laboratory Design and Setup
4.1 Wind Tunnel Modifications	54
4.2 Air Delivery System	61
4.2.1 Injection Line	63

4.2.2	Suction Line	64
4.3	Sensors and Data Acquisition System	67
4.3.1	Injection Line	68
4.3.2	Test Section and Aerodynamic Forces	73
4.3.3	Suction Line	76
4.3.4	Data Acquisition System and <i>Labview</i>	78
4.4	Uncertainty Analysis	82
Chapter 5:	Results	90
5.1	Numerical Simulations	90
5.2	Experimental Results	111
5.2.1	Comparison of Numerical and Experimental Results	117
5.2.2	Future Work	125
Chapter 6:	Conclusions	126
Appendix A:	Coordinate Generation for Baseline and CFJ Airfoils	128
Appendix B:	Sample Input Files for FASIP code	133
B.1	<i>datain</i> File	133
B.2	<i>init.input</i> File	140
Appendix C:	Flowchart for Lab Equipment, Pip- ing, and Sensors	141
Appendix D:	CFJ Wind Tunnel Laboratory Test- ing Procedure	142
Appendix E:	Wind Tunnel Equipment Operation and Maintenance	146
E.0.1	Compressor: <i>Ingersoll Rand UP6-15c TAS-150</i>	146
E.0.2	Vacuum: <i>Dekker V-max 60 HP VMX1003K</i>	148
Appendix F:	List of Vendors	150
Appendix G:	Drawings for Airfoil Model and Wind Tunnel Modifications	153
References		154

List of Figures

1.1	Profile of Symmetric Airfoil with Co-Flow Jet Implementation	2
2.1	Early Drawing of CFJ Internal Geometry	14
2.2	Final Drawing of CFJ Internal Geometry	14
2.3	Duocel® Aluminum Foam	17
2.4	Side View of CFJ Airfoil	18
2.5	Trimetric View of CFJ Airfoil	19
2.6	CFJ Airfoil Model with Baseline Insert	19
2.7	Endplates for Airfoil Model	20
2.8	Injection Slot Clips	21
2.9	Attachments to Force Balance	22
2.10	Suction Cavity Manifolds and Tubing	23
2.11	CFJ Airfoil and Air Connection assembly	24
2.12	Suction Cavity Manifolds and Tubing	25
2.13	Cavities of Manufactured CFJ Airfoil	25
2.14	Manufactured CFJ Airfoil	25
2.15	Downstream View of Model Mounted in Test Section	25
3.1	Wind Tunnel Mesh of Baseline Airfoil	33
3.2	Wind Tunnel Mesh of CFJ Airfoil	34
3.3	Far Field Mesh	36
3.4	Close View of Baseline Mesh	37
3.5	Close View of CFJ Mesh	37

3.6	Close View of Interior CFJ Blocks	38
3.7	Angles of Injection and Suction Slot for Jet Effects	50
4.1	Aluminum Wall Assembly	55
4.2	Aluminum Wall Plate Connections	55
4.3	Circular Plate for Fitting with Aluminum Wall Assembly	56
4.4	Clamp used for Securing Circular Insert	57
4.5	Modified Test Section Wall Assembly	58
4.6	Wind Tunnel Box	59
4.7	Outer Circle for Wind Tunnel Box with Suction Manifold	60
4.8	Sting Support Piece	61
4.9	Full Wind Tunnel Box Assembly Drawing	61
4.10	Complete Wind Tunnel Box Assembly	62
4.11	Sting Support Piece and Force Balance	62
4.12	Suction Cavity Manifold and Vacuum Hoses	63
4.13	50 CFM Compressor	64
4.14	Pneumatic Computer Controlled Valve	65
4.15	60 Hp Vacuum Pump	65
4.16	Layout of CFJ Wind Tunnel Laboratory	66
4.17	Piping for Air Delivery System	67
4.18	Connection of Injection and Suction Line to Wind Tunnel Box	67
4.19	Overall View of CFJ Wind Tunnel Laboratory	68
4.20	Spectre Sensors Model 1500 Pressure/Temperature Transducer	70
4.21	Spectre Sensors Model D150 Differential Pressure Transducer	70
4.22	Illustration of α Correction Angle	75
4.23	Signal Conditioning Modules	79
4.24	Front Panel of CFJ Wind Tunnel Laboratory Test Stand: Screen 1 .	80
4.25	Front Panel of CFJ Wind Tunnel Laboratory Test Stand: Screen 2 .	81

4.26	Force Balance Calibration Curve, +Fy Direction	83
4.27	Force Balance Calibration Curve, -Fy Direction	83
4.28	Force Balance Calibration Curve, +Fx Direction	84
4.29	Force Balance Calibration Curve, -Fx Direction	84
5.1	Baseline Mach Contours w/Streamlines, $\alpha = 10^\circ$	91
5.2	Baseline 3-D Surface Pressure, $\alpha = 10^\circ$	91
5.3	Baseline 3-D Surface Pressure and 2-D Mach Contours, $\alpha = 15^\circ$. . .	92
5.4	Baseline 2-D Mach Contours w/Streamlines, $\alpha = 15^\circ$	92
5.5	C_L vs. α for All CFD Cases	93
5.6	C_D vs. α for All CFD Cases	93
5.7	C_μ vs. α for All CFD Cases	95
5.8	2-D Mach Contours w/Streamlines, $C_\mu = 0.05$, $\alpha = 0^\circ$	95
5.9	2-D Mach Contours w/Streamlines, $C_\mu = 0.05$, $\alpha = 5^\circ$	96
5.10	2-D Mach Contours w/Streamlines, $C_\mu = 0.05$, $\alpha = 10^\circ$	96
5.11	2-D Mach Contours w/Streamlines, $C_\mu = 0.05$, $\alpha = 15^\circ$	97
5.12	2-D Mach Contours at Injection, $C_\mu = 0.05$, $\alpha = 15^\circ$	98
5.13	2-D Pressure Contours w/Streamlines, $C_\mu = 0.05$, $\alpha = 15^\circ$	99
5.14	3-D Pressure Contours w/ Interior Streamlines, $C_\mu = 0.05$, $\alpha = 15^\circ$.	99
5.15	3-D Surface Pressure and 2-D Mach Contours, $C_\mu = 0.05$, $\alpha = 15^\circ$. .	100
5.16	2-D Mach Contours w/Streamlines, $C_\mu = 0.05$, $\alpha = 18^\circ$	101
5.17	2-D Mach Contours w/Streamlines, $C_\mu = 0.1$, $\alpha = 0^\circ$	102
5.18	2-D Mach Contours w/Streamlines, $C_\mu = 0.1$, $\alpha = 5^\circ$	102
5.19	2-D Mach Contours w/Streamlines, $C_\mu = 0.1$, $\alpha = 10^\circ$	103
5.20	2-D Mach Contours w/Streamlines, $C_\mu = 0.1$, $\alpha = 15^\circ$	103
5.21	2-D Mach Contours w/Streamlines, $C_\mu = 0.1$, $\alpha = 20^\circ$	104
5.22	2-D Mach Contours w/Streamlines, $C_\mu = 0.1$, $\alpha = 25^\circ$	105
5.23	2-D Mach Contours at Injection, $C_\mu = 0.1$, $\alpha = 25^\circ$	106

5.24	2-D Pressure Contours w/Streamlines, $C_\mu = 0.1$, $\alpha = 25^\circ$	106
5.25	3-D Pressure Contours w/ Interior Streamlines, $C_\mu = 0.1$, $\alpha = 25^\circ$. .	107
5.26	3-D Surface Pressure and 2-D Mach Contours, $C_\mu = 0.1$, $\alpha = 25^\circ$. . .	107
5.27	2-D Mach Contours w/Streamlines, $C_\mu = 0.1$, $\alpha = 28^\circ$	108
5.28	Mesh Refinement Results, α vs. C_L	109
5.29	Mesh Refinement Results, α vs. C_D	110
5.30	Mesh Refinement Results, α vs. C_μ	110
5.31	C_L vs. α for All Experimental Cases	111
5.32	C_D vs. α for All Experimental Cases	112
5.33	C_μ vs. α for All Experimental Cases	114
5.34	C_L vs. α with Error Bars	115
5.35	C_D vs. α with Error Bars	116
5.36	Numerical and Experimental Comparison of All Cases, C_L	117
5.37	Numerical and Experimental Comparison Baseline Case, C_L	118
5.38	Numerical and Experimental Comparison of $C_\mu = 0.05$ Case, C_L . . .	118
5.39	Numerical and Experimental Comparison of $C_\mu = 0.1$ Case, C_L . . .	119
5.40	Numerical and Experimental Comparison of All Cases, C_D	120
5.41	Numerical and Experimental Comparison of Baseline Case, C_D	121
5.42	Numerical and Experimental Comparison of $C_\mu = 0.05$ Case, C_D . . .	121
5.43	Numerical and Experimental Comparison of $C_\mu = 0.1$ Case, C_D . . .	122
5.44	Numerical and Experimental Comparison of $C_\mu = 0.05$ Case, C_μ . . .	123
5.45	Numerical and Experimental Comparison of $C_\mu = 0.1$ Case, C_μ . . .	123
5.46	Experimental Drag Polar for All Cases	124
5.47	Numerical Drag Polar for All Cases	124

List of Tables

3.1	Block Allocation for CFJ Airfoil	38
3.2	Block Allocation for Baseline Airfoil	39
3.3	Normalized Initial Conditions for FASIP <i>datain</i> file	41
3.4	Final Inputs for Baseline	43
3.5	Final Inputs for CFJ, $C_\mu = 0.05$	43
3.6	Final Inputs for CFJ, $C_\mu = 0.1$	44
3.7	Scheme Selection for Baseline and CFJ Simulations	45
3.8	C_L and C_D for CFD Baseline Case	48
3.9	Jet Effects and Final C_L and C_D for $C_\mu = 0.05$ Case	50
3.10	Jet Effects and Final C_L and C_D for $C_\mu = 0.1$ Case	51
3.11	Flow Rate Values for $C_\mu = 0.05$ Case	51
3.12	Flow Rate Values for $C_\mu = 0.1$ Case	52
4.1	Sensors and Controls	78
4.2	Uncertainties of Sensor Equipment	82
4.3	Mass Flow Measurement Uncertainties	87
4.4	Jet Velocity Uncertainties	88
4.5	Final Uncertainties for C_L , C_D , and C_μ	89
5.1	Standard Deviations of C_L & C_D , Baseline	115
5.2	Standard Deviations of C_L & C_D , $C_\mu = 0.05$	116
5.3	Standard Deviations of C_L & C_D , $C_\mu = 0.1$	116

List of Symbols

α	angle of attack
α	thermal diffusivity
β	ratio of diameters
$\frac{A}{A^*}$	ratio of area to critical area
γ	ratio of specific heats
μ	viscosity
μ_o	reference viscosity
ν	kinematic viscosity
ρ	density
ρ_∞	free stream density
τ_{ij}	viscous stress tensor
θ	angle in radians, for airfoil geometry
ξ, η, ζ	coordinates for computational domain
A	area
a	speed of sound

A_{jet}	2-D jet area
AoA	Angle of Attack; angle made by an airfoil's chord and the free stream flow
BL	Baldwin-Lomax
C	coefficient of discharge
C_μ	momentum coefficient
C_D	drag coefficient
C_L	lift coefficient
C_M	moment coefficient
CC	Circulation Control
CFD	Computational Fluid Dynamics
CFJ	Co-Flow Jet
CUSP	Convective Upwind and Split Pressure
D	total drag
D_1	large diameter of orifice plate
D_2	small diameter of orifice plate
DES	Direct-Eddy Simulation
DNS	Direct Numerical Simulation
e	expansion coefficient
e	total energy per unit mass
E, F, G	inviscid flux vectors in x , y , and z directions

FASIP	Fluid-Acoustic-Structure Interaction Package, CFD code developed at the University of Miami
FC	Flow Control
HGV	usually in inches, mercury for vacuum pressure
ID	inner diameter
K	constant for isentropic flow equation
L	reference length
L	total lift
L/D	lift to drag Ratio
LE	Leading Edge; on an airfoil
LES	Large Eddy Simulation
LHS	left hand side
\dot{m}	mass flow rate
M	Mach number
m	max ordinate of mean line, for airfoil geometry
MUSCL	Monotone Upstream-centered Schemes for Conservation Laws
n	current time step, for differencing schemes
$n + 1$	next time step, for differencing schemes
NPT	National Pipe Thread
OD	outer diameter

\bar{p}	normalized pressure
p	chordwise position of max ordinate, for airfoil geometry
p	pressure
p_{total}	total pressure
Pr	Prandtl number
Q	vector of conservative variables
Q_x, Q_y, Q_z	heat flux terms in x , y , and z directions
q_x, q_y, q_z	molecular heat flux in x , y , and z directions
R	specific gas constant
R, S, T	viscous flux vectors in x , y , and z directions
R'_x	surface pressure and shear stress integral in x direction
R'_y	surface pressure and shear stress integral in y direction
RHS	right hand side
S	span area
SA	Spalart-Allmaras
STOL	Short Take Off and Landing
\bar{T}	normalized temperature
T	temperature
t	time
T_o	reference temperature

T_{∞}	free stream temperature
T_{cavity}	temperature in injection cavity
T_{ref}	reference temperature for Sutherland's Law
T_{total}	total temperature
TE	Trailing Edge; on an airfoil
U	velocity
u, v, w	velocity components in x , y , and z directions
V_{∞}	free stream velocity
V_{jet}	jet velocity
WCD	Water Column Depth
x	non-dimensional x-coordinate along chord, for airfoil geometry
x, y, z	Cartesian coordinate directions
x_L	x-coordinate of lower surface, for airfoil geometry
x_U	x-coordinate of upper surface, for airfoil geometry
y_c	non-dimensional y-coordinate of mean line, for airfoil geometry
y_L	x-coordinate of lower surface, for airfoil geometry
y_U	y-coordinate of upper surface, for airfoil geometry

Chapter 1

Introduction

1.0.1 Background

Man has always envied the fortunate creatures with natural abilities of flight. The once infinite separation between them has decreased through the 20th century to the present. From the first 852 foot flight achieved by two brothers in a North Carolina field [1] to the maneuverability of the F-22 Raptor, the advancements in flight performance and efficiency have grown exponentially. The global paradigm shift toward more energy and cost efficient solutions must coincide with technological advancements. The work in this thesis thoroughly examines a method to dramatically increase flight performance with very minimal energy expenditure. A flow control method introduced by Zha at the University of Miami has been found to increase lift, decrease drag, and augment stall margin. This flow control method is known as the Co-Flow Jet (CFJ) [2–9].

The Co-Flow Jet method utilizes a high velocity jet injected near the leading edge of an airfoil along the suction surface, while the same amount of air is removed at the trailing edge. The mass flow rates of air entering at the injection slot and exiting at the suction slot are equal, achieving zero net energy loss to the system. The jet is injected tangentially along the suction surface of the airfoil and then mixes

with the free stream flow. This mixing between the turbulent jet and the main flow increases circulation and enhances lift. The jet also provides turbulent diffusion and mixing [2, 3] which allows the main stream flow to overcome the severe adverse pressure gradient and remain attached at higher angles of attack. This provides the CFJ airfoil with increased stall margins as compared to a standard baseline airfoil. Drag reduction is achieved due to super suction provided by the jet near the leading edge and the horizontal component of the jet's reactant force. At certain angles of attack the combination of the super suction effect and the jet's reactant force actually produces negative drag, or thrust. The enhancement of lift, increase in stall margin and reduction in drag are all achieved with minimal energy cost. These performance results are proven both numerically, using computational fluid dynamics (CFD), and experimentally in wind tunnel testing. Fig. 1.1 illustrates the CFJ method as it is implemented into a standard baseline airfoil.

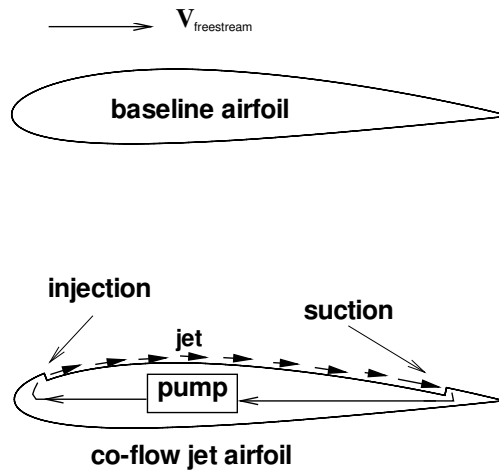


Figure 1.1: Profile of Symmetric Airfoil with Co-Flow Jet Implementation

1.1 Benefits of Co-Flow Jet as a Flow Control Method

The advancement of traditional flight performance can be achieved by using flow control (FC) techniques. Improvements include increased lift, reduction in drag, and suppressed separation which provides increased stall margin. Flow control research has benefits of shorter take off and landing distances (STOL) [10], increased maneuverability, and reduction in fuel consumption in some cases [11]. Various flow control techniques include circulation control (CC) methods using tangential blowing, synthetic jets or pulsed jet separation control, rotating cylinders located at the leading edge and trailing edge, and multi-element airfoils [2–4, 8, 10]. For any flow control method, it is required that the benefits of the new system outweigh the costs or penalties that it will ensue [2]. There are three issues that should be addressed when designing a flow control method including effectiveness of the method, energy efficiency, and ease of implementation [4]. Improvements in lift, higher stall margins and drag reduction are essential for an effective flow control technique. These advancements should have minimal burden on the propulsion system and low impact on the weight of the aircraft. Finally, the FC method should be easily implemented into an existing airfoil or flight system [4]. The application of CFJ as a flow control method allows for greater performance advantages at lower energy costs than other FC methods.

The circulation control method, discussed by Englar, increases lift by enhancing circulation across the low pressure surface of an airfoil. [10] The CC method requires a rounded leading edge (LE) or trailing edge (TE) and utilizes the Coanda effect to keep the flow parallel with the rounded surface and enhance circulation [3, 10]. Even with the increase in lift at low angles of attack (AoA), the rounded LE or TE will have an adverse effect on flight performance during cruise because of the increased drag. Englar states that the CC airfoil is only designed for take off and landing because of the increased drag generated by the rounded TE. Englar proposes

a transformable trailing edge that becomes sharp for cruise flight [10]. This method introduces complex moving parts and control systems. Without LE blowing at higher AoA, the centrifugal force of the jet using the Coanda effect will not be able to stay attached and the stall margin will be reduced. The blunt TE used for the CC method will stall at a lower angle of attack than the same airfoil without CC. The mass flow blowing employed by the circulation control FC method is wasted once it exits the jet. It cannot be recovered and it will have a large hindrance on the propulsion system as an energy loss and will increase fuel consumption during flight [2–4, 8]. An energy analysis provided by Zha and Paxton [6] shows that the loss due to dumping of mass flow is directly proportional to the loss of thrust by the engine. The CFJ, however, utilizes flow from the compressor and can be applied to an airfoil without changing the LE or TE. The shape of the airfoil will stay the same throughout the entire flight and the CFJ can be used during take off, landing, and cruise. The CFJ provides enhanced lift at low and high AoA. Since the CFJ does not rely on the Coanda effect [4], the stall margin will be increased. Furthermore, drag is reduced at take off and landing. At low cruise AoA, negative drag or thrust could be produced. The CFJ method has no moving parts or complex control systems; this will reduce the weight of the aircraft and fuel consumption. The premier benefit of the co-flow jet method is that there is zero mass flux loss from the system. The mass flow rate of jet air that exits at the injection slot is fully recovered by the suction slot. This recirculation of mass flow will insure very minimal energy loss to the propulsion system [2–4, 8]. So far, all CFJ airfoil research has been limited to thick airfoils with 25% maximum thickness.

Another flow control method utilizes rotating cylinders to enhance circulation and therefore lift. This method requires a thick leading edge or trailing edge on the airfoil [8]. Thick airfoils are better suited for low speed flight. If the aircraft design is focused on a thin airfoil for higher speed or supersonic flight, rotating cylinders would be impractical. Also, the motor and control system for driving the cylinders

would increase the payload of the aircraft. The CFJ concept can be applied to any airfoil shape or thickness, providing versatility in its usage to span from low speed commercial flights to supersonic jets. While multi-element airfoils allow for an increase in lift, the moving parts greatly increase the weight of the aircraft. Since the highest lift is required at low speeds, during take off and landing, the noise levels due to the moving flaps will increase. Synthetic jets or pulsed jets are used to minimize the mass flow loss used with CC blowing. This type of system requires a feed back control system and some mechanism to produce the jet. These aspects increase the cost and difficulty of system implementation. Furthermore, this type of jet is weak and when it mixes with the main flow the resulting circulation and turbulent diffusion may not be as dramatic as with the co-flow jet. This produces lower lift augmentation and less attached flow at high angles so the stall margin increase may not be as large as with the CFJ [8].

The co-flow jet as a flow control method provides the benefits of increased lift, stall margin increase, and drag reduction. Lift augmentation is found at both low and high angles of attack using CFJ. This proves that it can be used at take off, landing, and during cruise. Increased lift at lower angles will also provide shorter take off and landing distances. Due to turbulent jet mixing with free stream, the flow will be able to overcome the large adverse pressure gradient and remain attached at higher AoA. This will increase stall margin and improve safety factors for both commercial and military aircraft. Drag reduction and thrust, at some AoA, will be achieved due to super suction provided by the high velocity jet along with the reactant force of the jet's horizontal component. This will greatly increase fuel economy and increase range and endurance of the flight. With the large increase in L/D , it is shown that the co-flow jet has many benefits with minimal energy costs.

1.1.1 Objective

The purpose of this research is to apply the CFJ flow control method to a typical thin airfoil in order to demonstrate its performance enhancement capabilities. This work included the design and manufacturing of a thin co-flow jet airfoil with adjustable slot sizes. CFD analysis was performed for a baseline airfoil and for the CFJ airfoil with two different momentum coefficients, $C_\mu = 0.05$ and $C_\mu = 0.1$. C_μ is a dimensionless parameter that includes mass flow rate and jet velocity and is shown in Eq. (1.1)

$$C_\mu = \frac{\dot{m}V_{jet}}{\frac{1}{2}\rho_\infty V_\infty^2 S} \quad (1.1)$$

where \dot{m} is mass flow rate, V_{jet} is jet velocity, ρ_∞ and V_∞ are free stream density and velocity respectively, and S is the span area of the airfoil. A Co-Flow Jet Wind Tunnel Laboratory was designed and constructed at the University of Miami to obtain experimental CFJ data. The results of the CFD analysis and experimental data are compared to demonstrate the CFJ airfoil performance enhancements. The FASIP (Fluid-Acoustic-Structure Interaction Package) CFD code, developed at the University of Miami CFD Laboratory, was used to obtain numerical results [12–24].

Chapter 2

CFJ Airfoil Design

A thin cambered airfoil was chosen for this research to demonstrate that co-flow jet implementation is possible for any airfoil thickness. Previous studies of wind tunnel experiments and CFD analysis have been done using a NACA 0025 airfoil, which is thicker and symmetric [3, 5, 6, 8, 9, 11]. The NACA 6415 airfoil was chosen in this research for the baseline shape and as a guide for the translation of the suction surface to become a CFJ airfoil. The airfoil has a 12 inch chord length and a 24 inch span. The injection and suction slot heights are measured as the distance of the openings normal to the upper curved surface of the baseline airfoil. The injection and suction slot heights are 0.65% and 1.42% of the chord, respectively. Previous studies show that an injection slot height of this size provides better performance results than a thicker injection slot [3, 8]. The thinner injection slot has a lower mass flow rate and requires less power from the compressor bleed. The suction slot is larger so that the same mass flow expended by the injection slot can be removed by the suction slot without choking, due to the lower static pressure achieved by the vacuum. The name of the CFJ airfoil uses the same 4-digit series number from its NACA origins and includes the injection and suction slot heights. The form is NACA 6415-INJ-SUC, where INJ and SUC are replaced by the injection and suction slot heights

as a percentage of the chord. The resulting airfoil is the CFJ 6415-065-142. The location of the injection and suction slots were also determined from previous works. The injection slot should be located as close to the leading edge as possible but still downstream of the suction peak on the airfoil [6]. This positioning takes advantage of the severe adverse pressure gradient and uses it to promote mixing between the jet at the wall and the main stream flow. The injection and suction slots are located at 7.5% and 88.5% of the chord, respectively. Description of the airfoil design includes exterior coordinate generation for baseline and CFJ airfoils, development of interior cavities required for the CFJ airfoil, and CAD modeling to create an adjustable slot size wind tunnel model with connection to a side mounted force balance.

2.1 External Geometry for Baseline and Co-Flow Jet Airfoils

Coordinate data was used from a NACA 6415 airfoil as the baseline shape of the CFJ airfoil. The coordinates were then used to generate 2- and 3-dimensional models using *SolidWorks 2007* 3-D modeling software. Each number in a NACA 4-digit series airfoil has a specific function to determine the resulting shape. The wing shape begins with a mean line which is then offset with a thickness distribution function for both the upper and lower surfaces of the airfoil. The resulting coordinates give the shape of the wing section. The first digit, 6, is the maximum ordinate of the mean line (largest camber) as a percent of the chord [25]. The second number, 4, is the position of the maximum ordinate or the position of the maximum camber in tenths of the chord. The last two digits, 15, is the maximum thickness of the airfoil in percentage of the chord. The following equations are used to obtain the coordinates of an airfoil and are given by Abbott and Von Doenhoff [25]. The mean line is found using two functions, one for values forward of the max ordinate and one for values

aft. These are shown in Eq. (2.1) and Eq. (2.2) respectively,

$$y_c = \frac{m}{p^2} (2px - x^2) \quad \text{forward of max ordinate} \quad (2.1)$$

$$y_c = \frac{m}{(1-p)^2} [(1-2p) + 2px - x^2] \quad \text{aft of max ordinate} \quad (2.2)$$

where m is the maximum ordinate of the mean line and p is the chordwise position of the maximum ordinate. the non-dimensional chordwise dimension, x varies from 0 to 1 and for the NACA 6415, $m = 6$ and $p = 4$. Next, the thickness distribution is given by Eq. (2.3), where t is the maximum thickness of the airfoil as a percent of the chord length ($t = 15$ for NACA 6415).

$$y_t = \frac{t}{0.20} (0.2969\sqrt{x} - 0.1260x - 0.3516x^2 + 0.2843x^3 - 0.1015x^4) \quad (2.3)$$

Finally, the coordinates of the upper and lower surface of the airfoil can be found using Eq. (2.4) and (2.5) for the upper surface and Eq. (2.6) and (2.7) for the lower surface. Eq. (2.8) shows the value for θ in these equations as the angle slope of the mean line.

$$x_U = x - y_t \sin \theta \quad (2.4)$$

$$y_U = y_c + y_t \cos \theta \quad (2.5)$$

$$x_L = x + y_t \sin \theta \quad (2.6)$$

$$y_L = y_c - y_t \cos \theta \quad (2.7)$$

$$\theta = \tan^{-1} \left(\frac{dy_c}{dx} \right) \quad (2.8)$$

These equations give coordinates for the baseline shape of a NACA 6415 airfoil.

The co-flow jet slots were generated from the baseline coordinates. The upper surface was translated downward to create the CFJ geometry. Since the injection and suction slot have different thicknesses, two translations were made and a resulting surface was created by blending the two together. Each y-coordinate was generated by introducing a rotation angle between each point. The resulting blended surface became the suction surface of the CFJ airfoil. The original translated surfaces were simply shifted vertically downward by the thickness of the injection and suction slot. The coordinates for the baseline NACA 6415 and the CFJ 6415-065-142 airfoil are given in Appendix A. Plots of the baseline NACA 6415, the two translated surfaces for the injection and suction slots, and the final CFJ airfoil cross section are also included.

2.2 Internal Geometry for Co-Flow Jet Airfoil

With the exterior profiles of the baseline and CFJ airfoils complete, the internal ducting for the injection and suction cavities were created. The shapes of the interior curves were driven by three factors: the minimum area required for flow without being choked, internal aerodynamic characteristics, and ease of machining. Since air will be supplied to and removed from the airfoil to create the co-flow jet, the internal cavities needed to have large enough areas so that there would be no choked flow and the mass flow rates could be controlled for various tests. The internal features should include

aerodynamic shapes for the most effective use of high pressure air to generate the jet. Throughout the design of the model, manufacturing capabilities were considered to ensure that the final airfoil would be easy to machine without complicated and costly features.

Certain parameters were given as requirements for the experimental design. The Baseline and CFJ models would be used in the wind tunnel test section to acquire critical data for experimental airfoil testing. The entire research including model design, CFD analysis, laboratory design and set up, and collection of wind tunnel data was based on these parameters. The free stream velocity for CFD and experimental testing was $M = 0.1$ and the air delivery system was designed for a maximum of $C_\mu = 0.4$. The entire CFJ testing system was designed with these two input values. The minimum areas required for the injection and suction cavities without choke can be found from these values as well. Before CFJ testing began, some assumptions were made for measured values that would be collected from experimental data. The jet velocity (V_{jet}) exiting the injection cavity was taken as three times the free stream flow. This approximation comes from previous CFD simulations and CFJ testing done on a different airfoil. The maximum mass flow rate required at the given C_μ is found. The momentum equation is rearranged to solve for mass flow rate and V_{jet} is replaced with $3 \cdot V_\infty$.

$$\dot{m} = \frac{C_\mu \frac{1}{2} \rho_\infty V_\infty^2 S}{V_{jet}} \quad (2.9)$$

$$V_\infty = M \cdot a \quad (2.10)$$

$$a = \sqrt{\gamma R T} \quad (2.11)$$

In Eq. (2.9), (2.10), and (2.11), all values are used as standard ambient conditions

at sea level where $\rho_\infty = 1.23 \text{ kg/s}$, $V_\infty = 34.55 \text{ m/s}$, $T = 297.04 \text{ K}$ or 75° F , and $R = 287.06 \text{ J/(kg} \cdot \text{K)}$. Using the above equations and the given inputs for Mach number and C_μ , the resulting maximum mass flow rate is $\dot{m} = 0.5264 \text{ kg/s}$. The minimum 2-D injection cavity area is then found using Eq. (2.12). Here, the mass flow rate is the same value found from Eq. (2.9) with the maximum value of $C_\mu = 0.4$. The velocity in Eq. (2.12) uses velocity right before choke, when $M = 0.95$. The density varies depending on the total pressure and temperature in the cavity. For the current calculation, density comes from a maximum cavity total pressure of 80 psi (551.6 kPa) and ambient temperature of 75° F (23.9° C). In the injection cavity, the pressure will increase as C_μ increases. Also, the increased \dot{m} will require higher pressure. The pressure can be regulated by controlling the amount of flow entering the cavity from the air delivery system. This control will be discussed in later sections regarding laboratory equipment selection for air systems. The minimum 2-D area for the injection cavity is therefore not as critical as the minimum area for the suction cavity, because the pressure will increase as mass flow increases on the injection side. As air flows out of the holding tank at high mass flow rates, the decrease in temperature will not be of concern because the high pressure will mediate the density and maintain the minimum area required. A worst case scenario combination of pressure and temperature was chosen to find density and ultimately find the minimum injection area. Eq. (2.13) is the state equation for an ideal gas as it is solved for density. The minimum area was found to be 0.3843 in^2 ($2.479 \times 10^{-4} \text{ m}^2$) for the injection cavity.

$$\dot{m} = \rho V A \quad (2.12)$$

$$\rho = \frac{p}{RT} \quad (2.13)$$

The same method is used to find the minimum area required in the suction cavity. The same mass flow rate was used from Eq. (2.9), however the density used for Eq. (2.12) was different. Since the mass flow on the suction side is the result of a low pressure source, the pressure and temperature are not as easily controlled. Ambient temperature ($T = 75^{\circ}F$ or $23.9^{\circ}C$) and a low pressure ($P = 10$ psia or 68.9 kPa) were chosen to calculate the minimum 2-D area required in the suction cavity. The minimum area corresponding to the highest mass flow rate with $C_{\mu} = 0.4$ was found to be 3.0738 in^2 ($1.983 \times 10^{-3} \text{ m}^2$).

Another factor driving the geometry of the injection and suction cavities are the aerodynamic characteristics of the internal structure. It was important to have negligible losses, if any, from the flow entering the inside of the airfoil to the jet exiting the injection slot. This would allow for the most accurate mass flow, pressure, and temperature readings across the slot. It would also increase the efficiency of the air delivery system so that all streamlines entering the cavity would exit without forming any eddies or stagnation points. This was achieved by performing 2-dimensional CFD analysis of the internal structures and the jet of the CFJ 6415-065-142 airfoil. The cavities were drawn in *SolidWorks* using splines that followed the desired internal shape for the cavities. Results of the CFD analysis showed streamlines inside the cavities. These provided a visualization of the flow and any internal stagnation points or eddies were apparent. Then the geometry could be adjusted accordingly. Many iterations of this process led to the final internal ducting of the airfoil that allowed the flow to turn effectively and exit the jet outlet and enter at the suction slot smoothly without any aerodynamic losses. Fig. 2.1 illustrates the 2-D sketch of one of the first iterations of the internal CFJ airfoil geometry.

The final consideration for the internal design of the CFJ 6415-065-142 airfoil was its ability to be machined. Several methods of manufacturing and material selections were explored for the model. Machined aluminum was chosen as the final

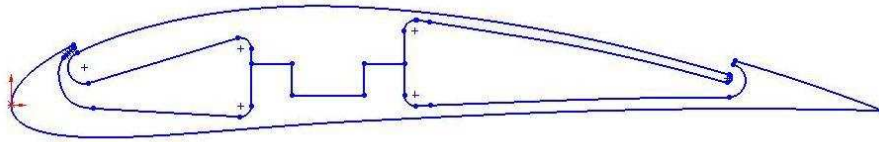


Figure 2.1: Early Drawing of CFJ Internal Geometry

manufacturing decision due to the material's shear and compressive strengths and malleability. Computer Numerically Controlled (CNC) machining was chosen as the means of manufacturing because of the complex curves of the airfoil's surface and internal geometry. Standard machining could not accurately achieve the desired results. By adjusting the internal ducting of the airfoil and removing excess material where possible, the cost of CNC work was decreased. The thin edges at the injection and suction slots were made to a thickness within reason, leaving enough material to be stable. Fig. 2.2 shows the final 2-D sketch for the internal geometry of the CFJ 6415-065-142 airfoil.

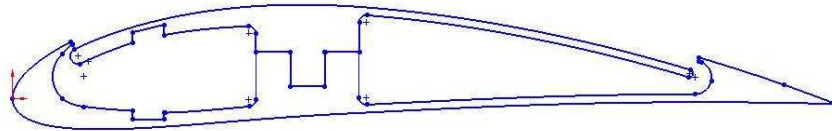


Figure 2.2: Final Drawing of CFJ Internal Geometry

The changes made from the original design can be seen in this drawing. The solid section in the center of the airfoil connecting the injection and suction cavities was made thinner to reduce material and the model's weight. The larger area in the injection cavity was used for the air delivery apparatus and the force balance mounting. These features and others are discussed further in the next section. The upper section of the injection cavity was also made thinner for the same reasons. In addition, the converging area leading to the jet was made with a lower slope and the curving walls that turn the flow were made with a larger radius so that all streamlines could easily exit the jet without forming internal stagnation points. The cut-outs in the injection

cavity are for the placement of Duocel® aluminum foam. Since the air enters the CFJ airfoil from the side, the foam is essential to make the flow uniform as it exits the jet. This is also discussed in later sections.

2.3 Model Design of Baseline and CFJ Airfoils

Once the external curves and internal cavities were generated as a 2-dimensional sketch, the 3-dimensional models of the baseline and CFJ airfoils were created. The model was made as an extrusion of the 2-D sketch in the z-direction. The model's geometry remained constant in the span wise direction of the airfoil. For the purpose of this research, both models were designed to provide 2-D results in the wind tunnel test section so that wing tip vortices and cross flow would be negligible. The design parameters were set to include adjustable injection and suction slot sizes within one entire model, use of aluminum foam for uniform flow, incorporation of the baseline and CFJ airfoil within one model, a side mounted connection to the force balance, and incorporation of the air delivery and removal from the same side as the force balance. The model had a chord length of 12 inches and a span length of 23.75 inches. The wind tunnel test section that the model was designed for is 24" (0.6096 m) high, 24" (0.6096 m) wide, and 48" (1.2192 m) long. The span wise dimension of the model was reduced from the original 24" (0.6096 m) to 23.75" (0.60325 m) to allow for a 0.125" ($.3175\text{ cm}$) gap on either side of the model to avoid wall interference during testing.

The first design element to be implemented was the adjustable slot size feature. To achieve this, the suction surface of the CFJ airfoil and the lower surface were made as two parts. By inserting shims with a fixed thickness, the slot distance perpendicular to the chord could be decreased. The cut separating the parts is parallel to the chord, or horizontal. This will allow the top of the CFJ airfoil to be adjusted in one direction only, the y-direction. The cut was made as a step feature to reduce the movement of

the top surface by one degree of freedom (x-direction restraint), and the endplates of the model will prevent movement in the z-direction. The top and bottom sections of the model are secured together by screws, entering through the bottom and tapping into the top. These screws are placed along the span of the model. The largest slot sizes for the injection and suction openings are the dimensions given by the CFJ 6415-065-142 airfoil. Stainless steel shims with 0.012" (0.63048 *mm*) thickness will be used to adjust the slot heights.

Since high pressure air will fill the injection cavity before it escapes at the jet outlet, it was important to ensure that the thin cantilevered extrusion making up the top of the injection cavity would not flex out of place under the load of the high pressure air. As mentioned previously, aluminum foam was used to make the flow uniform across the span since it enters at the side of CFJ. This foam was also used as a support for the cantilevered surface. Screws were placed along the span, through the suction surface and into the foam with threaded inserts. The foam was held in place in the x-direction by the cut-outs shown in Fig. 2.2, in the z-direction by the airfoil endplates, and in the y-direction by screws through the upper and lower surface of the airfoil. The cut-out for the foam in the lower surface is deep enough for several 0.012" (0.63048 *mm*) shims to be layered for slot size adjustment. The Duocel® aluminum foam was purchased from ERG Materials and Aerospace Corporation, and has 40 ppi, 6 – 8% density 6101-T6 aluminum, and is compressed to 35% nominal density. This foam was used for the results included in the current research. A 50% density foam was also ordered to use for future testing. Fig. 2.3 shows one of the 35% density Duocel foam pieces used.



Figure 2.3: Duocel® Aluminum Foam

A cantilevered surface also exists in the suction cavity. Since there will be a localized low pressure in this cavity from a vacuum system, the thin surface needs to be supported to prevent collapse. Small supports were made for this cavity and they attach from the bottom with screws. The top surfaces of these supports follow the same spline shape as the curvature of the surface itself, in order to provide a good fit. There are three suction supports along the span of the airfoil. In Fig 2.4 the aluminum foam and suction supports are shown in the injection cavity and suction cavity respectively. They are transparent so that the fasteners can be seen. For the adjustable slot size airfoil, shims will also be placed under each suction support to assist in maintaining the desired suction slot distance. Near the trailing edge, another cut was made so that the upper lip of the suction opening could be removed. In Fig. 2.4 this part is green. This additional cut allows for simple assembly of the airfoil and ease of CNC machining by decreasing the amount of concave curves. Like the top and bottom sections of the airfoil, this piece also has a stepped cut to remove movement in the x-direction. This piece is secured from the bottom part of the model with screws along the span of the airfoil.

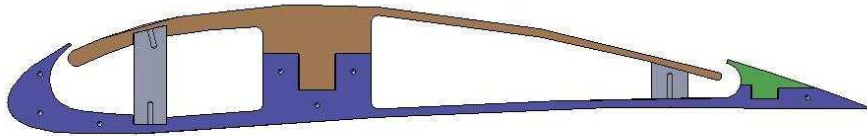


Figure 2.4: Side View of CFJ Airfoil

The lower section of the airfoil is shown blue in Fig. 2.4, and the top piece is tan. Fig. 2.5 shows another view of the CFJ airfoil without endplates, where screw holes for the aluminum foam are visible across the span of the airfoil.

In order to minimize cost of the model's manufacturing, the baseline NACA 6415 and the CFJ 6415-065-142 airfoils were incorporated into one interchangeable model. Since the CFJ airfoil is simply the baseline airfoil with a lowered suction surface, a

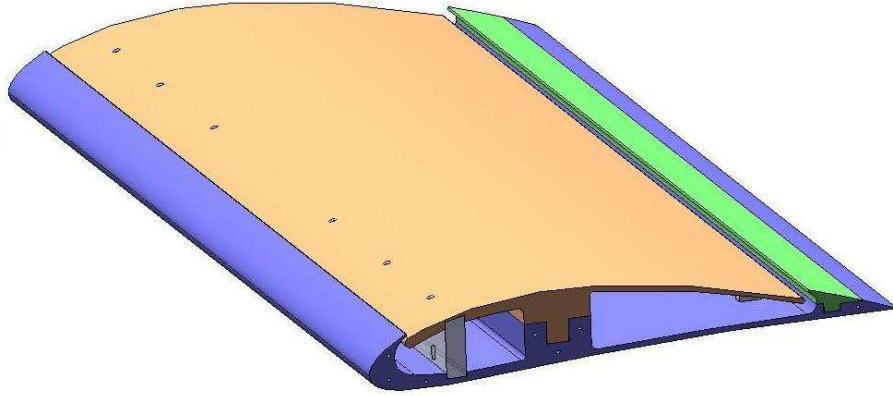


Figure 2.5: Trimetric View of CFJ Airfoil

part was made to fill in the empty area and close off the injection and suction slots. The baseline insert part is easily added to the CFJ airfoil by sliding it in at the side and securing it into the top section with screws along the span of the model. The baseline insert is shown in Fig. 2.6 as the gray part filling the CFJ slot. The side view of the model with the insert will make the profile of a NACA 6415 airfoil.

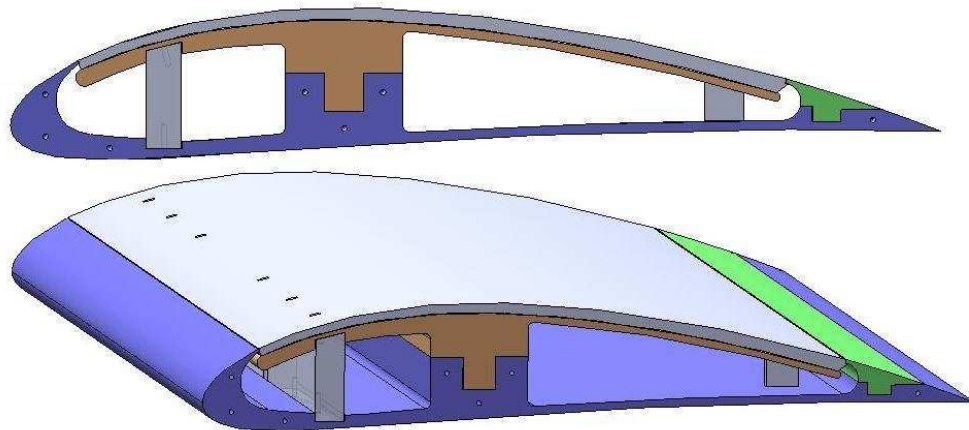


Figure 2.6: CFJ Airfoil Model with Baseline Insert

To close the cavities off at the ends of the airfoil and to provide a connection to the force balance and air systems, endplates were added to the model. A 0.25" thick endplate was placed at each end of the model. One end has a solid endplate and one has an endplate with a connection to the force balance and an opening for a manifold connection to the vacuum system. In Fig. 2.7, the upper drawing is the plain endplate

and the lower one is the endplate with balance and air connections.

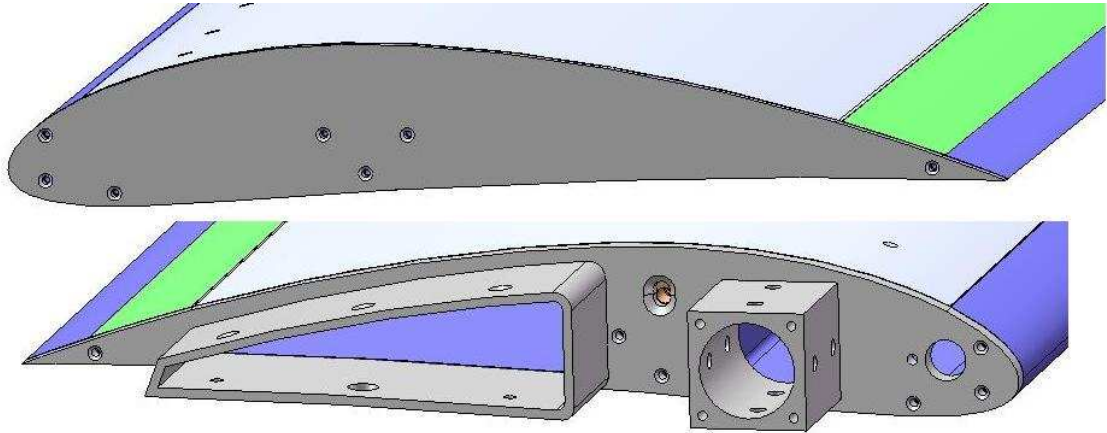


Figure 2.7: Endplates for Airfoil Model

Each endplate is secured to the model with screws. The endplate with force balance connection must support the aerodynamic loads felt by the airfoil. This endplate is secured to the airfoil with an additional larger screw into the material filled center of the model. The through hole on the endplate is slotted so that it can still be attached properly when the injection and suction slot sizes are changed. This can be seen in Fig. 2.7.

To ensure that the injection slot size will remain constant under the high pressure loads inside the cavity during testing, a small spacer was designed. These spacers, or clips, are inserted at the side of the airfoil before the endplate is added. Three or four clips are slid along the span of the airfoil and are held in place by their geometry. This is shown in Fig. 2.8.

The square extrusion on the endplate is where the model will connect to the force balance and where the high pressure injection air will enter the cavity. It is important for this connection be as rigid as possible and be the only connection that will have reactant forces on the airfoil during testing. This is to ensure that the readings for lift, drag, moments, etc. are as accurate as possible. The center of this part is located at the quarter chord of the airfoil so that the pitching moments from the force balance

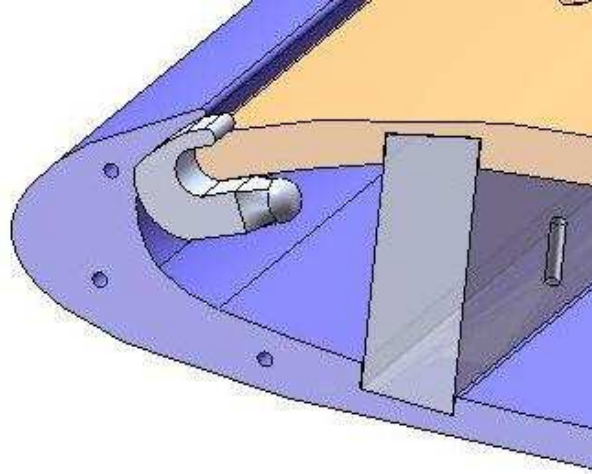


Figure 2.8: Injection Slot Clips

do not have to be re-calculated. The holes on this part are tapped holes where set screws will be used to secure the model in place. The airfoil does not connect to the balance directly as there is an intermediate piece, called the sting, that attaches to the balance. There are grooves in the sting that correspond to the set screws connections from the airfoil for more secure attachment. The force balance will be discussed in more detail further on. The sting is a hollow tube that also delivers air into the injection cavity. This stainless steel tube has an OD of 1.00" (2.54 *cm*) and an ID of 0.75" (1.905 *cm*). The 2-D choke area analysis from section 2.2 also applies to this area for flow. The distance of the extrusion in the z-direction needs to be long enough to reach through the wind tunnel wall. After the original design, an additional part was made to extend this length. This is discussed further in the section titled *Wind Tunnel Modifications*. This part, along with the sting, was machined in house and is called the sting coupler. It attaches to the existing extrusion with screws and has additional set screws for airfoil attachment to the sting. The sting and the sting coupler are shown in Fig. 2.9. The flange on the sting has a bolt pattern of thru holes that matches the bolt pattern of tapped holes on the force balance. The force balance is attached as close to the model as possible so that accurate yaw and roll moments (moments about the y- and x-axis) are read by the strain gauges. Due to

the wind tunnel modifications discussed later, an additional part was made to make the balance rigid on one side. This part, called the sting extender, was also made in-house and is shown in Fig. 2.9

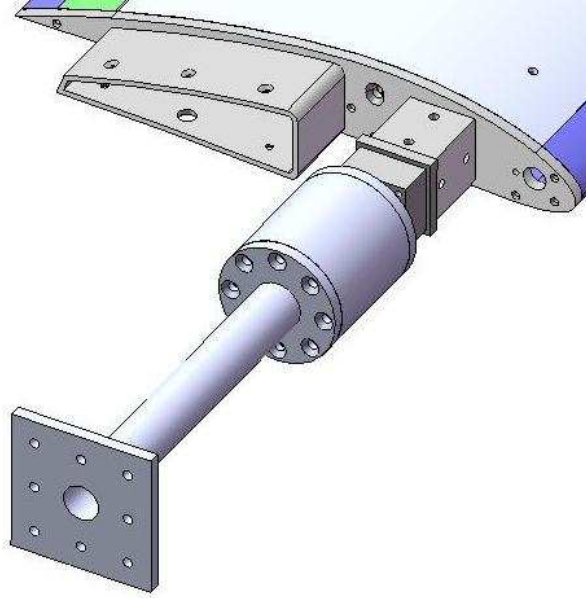


Figure 2.9: Attachments to Force Balance

To achieve equal mass flow rates exiting and entering each cavity in the CFJ airfoil, a vacuum is required to remove the air from the suction cavity. The outlet of the section cavity is an extruded shell feature that will lead to the suction line, and can be seen in Fig. 2.7. A manifold was designed to attach the curved suction outlet to three tubes that will lead to the vacuum line. The tubes are made of flexible vacuum tubing so that they will not translate any forces onto the airfoil during testing. The 2-D areas of both of these features follow the minimum area for choke as required in section 2.2. Another manifold was designed to connect the three tubes to the larger main suction line. Fig 2.10 shows the manifold joining the suction cavity to the tubes and the manifold joining the tubes to the main suction line. The ID of the tubes allows for a snug fit over the OD of the manifold tube connections. These tubes are held in place with hose clamps and the holes in the manifolds are for screws.

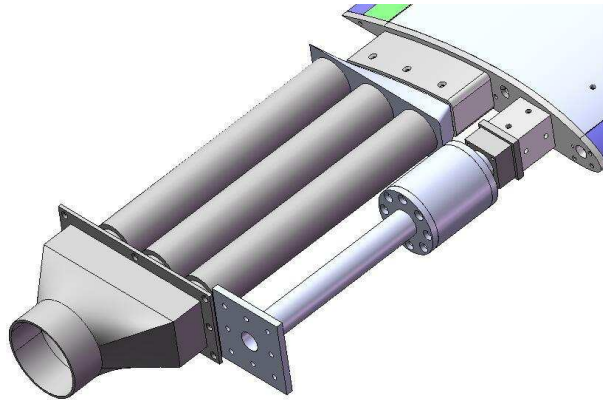


Figure 2.10: Suction Cavity Manifolds and Tubing

The large hole located in the endplate near the leading edge is a 1/4 NPT tap for the connection of a pitot tube for measurement of total pressure in the injection cavity. This and other test sensors are discussed later. The smaller hole that is located just aft of the NPT is an opening for a J-type thermocouple that will measure the temperature in the cavity.

All parts of the airfoil model itself are CNC machined from 6061 aluminum. This material was chosen because of its rigidity and tensile strength to support the aero-

dynamic loads and moments felt during testing and the internal forces produced by the high pressure jet air. Other options for manufacturing were explored, including SLA and 3-D printing, however the machined metal was chosen based on the model's size, the material's properties, the surface finish achieved, and the strength of the thin features in the model. The two manifolds used to connect the airfoil to the suction line were manufactured using SLA (stereo lithography) prototyping. These parts were not load bearing and the complexity of their geometry made them excellent candidates for SLA prototyping. The CNC machined airfoil parts and the SLA prototyped manifolds were made by Solid Concepts. The sting and the sting extender, connecting the airfoil to the force balance, were made with stainless steel tubing and plates for the flanges. These parts were machined in-house and welded to the flanges. Stainless steel was chosen to make these parts as rigid as possible, since they will bear the entire load from the model.

The CFJ airfoil and the connections to the air system are shown in their entirety in Fig. 2.11. Fig. 2.12 shows all of the parts in the airfoil assembly in an exploded view, to show how they are assembled. Fig. 2.13 shows the interior cavities of the manufactured airfoil model. Fig. 2.14 and 2.15 show the final model mounted in the test section.

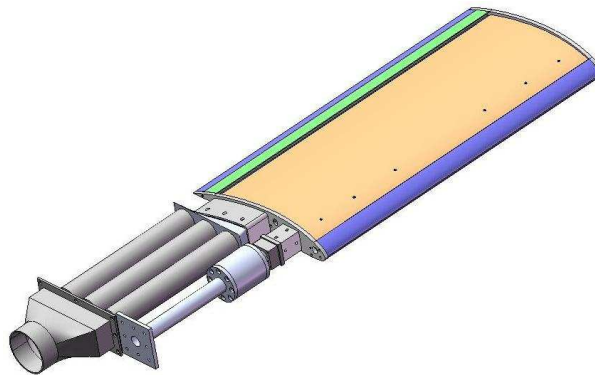


Figure 2.11: CFJ Airfoil and Air Connection assembly

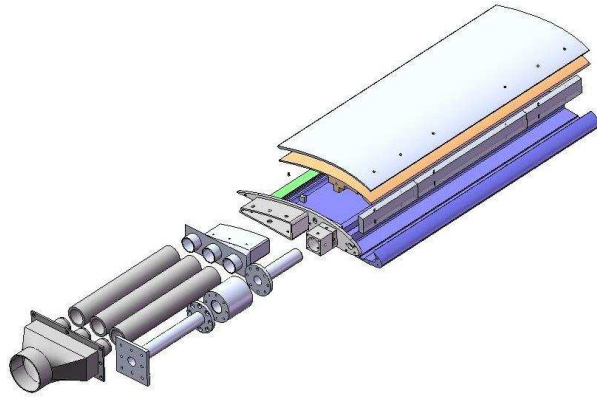


Figure 2.12: Suction Cavity Manifolds and Tubing



Figure 2.13: Cavities of Manufactured CFJ Airfoil



Figure 2.14: Manufactured CFJ Airfoil

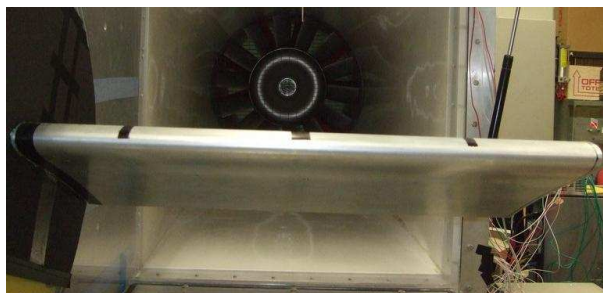


Figure 2.15: Downstream View of Model Mounted in Test Section

Chapter 3

CFD Analysis of Co-Flow Jet and Baseline Airfoils

To obtain cost and time effective solutions to fluid flow problems, initial results can be obtained from numerical methods. Computational fluid dynamics, or CFD, is an iterative process that numerically solves non-linear, partial differential Navier-Stokes equations for fluid flow. For this research, the FASIP (Fluid-Acoustics-Structure Interaction Package) CFD code was used. This code was developed at the University of Miami CFD Laboratory under the supervision of Dr. Gecheng Zha [12–23]. For this research, the FASIP code was used as a tool to obtain results including pressure distributions, velocity profiles, streamlines, and non-dimensional aerodynamic coefficients such as C_L , C_D , and C_μ . All results were acquired from 3-dimensional, steady-state simulations of the NACA 6415 baseline airfoil and the CFJ 6415-065-142 airfoil at $C_\mu = 0.05$ and 0.1 . For each case, CFD analysis was performed for a broad range of angles of attack, from $\alpha = 0$ to $\alpha = \text{stall angle}$. Use of the FASIP CFD code requires meshing of the flow field, input of initial conditions and boundary conditions, and post processing of the acquired results.

3.1 Governing Equations

Navier Stokes Equations are the governing equations for fluid flow problems. CFD utilizes numerical methods to solve these non-linear partial differential equations. The general 3-dimensional Navier Stokes equation is shown in conservative form in Eq. (3.1).

$$\frac{\partial \mathbf{Q}}{\partial t} + \frac{\partial \mathbf{E}}{\partial x} + \frac{\partial \mathbf{F}}{\partial y} + \frac{\partial \mathbf{G}}{\partial z} = \frac{\partial \mathbf{R}}{\partial x} + \frac{\partial \mathbf{S}}{\partial y} + \frac{\partial \mathbf{T}}{\partial z} \quad (3.1)$$

In the above equation, \mathbf{Q} is the vector of conservative variables; \mathbf{E} , \mathbf{F} , and \mathbf{G} are the inviscid flux vectors for flux in the x , y , and z directions respectively; and \mathbf{R} , \mathbf{S} , and \mathbf{T} are the viscous terms.

$$\mathbf{Q} = \begin{pmatrix} \rho \\ \rho u \\ \rho v \\ \rho w \\ \rho e \end{pmatrix} \quad (3.2)$$

$$\mathbf{E} = \begin{pmatrix} \rho u \\ \rho u^2 + p \\ \rho uv \\ \rho uw \\ \rho (\rho e + p) u \end{pmatrix}, \mathbf{F} = \begin{pmatrix} \rho v \\ \rho vu \\ \rho v^2 + p \\ \rho vw \\ \rho (\rho e + p) v \end{pmatrix}, \mathbf{G} = \begin{pmatrix} \rho w \\ \rho wu \\ \rho wv \\ \rho w^2 + p \\ \rho (\rho e + p) w \end{pmatrix} \quad (3.3)$$

$$\mathbf{R} = \begin{pmatrix} 0 \\ \tau_{xx} \\ \tau_{xy} \\ \tau_{xz} \\ Q_x \end{pmatrix}, \mathbf{S} = \begin{pmatrix} \tau_{yx} \\ \tau_{yy} \\ \tau_{yz} \\ Q_y \end{pmatrix}, \mathbf{T} = \begin{pmatrix} \tau_{zx} \\ \tau_{zy} \\ \tau_{zz} \\ Q_z \end{pmatrix} \quad (3.4)$$

In these equations, ρ is the density; u , v , and w are the velocity components in the x , y , and z directions respectively; p is the pressure; and e is energy per unit mass. All aspects of fluid flow can be solved from these variables. In Eq. (3.4), the terms Q_x , Q_y , and Q_z are the heat flux terms and are functions of shear stress and velocity components. Eq. (3.5) shows these expanded terms and Eq. (3.6) shows the heat flux in the x , y , and z directions.

$$\begin{aligned} Q_x &= u\tau_{xx} + v\tau_{xy} + w\tau_{xz} - q_x \\ Q_y &= u\tau_{xy} + v\tau_{yy} + w\tau_{yz} - q_y \\ Q_z &= u\tau_{xz} + v\tau_{yz} + w\tau_{zz} - q_z \end{aligned} \quad (3.5)$$

$$\begin{aligned} q_x &= -\frac{\mu}{(\gamma-1)Pr} \frac{\partial a^2}{\partial x} \\ q_y &= -\frac{\mu}{(\gamma-1)Pr} \frac{\partial a^2}{\partial y} \\ q_z &= -\frac{\mu}{(\gamma-1)Pr} \frac{\partial a^2}{\partial z} \end{aligned} \quad (3.6)$$

In the above equation, Pr is the Prandtl number and is defined as follows where ν is kinematic viscosity, α is the thermal diffusivity in this case, and γ is the ratio of specific heats.

$$Pr = \frac{\nu}{\alpha} \quad (3.7)$$

The viscous shear stress terms from Eq. (3.5) are shown as follows.

$$\begin{aligned}
\tau_{xx} &= \frac{2}{3}\mu \left(2\frac{\partial u}{\partial x} - \frac{\partial v}{\partial y} - \frac{\partial w}{\partial z} \right) \\
\tau_{yy} &= \frac{2}{3}\mu \left(2\frac{\partial v}{\partial y} - \frac{\partial u}{\partial x} - \frac{\partial w}{\partial z} \right) \\
\tau_{zz} &= \frac{2}{3}\mu \left(2\frac{\partial w}{\partial z} - \frac{\partial u}{\partial x} - \frac{\partial v}{\partial y} \right) \\
\tau_{xy} &= \tau_{yz} = \mu \left(\frac{\partial u}{\partial y} - \frac{\partial v}{\partial x} \right) \\
\tau_{xz} &= \tau_{zx} = \mu \left(\frac{\partial w}{\partial x} - \frac{\partial u}{\partial z} \right) \\
\tau_{yz} &= \tau_{zy} = \mu \left(\frac{\partial v}{\partial z} - \frac{\partial w}{\partial y} \right)
\end{aligned} \tag{3.8}$$

The first terms in Eq. (3.2), (3.3), and (3.4) form the Continuity Equation, or conservation of mass. The 2nd through 4th terms make up the u , v , and w directions of the Momentum Equation. Finally, the 5th term makes up the Energy Equation. All of these equations together can be solved simultaneously using various differencing schemes by CFD. From this, the density, velocity in three directions, pressure, and energy can be found at every point within the discretized space.

Turbulence modeling of fluid flow is very complex and much work has been done in the field to accurately capture this chaotic and seemingly unsolvable phenomenon. However, there are many approximation methods that are shown to have accurate results. These turbulence models include algebraic solving, one-equation, two-equation, Large Eddy Simulation (LES), Direct-Eddy Simulation (DES), and Direct Numerical Simulation (DNS) [26–28]. The FASIP CFD code is equipped with solvers for the algebraic Baldwin-Lomax (BL) model, the one-equation Spalart-Allmaras (SA) model, LES, and DES. For this work, the BL turbulence model is used with Reynolds averaged Navier-Stokes equations for their robustness and high CPU efficiency. This model is often used when the turbulent boundary layer is very thin compared to the overall geometry and the discretized cell size along the wall is small. Such applications include the aerodynamic modeling of wings.

3.2 Scheme Selection for CFD Computation

The main purpose of this work is to compare experimental wind tunnel results with numerical CFD analysis of a Co-Flow Jet Airfoil. This will not only demonstrate the many aerodynamic benefits of the CFJ flow control method, but it will also assist in validation of the FASIP CFD code for use with airfoils and to produce accurate aerodynamic force simulation. This CFD package uses implicit schemes, which are unconditionally stable and can be proven so via Von Neumann analysis. This means that the unknowns exist in time step $n + 1$ and they are solved simultaneously for every solution point in that time step [28]. The FASIP code is equipped with several differencing schemes that can be applied to the equations for different orders. The higher the order of the equation, the more accurate the results will be because the truncation error is reduced when more terms are included in the calculations. For each case of simulations for the baseline and CFJ airfoil the same schemes and orders are used. The Zha3 Low Diffusion E-CUSP (Convective Upwind and Split Pressure) scheme is used for the right hand side (RHS) of the interface equation [18,19,23,26,27]. This scheme utilizes vector splitting of the inviscid flux terms into convective and pressure parts. For this scheme, the inviscid fluxes were evaluated using 3rd order accuracy. The viscous terms are found using 2nd order central differencing. The Van Leer Scheme was used to evaluate the implicit left hand side (LHS) with a 1st order MUSCL scheme (Monotone Upstream-Centered Schemes for Conservation Laws) to enhance diagonal dominance.

3.3 Mesh Generation

For any CFD code simulation, the first task is to generate a mesh within the flow field. The FASIP code is no exception. Sometimes the space will contain the geometry of a solid body that will interact with the flow. In the case of this research, the free

stream flow field contains baseline and CFJ airfoils. If the solution space can be reduced to a single point, then the mesh within that space is considered simply-connected. However, if there is a geometry enclosed within the mesh and the space is not reducible, the mesh is called doubly-connected [27]. Such is the case for this work.

There are various shapes available for mesh discretization, such as triangles, rectangles, and hexagons. For this work, each cell is rectangular. For 2-dimensional meshing each cell has 4 node points at the corners and for 3-dimensional meshes each cell has eight node points. The CFD simulation performed on the NACA 6415 baseline and the CFJ 6415-065-142 airfoils is 3-dimensional. Since the solution points are found from a finite volume method at the center of each cell, the accuracy of the results are dependent on the size of each mesh cell. A finer mesh will produce higher accuracy than a more coarse mesh, however the fine mesh will also increase CPU time. This is a trade off that varies with each case and depending on the type of results required. In general, when there is a large flow gradient with more complex flow interaction and higher turbulence, the mesh should be finer. For this reason, the mesh size at wall boundaries is much finer than further out in the flow field. Also, since the purpose of this work is to produce aerodynamic force coefficients, the pressure distributions and velocities near the airfoil surface is more important than the far field. If a mesh is very large, CPU time can be reduced by splitting the mesh into sections and running them simultaneously using an MPI (Message Passing Interface) parallel computing process. The FASIP code is used to easily accomplish this [14].

The mesh that fits the actual solution space is often built around complicated geometries, depending on the application. The position of each node is assigned a real coordinate in Cartesian space. This is referred to as the physical domain and has values for each x , y , and z coordinate. The physical domain needs to be transformed into a rectangular shape for CFD analysis and this is called the computational domain

with coordinates ξ , η , and ζ [27]. This allows the original physical domain with more complex shapes to align with the computational domain's rectangular axis. The FASIP code includes an executable that converts the physical domain into the computational domain.

A mesh generation software, Gridgen Version 15, was used to create the structured physical mesh required by the FASIP CFD code. The airfoil geometry produced in section 2.3 was converted to a textit.iges file and imported into Gridgen as data points. This process was done for both the baseline and CFJ airfoils. The flow field was modeled around the airfoils in the far field and in the interior injection and section cavities for the CFJ airfoil. The suction cavity was modeled entirely, with the exception of the suction supports and the injection cavity was modeled at from the downstream side of the aluminum foam. This was done for simplicity so that the complex geometry of the foam would not have to be modeled.

With the model loaded into Gridgen, all non-essential lines from cuts and extrusions were removed in preparation for the flow field meshing. Then the far field was generated with one-dimensional segments called connectors. The baseline and CFJ airfoils were created the same way, except that the baseline did not have interior cavities or the lowered suction surface. Once the segments were created, each one was dimensioned with a certain number of points from which each node of the mesh would be created. Also, the distribution of these points was assigned as well with the smaller distribution near the walls where boundary layers would exist. Then, 2-dimensional domains were created and bounded by 4 connectors. The dimensions of each opposite connector within the domain needed to have the same number of points. When all domains were generated, 3-dimensional blocks were formed with 6 domains. Each block in the physical space would be converted into a cube in the computational domain with each of the 6 faces from a 2-D domain in the grid. Multiple blocks can run simultaneously through the MPI system with the FASIP code so

that the solution points are found using less clock time. Each block can run on one node within the processor.

3.3.1 Original Wind Tunnel Mesh

The original mesh created for CFD analysis was made to model the wind tunnel that each airfoil would be tested in. This mesh was not used for the final results due to the less accurate results it produced from the much smaller far field and close wall boundary conditions. This mesh contained the airfoil model with a chord of 12" (0.3048 m) and a span of 24" (0.6096 m). The dimensions of the far field were driven by the physical dimensions of the test section and were 48" (1.2192 m) long by 24" (0.6096 m) high by 24" (0.6096 m) wide. The entry and exit of the free stream flow was made curved for simplicity of mesh generation. Fig. 3.1 and 3.2 shows the mesh created for the baseline and CFJ airfoils, respectively, for the wind tunnel simulation.

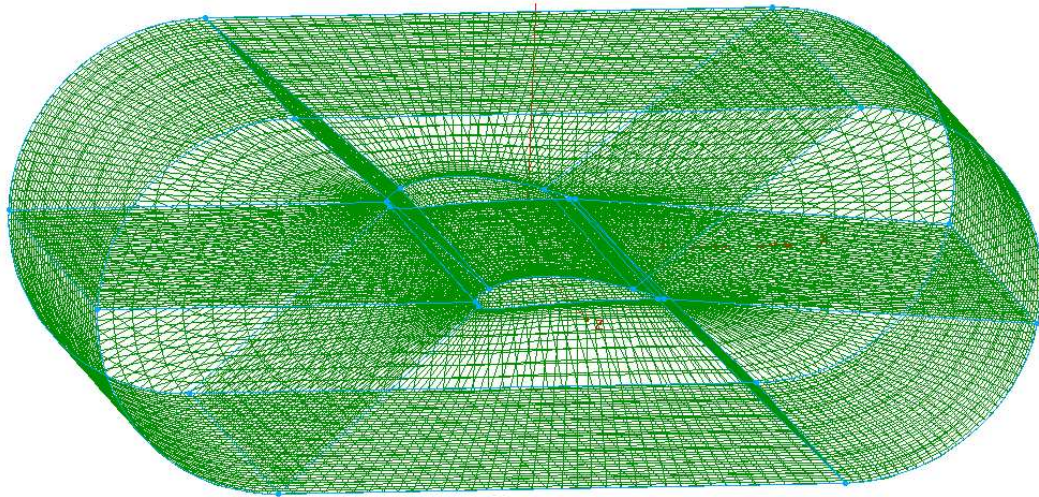


Figure 3.1: Wind Tunnel Mesh of Baseline Airfoil

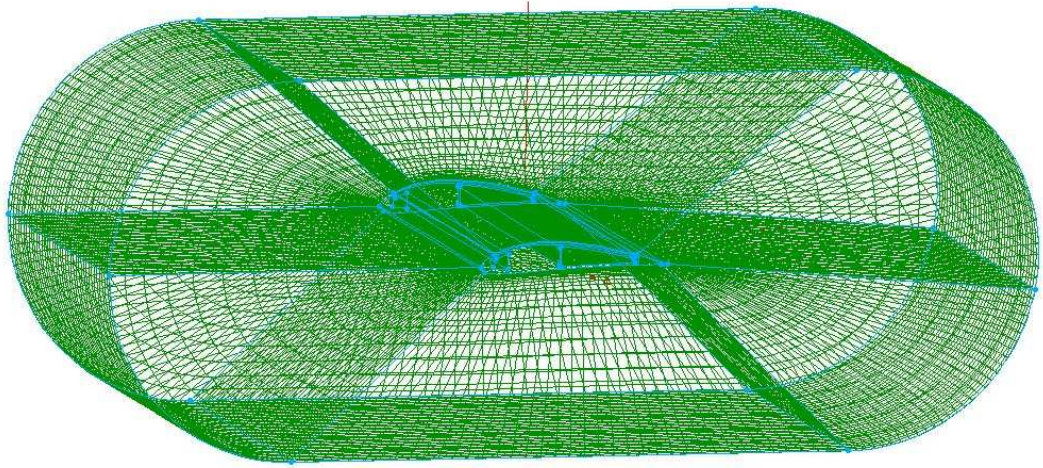


Figure 3.2: Wind Tunnel Mesh of CFJ Airfoil

In Gridgen, the dimensions are listed in the computational coordinates (ξ, η, ζ) . The ξ direction begins at the origin, which is located at the leading edge of the airfoil, and continues around the airfoil surface. The η direction begins at the origin and travels outward, and the ζ direction begins at the origin and continues along the span. The coordinate system is maintained as right-handed throughout the entire mesh. The baseline mesh had 6 blocks, separating the grid along boundaries with constant ξ dimensions. The CFJ airfoil had 9 blocks, including the same 6 exterior blocks of the baseline with the three others being the CFJ slot formed by the lowered suction surface and the injection and suction cavities.

The boundaries of the mesh on the top, bottom, left, and right sides had wall boundary conditions. This will be discussed in more detail further on. The boundaries parallel to the airfoil sides were also walls. The results from the CFD simulations with these meshes were not precise because the wall effects and the close far field could not be modeled accurately.

3.3.2 Final Mesh

After much iteration for mesh improvement, including changes to the physical size and shape, number of cells, and distribution along the walls, a final mesh shape was selected with a much larger far field. This mesh was made as an O-type mesh whose outer far field extent has a circular shape. This outer circle has a diameter of 15 chord lengths. Like the original grid, the sides of this mesh are wall boundaries as well. The distribution is much finer in this new mesh at the walls and there are more grid points throughout. The final mesh has 15 blocks, where 12 extend around the airfoil and 3 are comprised of the CFJ slot, injection cavity, and suction cavity. Fig. 3.3 shows the entire mesh and blocks 1-6 are labeled. The other blocks are located close to the airfoil are not visible in this view.

Fig. 3.4 shows the blocks located near the baseline airfoil. The blocks are divided

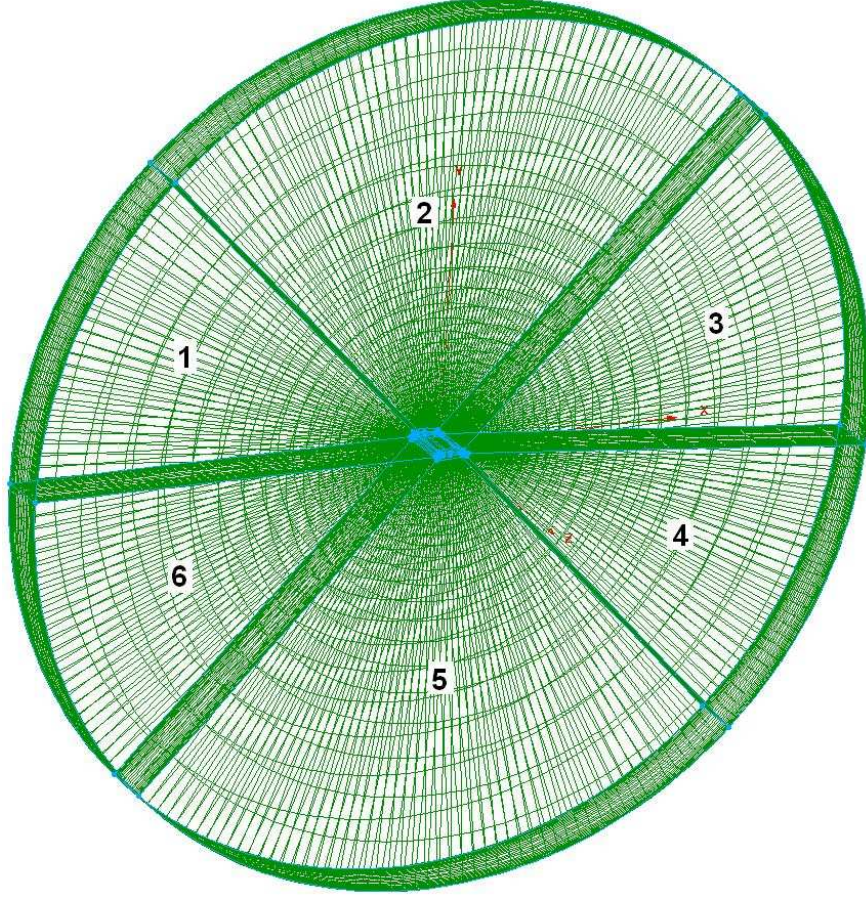


Figure 3.3: Far Field Mesh

by the number of cells each one has. Since the mesh is finer around the surface of the airfoil, the blocks are physically smaller, but have similar numbers of nodes. The block allocation for the CFJ airfoil mesh is shown in Fig. 3.5. Here blocks 1-6 and 10-15 extend around the airfoil and blocks 7, 8, and 9 are for the injection cavity, suction cavity, and CFJ slot respectively.

A closer view of the interior blocks of the CFJ airfoil is shown in Fig 3.6.

The block dimensions for the CFJ and baseline airfoil meshes are given in tables 3.1 and 3.2. These values are the number of cells along each connector in the ξ , η , and ζ direction. If the total number of node points in each connector is l than the number of cells along that particular connector is $l - 1$. When building the mesh in Gridgen, the number of node points is specified for each connector. However, when

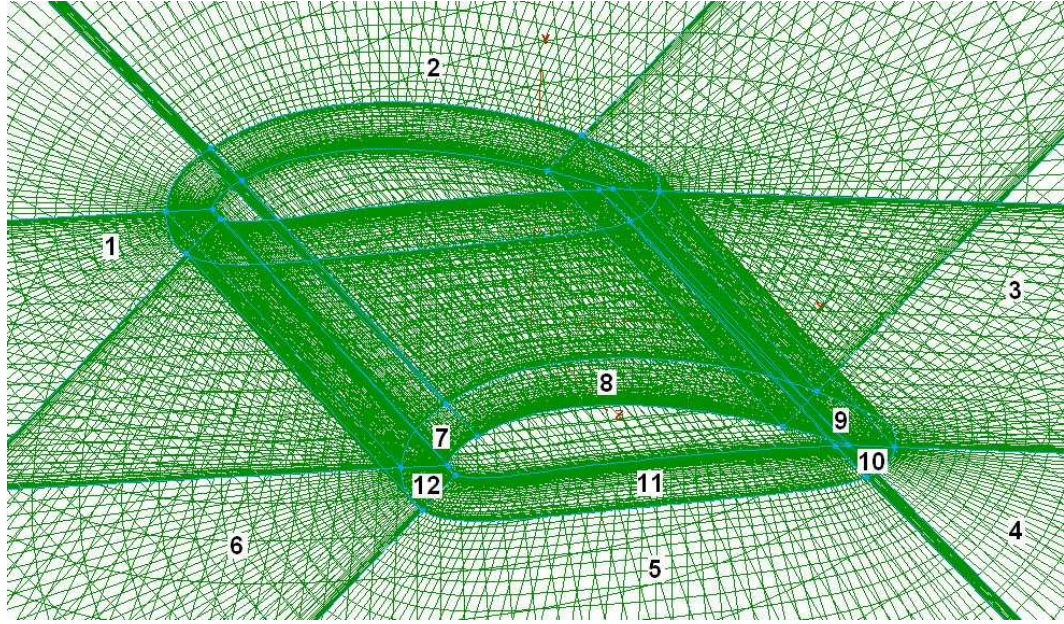


Figure 3.4: Close View of Baseline Mesh

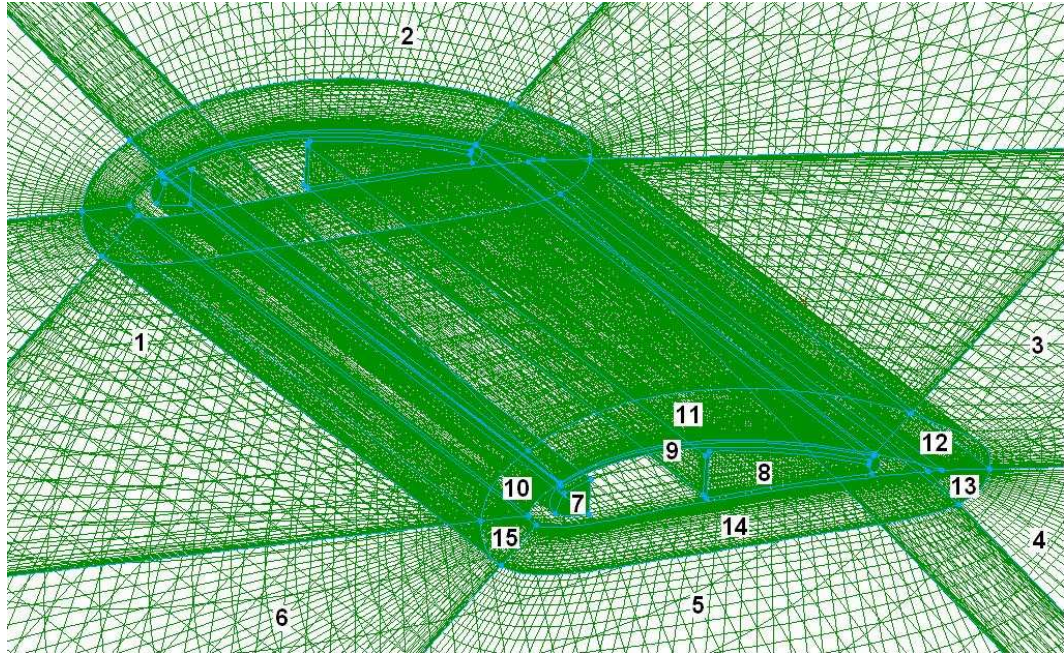


Figure 3.5: Close View of CFJ Mesh

setting up boundary and initial conditions in the FASIP code, the number of cells is given. For each block, the node points are first set to have equal distances between each, then the cell size is specified and redistributed at the surface of the airfoil and the walls. This is input as $\Delta y = 0.003$. Again, the CFJ airfoil mesh has 15 blocks,

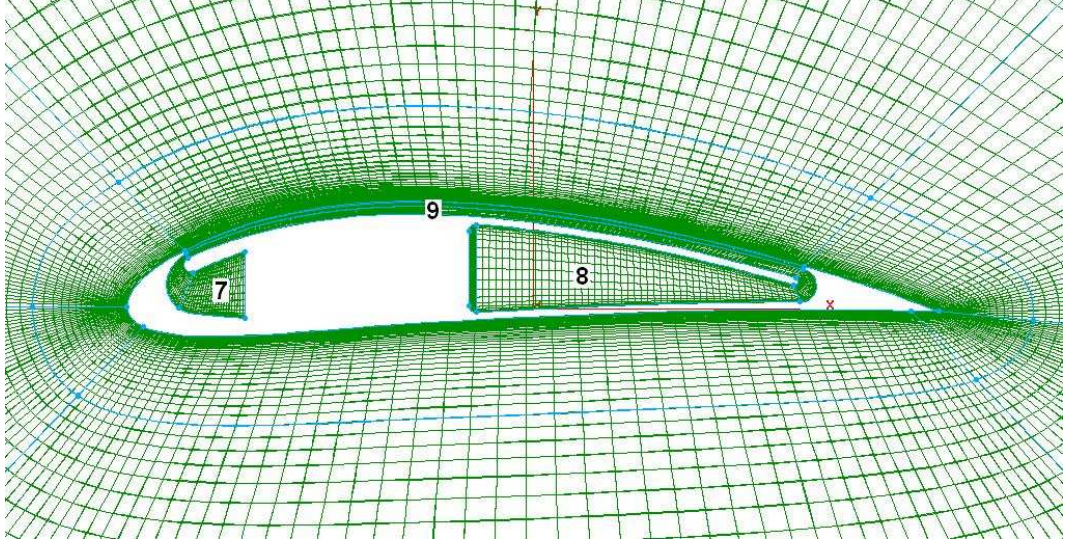


Figure 3.6: Close View of Interior CFJ Blocks

with 7-9 being the interior cavities and co-flow jet slot, and the baseline airfoil has 12 blocks.

Block	ξ -Direction	η -Direction	ζ -Direction	Total Cells
1	27	40	59	63,720
2	54	40	59	127,440
3	27	40	59	63,720
4	27	40	59	63,720
5	54	40	59	127,440
6	27	40	59	63,720
7	47	20	59	55,460
8	89	20	59	105,020
9	54	40	59	127,440
10	27	39	59	62,127
11	54	39	59	124,254
12	27	39	59	62,127
13	27	39	59	62,127
14	54	39	59	124,254
15	27	39	59	62,127
total	-	-	-	1,294,696

Table 3.1: Block Allocation for CFJ Airfoil

Block	ξ -Direction	η -Direction	ζ -Direction	Total Cells
1	27	40	59	63,720
2	54	40	59	127,440
3	27	40	59	63,720
4	27	40	59	63,720
5	54	40	59	127,440
6	27	40	59	63,720
7	27	39	59	62,127
8	54	39	59	124,254
9	27	39	59	62,127
10	27	39	59	62,127
11	54	39	59	124,254
12	27	39	59	62,127
total	-	-	-	1,006,776

Table 3.2: Block Allocation for Baseline Airfoil

3.4 Initial and Boundary Conditions for CFD

To obtain solutions for velocity, pressure, density, temperature, etc. at each node point within the solution domain, certain initial conditions must be provided. Boundary conditions are also necessary to begin the iterative solution process. For the case of the flow field around the baseline and CFJ airfoils, initial values are given for the pressures and temperatures for the incoming free stream flow. Reynolds number is also given as a flow parameter and is shown in Eq. (3.9).

$$Re = \frac{\rho UL}{\mu} \quad (3.9)$$

The free stream density, velocity, and viscosity are used in this equation. The reference length (L) is the chord length of the airfoil. Reynolds number comes from normalization of the Navier-Stokes equations given in Eq. (3.1).

3.4.1 Preliminary CFD Initial Conditions

Preliminary CFD results were obtained using the original wind tunnel mesh described earlier. These results utilized certain initial conditions that remained constant for every angle of attack tested. These results were not satisfactory but the method is discussed as part of the research. For the FASIP CFD code, there are two files to provide the main code with the initial information. Also, the code works only with normalized values so all inputs need to be dimensionless. The `datain` file contains the initial conditions for free stream flow, scheme selection, and boundary conditions. Table 3.3 shows the non-dimensional input values for the preliminary CFD results, which were used for the CFJ and baseline airfoils.

Here, p_{outlet} is the static pressure of the free stream flow, p_{total} is the total pressure of the free stream, T_{total} is the total temperature, and T_{ref} is a reference temperature used to by the code to calculate free stream viscosity from Sutherland's Law. All of

Variable	Value
Mach	0.1
p_{outlet}	71.42875
p_{total}	71.78625
Reynolds	727292
T_{total}	1.008
T_{ref}	0.43

Table 3.3: Normalized Initial Conditions for FASIP *datain* file

the above values, with the exception of T_{ref} and Re , can be found from the Mach number given for the simulations. These relations are given in Eq. (3.10), (3.11), and (3.12).

$$p_{outlet} = \frac{1}{\gamma M^2} \quad (3.10)$$

$$\bar{p}_{total} = \frac{p_{total}}{p_{\infty}} \left(1 + \frac{\gamma - 1}{2} M^2 \right)^{\frac{\gamma}{\gamma - 1}} \quad (3.11)$$

$$\bar{T}_{total} = \frac{T_{total}}{T_{\infty}} \left(1 + \frac{\gamma - 1}{2} M^2 \right) \quad (3.12)$$

The Reynolds number shown in table 3.3 was found using standard values for density, velocity at $Mach = 0.1$, and viscosity. The reference length used here is the chord length of both airfoils, 12 in. or 0.3048 m. The reference temperature was used as a standard from previous simulations, but was found to have a different value in the final CFD analysis. These inputs were used for the preliminary CFD simulations, which were performed before any wind tunnel testing took place.

3.4.2 Initial Conditions for Final CFD Simulations

Based on the results obtained from these simulations and the data collected from free stream conditions during wind tunnel tests, the CFD input values were changed. From

this change, the final results more accurately model the aerodynamic data obtained from the wind tunnel tests. Data from wind tunnel testing for the free stream total pressure, static pressure, total temperature, and velocity was used to determine the non-dimensional inputs for the `datain` file. The data fluctuated slightly for each angle of attack test with the baseline and CFJ airfoils. Therefore, with each case run using FASIP, the inputs changed as α changed. Since the wind tunnel data is dimensional, the values in Table 3.4 for p_{outlet} , p_{total} , T_{total} , and T_{ref} are normalized. These dimensional values were found using a pitot tube and a thermocouple in the wind tunnel test section. Since the thermocouple measures the temperature directly in the wind tunnel when the free stream was moving and Mach=0.1, the value for T_{total} was normalized by itself and resulted in $T_{total} = 1.000$ for all angles of attack. The equation for T_{ref} is as follows and this value utilizes T_{∞} being the free stream temperature found by the thermocouple. This input is then used by the code to calculate viscosity. The values used are in Kelvin.

$$T_{ref} = \frac{110.4}{T_{\infty}} \quad (3.13)$$

Values for total and static pressures were found from the wind tunnel data. The equation normalizing any pressure for p_{outlet} and p_{total} is as follows. The density also comes from the wind tunnel data.

$$\bar{p} = \frac{p}{\rho_{\infty} V_{\infty}^2} \quad (3.14)$$

In addition to these same inputs, the CFJ airfoil simulations require some additional information. An input file is used to give the additional pressure and temperature conditions for the injection and suction cavities. In the FASIP code, this file is called `init.input`. This file contains the total pressure in the injection cavity, the temperature in the injection cavity, and the static pressure in the suction cavity.

α	Mach	p_{outlet}	p_{total}	Re	T_{total}	T_{ref}
0	0.1	71.4683	71.9684	667950	1.000	0.37077
5	0.1	71.4711	71.9713	666057	1.000	0.37073
10	0.1	72.2193	72.7194	661755	1.000	0.37007
15	0.1	71.3405	71.8406	664985	1.000	0.36977
18	0.1	71.3768	71.8770	665308	1.000	0.37001
20	0.1	71.3768	71.8770	665308	1.000	0.37001

Table 3.4: Final Inputs for Baseline

These values, like the free stream values, were found from sensor equipment in wind tunnel testing. The total temperature inside the cavity is normalized using the free stream temperature as is shown in Eq. (3.15). The total and static pressures in this file are adjusted throughout the simulation to maintain equal mass flow rates exiting and entering the injection and suction cavity. Also, the C_μ value is maintained at either 0.05 or 0.1, according to the case being run. Tables 3.5 and 3.6 show the CFJ input information for $C_\mu = 0.05$ and $C_\mu = 0.1$, respectively.

$$\bar{T}_{cavity} = \frac{T_{cavity}}{T_\infty} \quad (3.15)$$

The final total and static pressures used to control the flow rates in the injection and suction cavities are given in the table as $p_{o\ Inj}$ and $p_{s\ Suc}$.

α	Mach	p_{outlet}	p_{total}	Re	T_{total}	T_{ref}	$T_{total\ Inj.}$	$p_{o\ Inj}$	$p_{s\ Suc}$
0	0.1	69.5077	70.0079	677920	1.000	0.36933	0.77373	71.5	67.5
5	0.1	68.9896	69.4898	677846	1.000	0.36856	0.76175	70.7	66.8
10	0.1	68.9286	69.4287	674960	1.000	0.36800	0.81248	70.2	66.4
15	0.1	69.5058	70.0060	668936	1.000	0.36690	0.72126	70.4	65.8
18	0.1	70.4221	70.9222	662085	1.000	0.36612	0.71491	71.0	65.7
20	0.1	70.4221	70.9222	662085	1.000	0.36612	0.71491	71.4	65.2
23	0.1	70.6729	71.1731	652036	1.000	0.36287	0.72126	72.0	65.4
25	0.1	71.5607	72.0609	648686	1.000	0.36380	0.73378	72.5	67.2

Table 3.5: Final Inputs for CFJ, $C_\mu = 0.05$

α	Mach	p_{outlet}	p_{total}	Re	T_{total}	T_{ref}	T_{total} Inj.	$p_{\circ Inj}$	$p_{s Suc}$
0	0.1	67.6771	68.1774	682232	1.000	0.36733	0.63078	73.9	64.9
5	0.1	68.3691	68.8691	671522	1.000	0.36560	0.56026	72.0	63.4
10	0.1	68.2431	68.7433	673290	1.000	0.36605	0.67168	72.0	63.4
15	0.1	68.9683	69.4685	655516	1.000	0.36660	0.73951	72.4	63.0
20	0.1	71.0572	71.5574	655516	1.000	0.36487	0.56816	73.6	62.8
25	0.1	70.8441	71.3443	651695	1.000	0.36328	0.50921	73.0	62.6
28	0.1	71.5786	72.0787	644079	1.000	0.36206	0.57439	74.2	63.0
30	0.1	71.4682	71.9684	643318	1.000	0.36194	0.57847	74.2	62.8

Table 3.6: Final Inputs for CFJ, $C_{\mu} = 0.1$

Since the FASIP code is equipped with several differencing schemes at various orders of accuracy and multiple turbulence models, the schemes used for each CFD simulation must also be included in the initial inputs. This information is provided in the `datain` file. Table 3.7 shows the schemes chosen for all cases for both baseline and CFJ airfoil simulations. The *CFL* (Courant-Friedrichs & Lewy) number is included as well, and it is described in Eq. (3.16).

$$CFL = \frac{c\Delta t}{\Delta x} \quad (3.16)$$

Variable	Value
CFL	1.0
LHS Scheme	Van Leer
LHS Order	1st Order MUSCL
RHS Scheme	Zha3
RHS Order	3
Turbulence Model	Baldwin Lomax

Table 3.7: Scheme Selection for Baseline and CFJ Simulations

3.4.3 Boundary Conditions for CFD Simulations

Along with initial conditions, the code also requires boundary conditions for the fluid flow domain. FASIP makes use of several types of boundary conditions for various cases. For the baseline and CFJ airfoil cases, boundaries are defined at all faces of each mesh block. The following boundary conditions are used for the baseline case.

- BC 3 - no-slip adiabatic wall boundary given at all airfoil surfaces and mesh sides where $\zeta = 1$ and $\zeta = Max$
- BC 6 - subsonic inflow used at the far-field where flow is entering the region
- BC 7 - interface boundary for MPI used at all subdomain boundaries for parallel computing

- BC 11 - subsonic outflow used at the far-field where flow is leaving the region

For the CFJ case, the above conditions are used along with these additional boundary conditions to define the flow going into the injection cavity and out of the suction cavity.

- BC 5 - subsonic outflow, fixed static pressure for suction cavity
- BC 9 - subsonic inflow with total pressure specified, used for incoming flow in injection cavity

The subsonic outflow (BC 5) is defined along the side of the suction cavity where $\zeta = 1$. This simulates how the flow will be removed from the side of the airfoil during wind tunnel testing. The subsonic inflow (BC 9) enters along the span of the injection cavity with $\xi = 1$ with a given total pressure. This will also simulate the wind tunnel test as the uniform flow entering the injection cavity after the aluminum foam. Total pressure in the injection cavity and static pressure in the suction cavity can be adjusted for each CFD case to control and maintain equal mass flow rates exiting and entering the cavities. These boundary conditions are assigned to each mesh surface via cell number. For each change in α , the airfoil is rotated within the mesh and the boundary conditions for far field inflow and outflow are adjusted as well. A sample `datain` file and `init.input` file are provided in the appendix for the CFJ airfoil case with $C_\mu = 0.05$ and $\alpha = 10^\circ$.

3.4.4 Adjusting Mass Flow Rates

To achieve zero net mass flux loss with the CFJ flow control method, the mass flow of air that exits the injection slot must equal the mass flow entering the suction slot. For numerical CFD simulations, this is achieved by controlling and adjusting the total pressure in the injection cavity and the static pressure in the suction cavity. An initial

value is given for each pressure in the `init.input` file. After running the simulation for 2,000 steps, the mass flow rates and the C_μ for each case can be determined by running the `flowrate` executable. If the resulting injection mass flow rate is too low, the total pressure in the `init.input` file should be increased. If mass flow is too high, then the total pressure should be decreased. If the mass flow rate for the suction cavity is too high, the static pressure in the in the `init.input` should be increased (to decrease the vacuum). Conversely, if the flow rate is too low then the static pressure should be decreased (to make the vacuum stronger). This process should be repeated throughout the simulation until the desired C_μ value is reached and the mass flow rates for injection and suction match within 5%.

3.5 Post-Processing of CFD Results

After each case is run using the FASIP CFD code, the resulting values of pressure and velocity must be processed to obtain useful results such as lift and drag coefficients with airfoils. Post-processing executables, that were previously developed, were modified for use with the NACA 6415 baseline and CFJ 6415-065-142 airfoils. Values for lift, drag, and flow rates for the CFJ airfoil were calculated using these executables. Also, plot data for pressure distributions, velocity profiles, streamlines, and other flow parameters were created and processed using Tecplot360 data analysis software.

3.5.1 Baseline Lift and Drag

From the baseline case, only C_L and C_D were used as results. The post processing executable calculates the pressure distribution along the surface of the airfoil for each block. The sums of each component are used to obtain the total dimensionless lift and drag for each case. Since lift is always perpendicular to the free stream flow and drag

is parallel to free stream flow, the angle of attack must be included in the calculation of each coefficient. Also, the dimensionless reference length and area needs to be included to acquire the C_L and C_D per dimensionless unit length. For the baseline and the CFJ airfoil, the reference length = 1 and reference area = 2 (The chord length of 12" (0.3048 m) is normalized to 1 and the span of 24" (0.6096 m) is normalized to 2, so reference area is $1 \times 2 = 2$). Equations 3.17 and 3.18 show how the coefficients C_L and C_D can be used to obtain dimensional force values, where L and D are the lift and drag forces and S is the span area of the airfoil.

$$L = C_L \cdot \frac{1}{2} \rho_{\infty} V_{\infty}^2 S \quad (3.17)$$

$$D = C_D \cdot \frac{1}{2} \rho_{\infty} V_{\infty}^2 S \quad (3.18)$$

The final values obtained for lift and drag coefficients from the baseline CFD simulations are shown in table 3.8.

α	C_L	C_D
0	.661504	.028353
5	1.16956	.038843
10	1.56653	.048900
15	1.73722	.072137
18	1.68080	.093950
20	1.56362	.123666

Table 3.8: C_L and C_D for CFD Baseline Case

3.5.2 CFJ Lift & Drag Including Jet Effects

For the CFJ airfoil, C_L and C_D are found in the same manner, where the pressure distributions were summed along the airfoil's surface including the lowered suction surface. The co-flow jet airfoil gains its benefits from the high velocity jet exiting the

injection slot and entering the suction slot. This jet creates added forces that must be included in the overall force generation of the CFJ airfoil. In addition to lift and drag created in the conventional way, as with the baseline airfoil, the CFJ airfoil generates jet effects from the reactant forces of the jet produced. A control volume analysis done on the CFJ airfoil yields the following equations and these jet effects must be included in the calculation of overall lift and drag [6,7]. Eq. (3.19) and (3.20) are the jet effect reactant forces in the x and y directions respectively.

$$F_x = (\dot{m}_j V_{j1} + p_{j1} A_{j1}) * \cos(\theta_1 - \alpha) - \gamma(\dot{m}_j V_{j2} + p_{j2} A_{j2}) * \cos(\theta_2 + \alpha) \quad (3.19)$$

$$F_y = (\dot{m}_j V_{j1} + p_{j1} A_{j1}) * \sin(\theta_1 - \alpha) - \gamma(\dot{m}_j V_{j2} + p_{j2} A_{j2}) * \sin(\theta_2 + \alpha) \quad (3.20)$$

In the above equations, the subscript j means *jet* and the subscripts 1 and 2 signify injection and suction respectively. γ can be 0 or 1, if there is only injection blowing and no suction, then $\gamma = 0$. If there is suction than $\gamma = 1$. The angles θ_1 and θ_2 are the angles formed by the injection and suction jet openings with the line normal to the chord. With the jet angles, the horizontal and vertical components of the jet effects can be found so that the reactant forces can be included with the overall lift and drag. Fig. 3.7 shows how these angles are formed. This profile is not a CFJ 6415-065-142, but it is used to simply illustrate how the jet angles are determined. For the CFJ 6415-065-142 airfoil, the angles were determined by the model drawings and $\theta_1 = 26.7^\circ$ and $\theta_2 = 41.4^\circ$. The values for F_x and F_y are then subtracted from the lift and drag forces obtained from the surface integrals of pressure and shear stress on the CFJ airfoil. The values for lift, drag, F_x , and F_y are normalized in the post processing executable included in the FASIP CFD code. The resulting lift and drag is

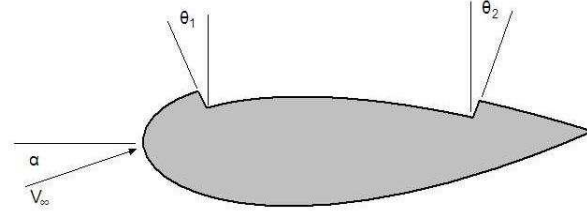


Figure 3.7: Angles of Injection and Suction Slot for Jet Effects

shown in Eq. (3.21) and (3.22), where R'_y and R'_x are the surface pressure and shear stress integrals in the y and x directions [6].

$$L = R'_y - F_y \quad (3.21)$$

$$D = R'_x - F_x \quad (3.22)$$

The results for lift and drag coefficient including jet effects are shown in Tables 3.9 and 3.10.

α	R'_y	R'_x	F_y	F_x	Final C_L	Final C_D
0	2.69214	-0.80274	1.74294	-0.65550	0.94920	-0.14724
5	3.30534	-0.60257	1.78025	-0.50014	1.52509	-0.10243
10	3.83952	-0.38862	1.80739	-0.34394	2.03213	-0.04468
15	4.20498	-0.12929	1.82316	-0.17962	2.38182	0.050330
18	4.42573	0.004579	1.87553	-0.09621	2.55020	0.100789
20	4.38725	0.125414	1.85418	-0.01596	2.53307	0.141374
23	4.04487	0.299284	1.86137	0.085263	2.18350	0.214020
25	4.31873	0.391604	1.88390	.143692	2.43483	0.247912

Table 3.9: Jet Effects and Final C_L and C_D for $C_\mu = 0.05$ Case

3.5.3 Flow Rates and C_μ

Dimensionless mass flow rates are also calculated by a post processing executable called `flowrate`. The flows out of the injection slot and into the suction slot are calculated along the span of the airfoil. The total pressure in the injection cavity

α	R'_y	R'_x	F_y	F_x	Final C_L	Final C_D
0	2.91310	-0.80523	1.78421	-0.62769	1.1289	-0.17754
5	3.42997	-0.59521	1.79658	-0.46481	1.63339	-0.13040
10	3.96663	-0.38048	1.82522	-0.30135	2.14141	-0.07913
15	4.47654	-0.15120	1.85618	-0.14633	2.62036	-0.00487
20	5.06366	0.100350	1.90541	0.007019	3.15825	0.093331
25	5.23048	0.367380	1.88223	0.170169	3.34825	0.199211
28	5.19676	0.558022	1.88362	0.283210	3.31314	0.274812
30	4.80737	0.757541	1.87291	0.344671	2.93446	0.412870

Table 3.10: Jet Effects and Final C_L and C_D for $C_\mu = 0.1$ Case

and the static pressure in the suction cavity were adjusted until these mass flow rates were within 5% of each other. Since the results would be compared with experimental results, a modification to the original `flowrate` file made the mass flow rates dimensional in units of kg/s. The C_μ value was also determined by the `flowrate` file and the pressures and flow rates were adjusted to achieve the desired C_μ depending on the case. Table 3.11 and 3.12 shows the final mass flow rates for the injection and suction cavity and the corresponding values of C_μ based on the injection cavity flow rate.

α	\dot{m} Injection (kg/s)	\dot{m} Suction (kg/s)	C_μ
0	0.107994	0.110231	0.050280
5	0.112109	0.118539	0.053683
10	0.107234	0.110402	0.053088
15	0.110270	0.103383	0.050266
18	0.119183	0.126728	0.059105
20	0.118365	0.122550	0.057930
23	0.118756	0.124229	0.059311

Table 3.11: Flow Rate Values for $C_\mu = 0.05$ Case

The final results for the CFD analysis of the baseline and CFJ airfoil are included in the *Results* chapter, where they are compared with the experimental wind tunnel results.

α	\dot{m} Injection (kg/s)	\dot{m} Suction (kg/s)	C_μ
0	0.179881	0.183300	0.110448
5	0.184422	0.175671	0.107995
10	0.175450	0.170921	0.117887
15	0.162434	0.169075	0.117265
20	0.183239	0.194503	0.111171
25	0.189332	0.192237	0.107701
28	0.186616	0.187304	0.118943
30	0.178201	0.178234	0.109146

Table 3.12: Flow Rate Values for $C_\mu = 0.1$ Case

Chapter 4

Wind Tunnel Laboratory Design and Setup

Another major aspect of this research included the design and setup of a CFJ Wind Tunnel Laboratory at the University of Miami. This was required to experimentally study the performance enhancements of the co-flow jet flow control method. Wind tunnel test results of the baseline and CFJ airfoil models were also used to further validate the FASIP CFD code for use with aerodynamic simulations. A standard wind tunnel required modification so that the test section could withstand the increase in aerodynamic forces produced by the CFJ airfoil. To accurately test the CFJ airfoil, a controlled air delivery system was needed to supply the jet air. This system provides the high pressure air for the injection slot and also employs a vacuum to remove the air from the suction slot. To achieve zero net jet mass flux within the system, the mass flow rates through the injection and suction slots must be equal. Furthermore, it was necessary to acquire the injection C_{μ} value so that it could be held constant for each series of tests. Gathering all of the necessary data required a six-component force and moment balance and flow rate sensor equipment, including pressure transducers, thermocouples, orifice plates, and a computer controlled valve. All of this information

was compiled in a data acquisition system to be used for each wind tunnel test. The wind tunnel test results for the NACA 6415 baseline airfoil and the CFJ 6415-065-142 airfoil for C_μ values of 0.05 and 0.1 are shown and compared to the CFD results for each case.

4.1 Wind Tunnel Modifications

The wind tunnel selected for the CFJ Wind Tunnel Laboratory is a 24" Open Circuit Wind Tunnel from ERG (Engineering Laboratory Design, Inc.). The electric motor can run at a maximum of 60 Hz and the tunnel is listed to have a maximum speed of 50 m/s. The test section of this tunnel is 48" (1.2192 *m*) long, 24" (0.6096 *m*) tall and 24" (0.6096 *m*) wide. Modifications were made to the existing test section, which is comprised of 4 acrylic walls that are 0.75" thick. This test section was originally designed to withstand the loads from a symmetric NACA 0025 airfoil with an 8" (0.2032 *m*) chord. The loads supplied from the cambered CFJ airfoil with a 12" (0.3048 *m*) chord will be higher. For this reason, the acrylic wall was reinforced with 0.5" (1.27 *cm*) thick aluminum plates. The plates were originally designed to replace the acrylic wall where the airfoil model was made to attach. However, it was found that the acrylic wall could not be removed without damaging the other faces of the test section, so the aluminum plates were made to fit over the existing acrylic. The plates were made in 4 sections, each joining at an overlapping edge and fastened with screws. This was done for ease of machining and assembly. Drawings of the parts were sent to a CNC machinist at Cypress Tools to make the parts. The following figures show the aluminum wall assembly and their connections.

The holes shown in Fig. 4.1 around the edges of the plates are screw thru holes used to connect the plates to the test section. The holes near the circular cut out are used to secure a wind tunnel box to the test section. This box will house the

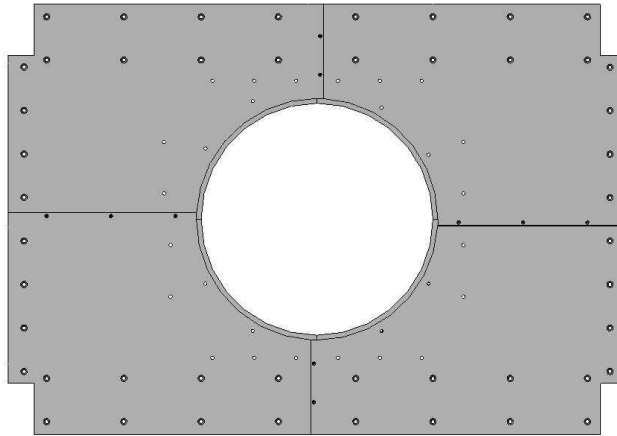


Figure 4.1: Aluminum Wall Assembly

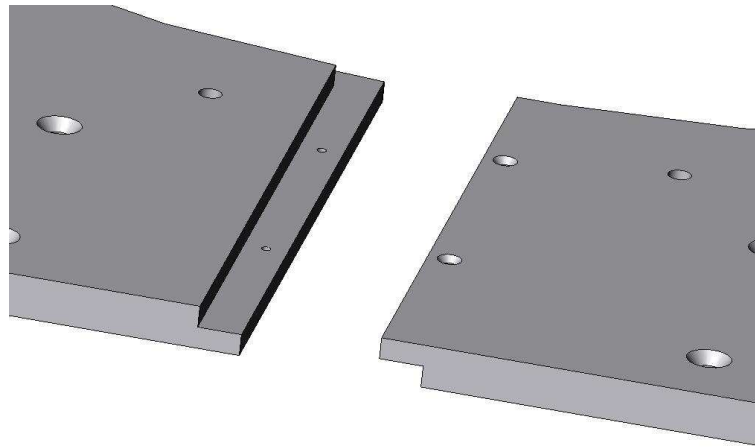


Figure 4.2: Aluminum Wall Plate Connections

force balance, pressure and temperature sensors for the CFJ airfoil's cavities, and to provide the air connections to the airfoil. The sealed box is necessary so that air does not leak out of the test section or enter the test section during testing. The circular cut out in the aluminum plates is needed so that a matching circular insert piece, CNC machined from aluminum, can be used to rotate the airfoil for various angles of attack. This circular insert part has cut-outs matching the geometry of the sting and force balance airfoil connection and the suction manifold for vacuum hook ups. The diameter of the plate is driven by fact that the center of rotation needs to be where the airfoil is connected at the $1/4$ chord and also by the distance from the

center to the farthest point on the extruded endplate geometry. A tolerance gap of 0.005" (0.127 mm) exists between the aluminum plates and the circular insert for ease of turning. This plate fits into the aluminum wall with a stepped edge, which will prevent the circle from falling into the test section and it will be secured by clamps on the opposite side to prevent unwanted rotation during tests. This circular plate is shown in Fig. 4.3. The square cut out is for the airfoil's endplate connection to the force balance and where air enters the injection cavity and the curved cut out is for the suction manifold where air is removed from the suction cavity. The circular cut is for the extension of the pitot tube which is located in the injection cavity forward of the aluminum foam for measurement of total pressure within the cavity.

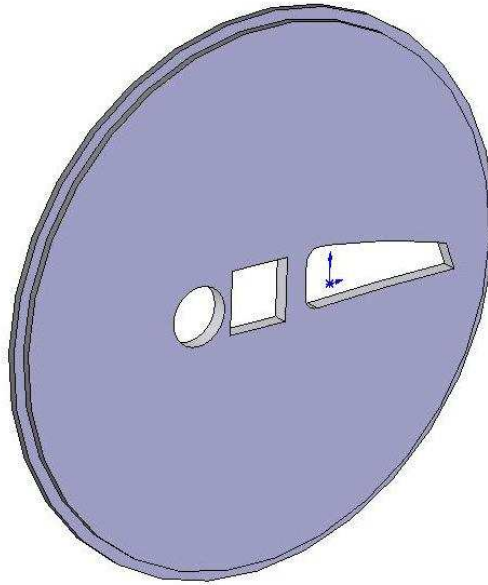


Figure 4.3: Circular Plate for Fitting with Aluminum Wall Assembly

The circular plate will be held in place by clamps that are screwed into the aluminum wall plates. The clamps were machined in-house out of aluminum and also have tapped holes for set screws to push against the aluminum wall plates. These clamps act as levers, where their screw connections act as the fulcrum and the tension from the set screws is the applied load. Therefore, the contact between the clamp and the circular insert plate has a strong force to prevent the plate from rotating or

falling back. Small silicone pads were placed under clamps at the connection point to prevent slipping. Fig 4.4 shows one of these clamps as it attaches to the aluminum wall plates and the circular insert.

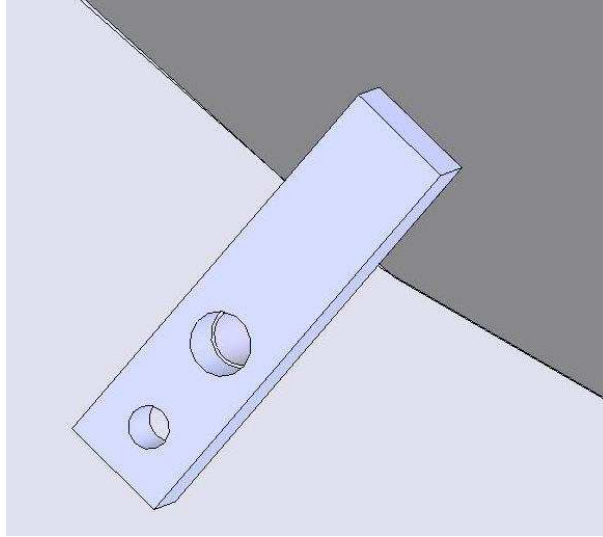


Figure 4.4: Clamp used for Securing Circular Insert

To accommodate the rotating aluminum plate for changing the model's angle of attack, an 18" (0.4572 m) diameter circular cut out was made in the acrylic wall of the wind tunnel test section. A matching circular plate with the same cut outs as the aluminum circular insert was made for the 0.75" (1.905 cm) thick acrylic wall of the test section. Again, a tolerance gap of 0.005" (0.127 mm) from the diameter was made for this plate. This acrylic circle is secured to the aluminum circle by screws and it does not have a stepped edge. The plate rotates in unison with the aluminum plate and its purpose is simply to maintain the surface inside the test section. Without this piece, the inside wall of the test section would have a 0.75" (1.905 cm) step down where the circle cut out would be. The Fig.full-wall-assem shows the front and back of the full wall assembly with the aluminum plates, aluminum circular insert, acrylic insert, acrylic circle, and clamps.

The holes forming a square pattern around the circular cut out are for the connection of a sealed wind tunnel box. This box houses the sensor equipment and air

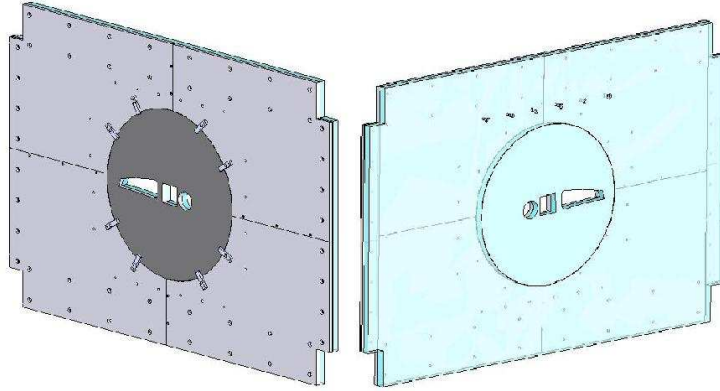


Figure 4.5: Modified Test Section Wall Assembly

delivery hook-ups that are necessary for testing the CFJ airfoil and that cannot be inside the test section. The force balance and sting connections to the airfoil and the rigid balance connection are located in the box as well. The front face, top, and bottom of the box are made from 0.5" (1.27 *cm*) thick aluminum because these faces will support the largest load from the vertical lift component and its resulting moments as well. The sides of the box are 0.5" (1.27 *cm*) thick acrylic so that the inside of the box is visible. The acrylic right side of the box was made as a hinged door set for inside access. The outside measurements of the box are 24" (0.6096 *m*) wide by 22" (0.5588 *m*) high by 12" (0.3048 *m*) deep. The figure below illustrates the wind tunnel box with its front, top, bottom, and sides.

The front face of the box also has a stepped circular cut out similar to the one that fits into the aluminum wall. This aluminum circular plate will bears the load of the airfoil through the sting extender and the force balance. This plate also rotates to change the angle of attack, and is held in place by the same clamp parts that hold the inner aluminum circle in place. The cut outs in this plate are different than the inner circular insert because this plate has the air connections to the high pressure air and vacuum systems. A 3/4 NPT tapped hole is located in the center of the plate for the injection air hose connection. The three larger circles are for the suction manifold connection. In the airfoil model, there is a suction manifold that couples the

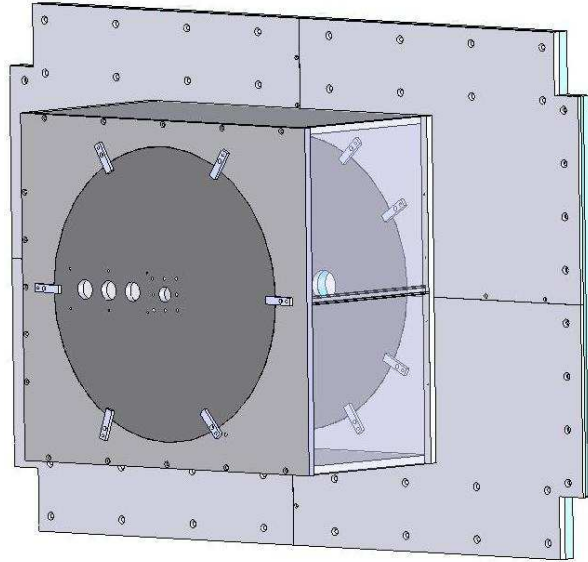


Figure 4.6: Wind Tunnel Box

endplate to three flexible vacuum hoses for air removal. These vacuum rated hoses have a 1.125" (2.8575 *cm*) ID (inner diameter) and they connect to both manifolds with screw-on hose connectors. The hoses are each 10.5" (0.254 *m*) long, including the hose connectors. On this aluminum plate, another suction manifold transforms the three vacuum hoses to a single 3" diameter outlet that is required for union to the suction air line. This manifold, like the one connected at the suction cavity, was SLA prototyped by Solid Concepts. The sting and force balance assembly are secured to the outer circular plate with 8 screws and lock nuts. The stainless steel sting has a very rigid connection to the back aluminum wall of the wind tunnel box. A 1.5" (3.81 *cm*) diameter hole was made in the bottom plate of the wind tunnel box so that the cables for the force balance, pressure sensors, and thermocouple could have access to the exterior of the box. Fig. 4.7 shows the wind tunnel box with the manifold to the suction line and the connection holes for the injection air line.

Since the rigid sting connection is located at the far circular plate in the wind tunnel box, a support for the force balance is necessary so that the moments felt by the balance are accurate. Without this support, the sting and the balance might

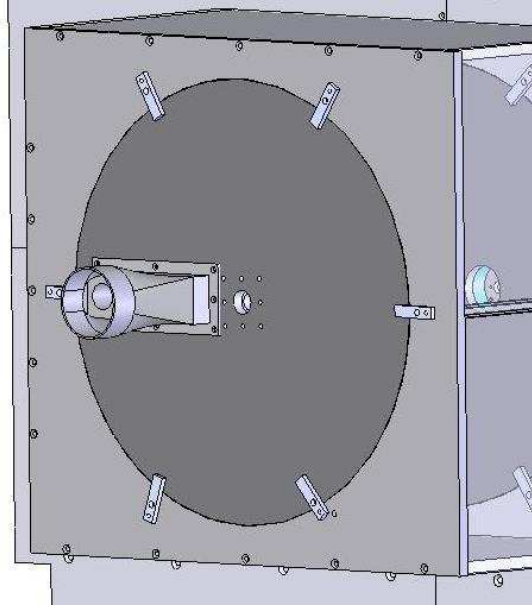


Figure 4.7: Outer Circle for Wind Tunnel Box with Suction Manifold

bend in unison about the rigid connection and the balance would not be reading the correct moments about the x and y axis. A sting support was made in-house out of PVC plastic to help maintain the moments about the balance. This material was chosen for its ease of machining and because the stainless steel sting welded to the square stainless flange was very solid. This piece was inserted under the sting and secured to the bottom of the box with screws through the bottom surface into the support. The top of the support is held in place by screws secured to the bottom of the support and the sting is held solid by the clamping action of these two pieces. Fig. 4.8 shows this support around the sting where the screw holes are clearly visible. To insure that the wind tunnel box is air tight, a silicon sealant was applied to the interior of the box at the intersection of each piece. The hole where the cables enter the box was also sealed with electrical tape. The aluminum and acrylic wind tunnel box parts, including the stepped rotating circles, were CNC machined by Cypress Tools. The drawings for each of these parts and the four sections of the aluminum wall are included in the appendix. The front and back of the full wind tunnel box assembly with airfoil connection is shown in Fig. 4.9. The actual finished product of

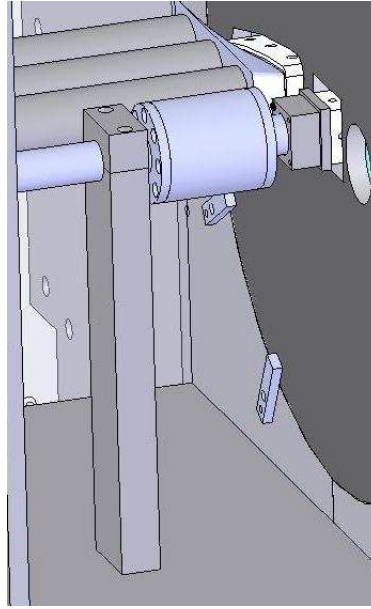


Figure 4.8: Sting Support Piece

the wind tunnel box is shown in figures 4.10, 4.11, and 4.12

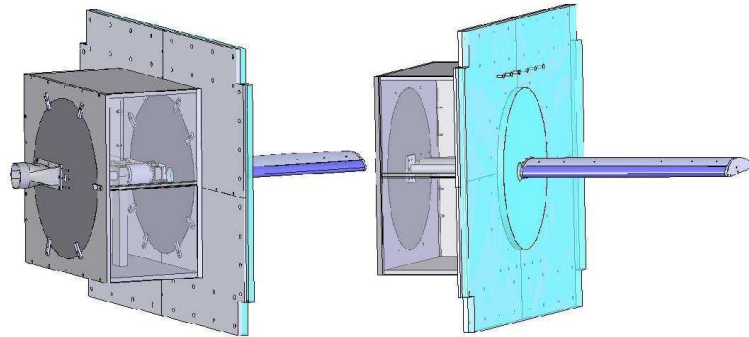


Figure 4.9: Full Wind Tunnel Box Assembly Drawing

4.2 Air Delivery System

To provide the Co-Flow Jet airfoil with a high velocity injection jet and to remove air at the suction slot, an air delivery system is necessary. To accurately maintain and measure the injection and suction mass flow rates, certain equipment and measuring devices were used in the CFJ Wind Tunnel Laboratory. The system was designed to maintain a maximum injection $C_\mu = 0.4$ (with a corresponding $\dot{m} = 0.5264$ kg/s)

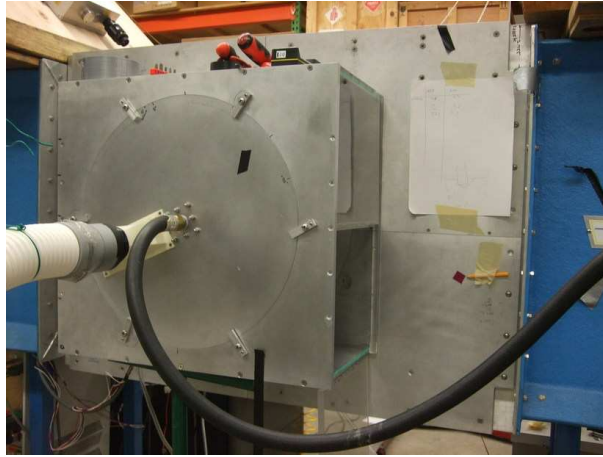


Figure 4.10: Complete Wind Tunnel Box Assembly



Figure 4.11: Sting Support Piece and Force Balance

for 60 seconds and to remove the air from the suction cavity at the same rate that it entered the injection cavity. To achieve this, the injection line required a compressor, a high pressure air storage tank, and a computer controlled valve, while the suction side used a vacuum pump and a vacuum storage tank. Calculations based on the state equation (Eq. (2.13)) for compressible flow were used to determine the time it would take the compressor to fill the holding tank (5.82 min.) and the time that the experiment could run at full C_μ value (2.98 min. with the compressor running). This

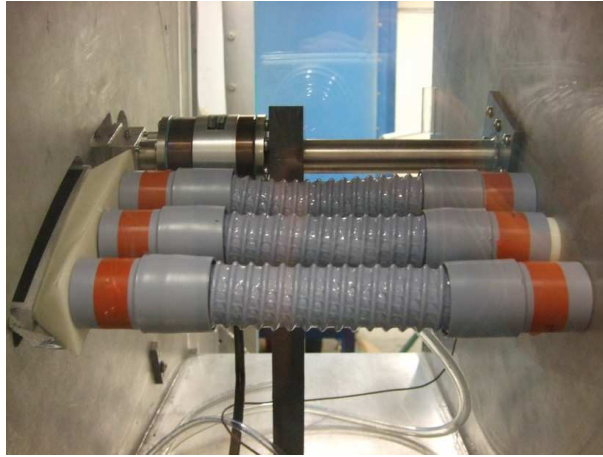


Figure 4.12: Suction Cavity Manifold and Vacuum Hoses

would be the worst case scenario. Determining what equipment to use was based on iterations between the equipment capabilities and the budget of the project. A flowchart of the equipment and piping sizes is included in the appendix.

4.2.1 Injection Line

The compressor chosen was an Ingersoll Rand UP6-15cTAS-150 compressor. This unit produces 50 CFM (cubic feet per minute) at 150 psi ($0.0236 \text{ m}^3/\text{s}$ at 1034 kPa). This Total Air System, compresses, cools, dries, and then outputs air at 72°F (22.22°C). The unit also includes a 120 gal (0.4542 m^3) air storage tank. The injection air storage tank is 2000 gallons (7.5708 m^3) with a maximum storage pressure of 150 psi. A larger tank and a smaller compressor were used to minimize project cost. To control the flow into the injection cavity, an electro-pneumatic computer controlled valve with feedback control was selected. This valve will be driven by the mass flow rate determined at the orifice plate. If the desired mass flow rate is not matched by the flow meter, the control valve will raise and lower accordingly until the mass flow rate matches the input value at the test stand. This is discussed in more detail in the *Sensors* section. The valve is a model IMO-G110-1 purchased from Koso Hammel Dahl Control Valves that utilizes pneumatic force to raise and lower the valve. A

small amount of air, ranging from 15 – 60 psi (103.4 – 413.7 kPa), is taken from the compressor and an electrical signal, ranging from 4 – 20 mA, from the computer regulates the air. The reading from the mass flow meter just downstream from the valve tells the valve whether it needs open further or close more. Fig. 4.13 shows the compressor and Fig. 4.14 shows the computer controlled valve used in the CFJ Wind Tunnel Laboratory.



Figure 4.13: 50 CFM Compressor

4.2.2 Suction Line

The vacuum pump is a 60 hp Dekker V-MAX system. This vacuum pump is connected to a 600 gallon (2.2712 m^3) vertical vacuum tank. This tank is used to regulate and maintain a steady vacuum for the suction cavity. A gate valve is used to manually adjust the suction flow rate to match the injection mass flow rate. A mass flow meter is also located in the suction line between the tank and the suction cavity so that the suction mass flow rate can be determined. More detail on the mass flow meter and how the flow rate is calculated is given in the *Sensors* section. Fig. 4.15 shows the



Figure 4.14: Pneumatic Computer Controlled Valve

vacuum pump used in the lab.



Figure 4.15: 60 Hp Vacuum Pump

Once the components were selected, the lab layout was designed. The space allocated for the CFJ lab needed to be re-wired for the electrical requirements of the equipment. The placement of each component was based on regulations for a working laboratory and safety procedures, simplistic set-up for the electrical access, and order of delivery for each piece. The lab layout based on the equipment placement is shown in Fig. 4.16. The piping layout is based on the requirements of the pressure

sensors in the lines. Each sensor requires a certain distance of straight pipe and pipe diameter. The inlets and exits of each component also attribute to the piping sizes and layout. These details are included in the following section discussing the sensors used. The piping installation was done by a contracting company hired by the University of Miami. The lengths and diameters of the pipes and the location of each lab component was given to the company and the piping was constructed according to these specifications.

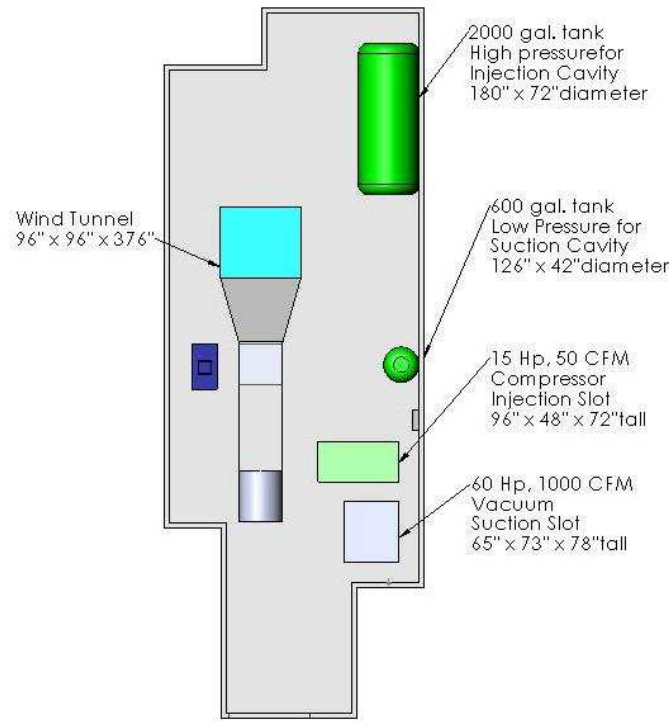


Figure 4.16: Layout of CFJ Wind Tunnel Laboratory

The completed piping for the air system is shown in Fig. 4.17. The connection of the injection line to the tapped hole in the outer circle of the wind tunnel box is completed with a 1" (2.54 cm) diameter high pressure flexible hose with a swivel connection to the male 3/4 NPT connection. This way, the plate can be rotated to various angles of attack without restriction. The connection from the vacuum line to the manifold on the outside of the outer circle is completed with a 3" (7.62 cm) diameter flexible

vacuum hose. It is connected with a hose clamp to the manifold on one end and fits over a 3" (7.62 cm) barbed hose coupler to a 3" (7.62 cm) male NPT connection to the suction line. These connections are shown in the Fig. 4.18.



Figure 4.17: Piping for Air Delivery System

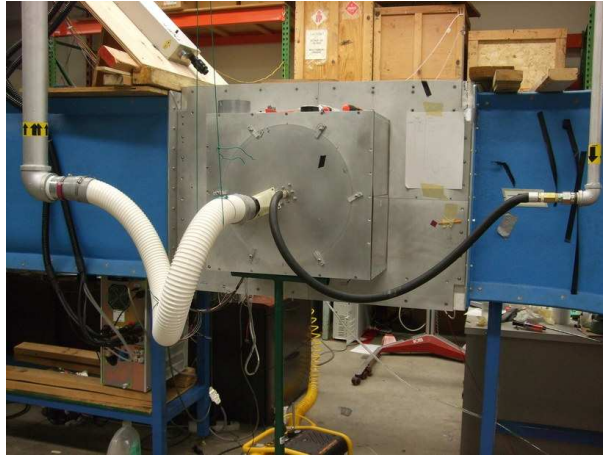


Figure 4.18: Connection of Injection and Suction Line to Wind Tunnel Box

4.3 Sensors and Data Acquisition System

Various sensor and control equipment was used to acquire the necessary data produced during wind tunnel testing of the baseline and co-flow jet airfoils. Ultimately, the critical measurements include non-dimensional force coefficients generated by both



Figure 4.19: Overall View of CFJ Wind Tunnel Laboratory

airfoils and the momentum coefficients of the injection jet achieved by the CFJ airfoil for each angle of attack. The data is collected as force balance loads and various fluid parameters, including static pressures, total pressures, differential pressures, and temperatures. All necessary values for experimental data can be computed from these measurements. This experimental data is compiled into an acquisition system using Labview. Equations are provided to determine all relevant information.

4.3.1 Injection Line

The injection line begins at the compressor where air is compressed and sent to the 2000 gallon (7.5708 m^3) tank where it can reach a maximum pressure of 150 psia (1034 kPa) before a safety blow off valve will expel the excess air. The outlet of the injection tank is controlled by a manual valve that allows the air into the injection line for testing. This 2" (5.08 cm) diameter outlet then goes to the electro-pneumatic control valve. The control valve is controlled by current output from the test stand computer. The default position of the valve is closed, so in case of power failure the valve will close for safety. A 4-20 mA output allows air into the pneumatic chamber

of the valve, lifting the main valve piston and allowing the controlled air into the injection line. The air for the piston chamber is supplied by a small line directly from the compressor. This line has a regulator to maintain the pressure between 15 – 60 psia ($103.4 - 413.7 \text{ kPa}$). Before testing, the valve on this line should be opened because the control valve will not function without it.

From mass conservation, the mass flow rate entering the injection cavity of the airfoil will be the same as the mass flow rate passing through the control valve. Since the injection line is sealed from this point to the airfoil, this principle allows for accurate measurement of the mass flow rate exiting the injection jet. A combination pressure and temperature transducer and an orifice plate with a differential pressure transducer are located downstream of the control valve. These sensors are used to find the injection mass flow rate given in Eq. (4.1). The 2" (5.08 cm) pipe leading from the control valve contains a Model 1500 (0 – 80 psia) Pressure and Temperature transducer from Spectre Sensors. Total pressure and total temperature are required for the calculations of mass flow rate. The equations are given in the *Sensors* section. This sensor has a 1/4 male NPT fitting that is tapped into the line. This sensor uses a J-type thermocouple which requires a T/C transmitter to condition the signal for the data acquisition system. A Devar SM815 Isolated T/C transmitter is used here and is attached to the line. The thermocouple wire from the transducer goes to the transmitter and regular electrical wire exits the transmitter. Fig. 4.20 and 4.21 show the pressure/temperature transducer with T/C transmitter and the differential pressure sensor with orifice plate, respectively. After 20" (50.8 cm) of straight pipe, the Oripac Model 5300 2" (5.08 cm) orifice plate is placed in the injection line. It is held in place by two flanges with rubber gaskets. A Spectre Sensors Differential Pressure Transducer Model D150 (0 – 267.7" WCD) is fitted to the line and connected to the orifice plate with 1/4 NPT taps. After the orifice plate, 10" (25.4 cm) of straight pipe are required for accurate measurement.

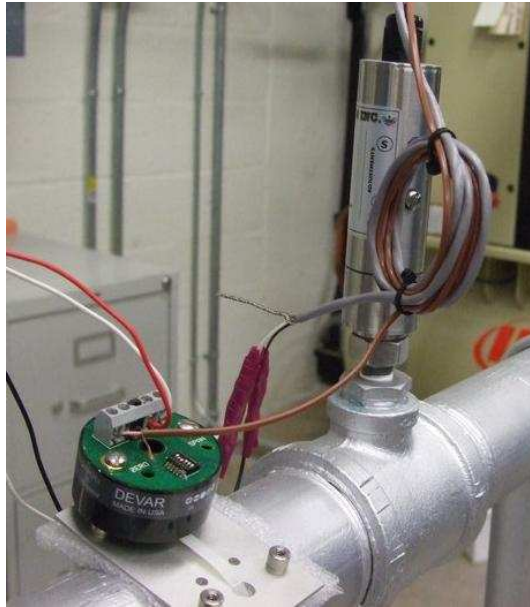


Figure 4.20: Spectre Sensors Model 1500 Pressure/Temperature Transducer



Figure 4.21: Spectre Sensors Model D150 Differential Pressure Transducer

Mass flow rate in the line can be determined from the following set of equations.

$$\dot{m} = \rho C e E \frac{\pi D_2^2}{4} \sqrt{\frac{2\Delta p}{\rho}} \quad (4.1)$$

$$E = \sqrt{\frac{1}{1 - \left(\frac{D_2}{D_1}\right)^4}} \quad (4.2)$$

Where C is the coefficient of discharge, e is the expansion coefficient, and E is given above. $D_1 = 0.0525\text{m}$ and $D_2 = 0.0368\text{m}$ and they are the small and large diameters of the orifice plate, respectively. The expansion coefficient for gases is given in Eq. (4.3) and the discharge coefficient for corner mounted taps, as in this case, is shown in Eq. (4.4).

$$e = 1 - (0.41 + 0.35\beta^4) \frac{\Delta p}{\gamma p} \quad (4.3)$$

$$\begin{aligned} C = & 0.5961 + 0.0261\beta^2 - 0.216\beta^8 + 0.000521 \left(\frac{10^6\beta}{Re}\right)^{0.7} \\ & + \left(0.0188 + 0.0063 \left(\frac{19000\beta}{Re}\right)^{0.8}\right) \left(\frac{10^6}{Re}\right)^{0.3} \beta^{3.5} \\ & + (0.043 + 0.08 - 0.123) \left(1 - 0.11 \left(\frac{19000\beta}{Re}\right)^{0.8}\right) \frac{\beta^4}{1 - \beta^4} \end{aligned} \quad (4.4)$$

The ratio of $\frac{D_2}{D_1}$ is given as β for simplicity and $\gamma = 1.4$. The diameter used for Re calculations is D_1 because this is where the density, viscosity, and velocity are acquired. To find the velocity, the mass flow rate is required from $V = \frac{\dot{m}}{\rho A}$. However, the mass flow equation needs C , which needs Re . This circular reference is solved with only a few iterations. The viscosity for Re is determined by the temperature in

the line from the pressure/temperature sensor and by using Sutherland's Law, shown in Eq. (4.5). The density is found using the state equation (Eq. (2.13)) with pressure and temperature readings taken from the sensor upstream.

$$\mu = \mu_o \left(\frac{T}{T_o} \right)^{3/2} \frac{T_o + 110}{T + 110} \quad (4.5)$$

Here, μ_o and T_o are reference viscosity and temperature given by $\mu_o = 1.7894 \times 10^{-5} \text{ kg/m} \cdot \text{s}$ and $T_o = 288.16 \text{ K}$. All of the above equations are calculated and iterated appropriately in the *Labview* program, giving an output of injection mass flow rate.

After the mass flow measurement equipment, the piping continues to the wind tunnel box connection for injection air. Along the way, the pipe diameter is decreased from 2" (5.08 cm) to 1" (2.54 cm) as it prepares to enter the sting and finally the injection cavity. As mentioned before, the final connection from the injection line to the box is completed by a high pressure flexible hose with a 3/4 NPT male swivel connection to the rotating outer circular plate. The air then travels through the hollow sting extender, through the balance and the sting, and into the airfoil. The injection air is made uniform by the aluminum foam that spans the interior of the airfoil.

On the downstream side of the aluminum foam, at the midpoint of the span, the total pressure and temperature are measured. A 12" (30.48 cm) pitot probe from Flow Kinetics (model K12-1/4) has a male 1/4 NPT thread and connects to the hole provided in the airfoil's endplate, refer to Fig. 2.7. The output of the probe extends outside of the airfoil into the wind tunnel box. Another pressure/temperature transducer (0 – 80 psia) from Spectre Sensors is used to acquire the data. A pressure rated clear flexible hose with an OD of 1/4" and an ID of 1/8" is attached to the end of the pitot probe and connects to the transducer via an 1/8" barbed hose fitting to a female 1/4 NPT coupler. A J-type T/C wire is carefully attached to the pitot probe

to measure the temperature inside the cavity, taking care not to touch any metal with the tip. The T/C wire extends out of the airfoil, via the small hole just aft of the NPT thread for the pitot probe, and connects to another Devar temperature transmitter. Again, regular electrical wires run from the transmitter to the data acquisition system. This total pressure and total temperature are used to calculate the jet velocity and injection C_μ using Eq. (4.6) and (4.7), where $K = 0.040416 \frac{\sqrt{K_s}}{m}$, A_{jet} is the 2-D area of the injection jet outlet, and \dot{m} is the mass flow rate calculated from Eq. (4.1). $\frac{A}{A^*}$ is the ratio of area to the critical choke area.

$$\frac{A}{A^*} = \frac{K P_o A_{jet}}{\dot{m} \sqrt{T_o}} \quad (4.6)$$

$$\frac{A}{A^*} = \frac{1}{M} \left[\left(\frac{2}{1+\gamma} \right) \left(1 + \left(\frac{\gamma-1}{2} \right) M^2 \right) \right]^{\frac{1+\gamma}{2(\gamma-1)}} \quad (4.7)$$

The isentropic relation given in Eq. (4.7) shows the ratio of critical areas as a function of Mach number, which is used to derive the jet velocity. This relation is non-linear and the known value of $\frac{A}{A^*}$ must be interpolated from acquired values based on a given Mach number. $\frac{A}{A^*}$ will have two values for Mach number, one subsonic and one supersonic. The subsonic value is used since the maximum jet speed will not be greater than the speed of sound due to the geometry of the injection cavity. This process is performed within the *Labview* program using an interpolation function. With the subsonic Mach number determined, $V_{jet} = M_{jet} \sqrt{\gamma R T}$ with T being the temperature measured in the injection cavity. With the determination of V_{jet} and \dot{m} (from Eq. (4.1)) are used in Eq. (1.1), which yields the value for C_μ .

4.3.2 Test Section and Aerodynamic Forces

A total and static pressure pitot probe and a J-type thermocouple are located inside the test section upstream of the airfoil model. This equipment was provided with

the purchase of the wind tunnel. This pitot probe is connected to an MKS Type 223B Differential Pressure Transducer, located inside of an MKS Type 660B Power Supply. This unit connects to the data acquisition system with a serial cable. The T/C wire connects to a conditioning module that accepts standard thermocouple wire directly. The static line of the pitot probe is connected to a Spectre Sensor Model 1000 Pressure Transducer (0 – 17 psia) with a clear tube and NPT/barbed coupler, in the same manner as the injection cavity pressure transducer. The wind tunnel velocity, density, and temperature are calculated with these sensors and are used as ambient values for non-dimensional parameters. Eq. (4.8) calculates the velocity, where $\Delta p = (p_o - p)$ from the differential pressure transducer and ρ is the density calculated using the static pressure and temperature measured in the wind tunnel (see Eq. (2.13)).

$$V = \sqrt{\frac{2\Delta p}{\rho}} \quad (4.8)$$

To obtain the aerodynamic forces produced by the airfoils, a 6 component force balance was used. It was necessary to have a balance that the injection air could travel through since the air delivery and balance connection are located in the same place on the CFJ airfoil model. Advanced Mechanical Technology, Inc. (AMTI) produces such a force balance with their model MC2.5B-2K-SS-5024. This unit requires the MSA-6 MiniAmp Signal Conditioner/Amplifier for 6 channels. The connection cable from the balance to the conditioner was also provided by AMTI. This balance has a range of 1000 lb (4448 N) in the Fx and Fy directions and 2000 lb (8896 N) in the Fz. It has a range of 1000 in-lb (113 $N \cdot m$) for the moments Mx, My, and Mz. The x, y, and z-directions are the same as they were described earlier with +Fx pointing upstream in the test section, +Fy pointing up, and +Fz pointing from the airfoil to the balance. The balance is cylindrical shaped and the sting mounts to it with a circular bolt pattern, as shown in Fig. 4.11.

Since the airfoil is fixed to the sting, the inner and outer circular aluminum plates rotate simultaneously when the angle of attack is changed. For this reason, the force balance rotates around its Fz axis and therefore the Fy and Fx directions rotate as well. This is significant because the lift and drag forces must be measured perpendicular to the free stream flow. Due to this shift, the true lift and drag forces are comprised of the vertical and horizontal components of the Fy and Fx forces felt by the balance. Calculations including the rotated angle of the outer circular plate are used to determine the actual lift and drag. Once the airfoil is rotated, α is measured using a digital level on the horizontal surface of the endplate extrusion that connects to the sting. This value is recorded in the front panel of the *Labview* interface as the AoA. From the *SolidWorks* models, it was measured that this extruded surface is actually -0.36° from the horizontal. Let this angle be the α correction angle. Hence, $\alpha_{true} = \alpha_{measured} - (-0.36^\circ)$, where $\alpha_{measured}$ is the measured angle of the flat extruded surface on the endplate. The positive angle convention is based on the positive angle of attack of the airfoil model. Fig. 4.22 shows correction angle between the chord of the airfoil and the flat extruded square where α is measured.

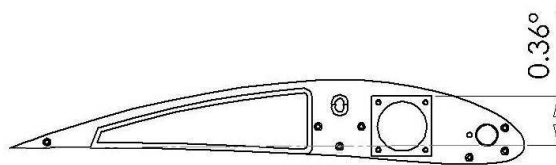


Figure 4.22: Illustration of α Correction Angle

A calibration procedure was used to determine the true Fx and Fy of the balance. With the sting extender bolted to the outer aluminum plate and the balance tightly screwed to the extender, known weights were hung from the balance. The outer plate was rotated slightly until the Fx reading was 0.00N on the front panel of the program. At this angle, the horizontal surface of the square flange was measured with the digital level and the value was recorded at 0.7° as the back plate correction angle. This angle

shows what the back plate measures when the balance is at 0° . The combination of the back plate correction angle and the back plate measured angle could then be used to determine the force components in the x and y-directions and ultimately, the true lift and drag. Eq. (4.9) and (4.10) show these relations. If these equations are used, then the resulting lift and drag will be correct regardless of whether the measured back plate angle is positive or negative.

$$L = F_y \cos(-\theta_{BPM} + \theta_{BPC}) - F_x \sin(-\theta_{BPM} + \theta_{BPC}) \quad (4.9)$$

$$D = F_y \sin(-\theta_{BPM} + \theta_{BPC}) - F_x \cos(-\theta_{BPM} + \theta_{BPC}) \quad (4.10)$$

Here, θ_{BPM} is the measured back plate angle and θ_{BPC} is the back plate correction angle in radians. From these equations, the values of C_L and C_D were found using Eq. (3.17) and (3.18), with the free stream velocity and density determined by the pressures and temperatures measured inside of the wind tunnel test section. The force seen by the balance in the Fz direction and the pitching moment, given by Mz, are the true values regardless of rotation. The moment coefficient, C_M is given by the following equation, where C is the chord length of the model.

$$C_M = \frac{M_z}{\frac{1}{2}\rho_\infty V_\infty^2 SC} \quad (4.11)$$

4.3.3 Suction Line

A total pressure pitot probe is located in the suction manifold to measure pressure in the suction cavity. The probe has a 1" (2.54 cm) length and has a 1/8 male NPT fitting for connection to the provided NPT tap in the suction manifold. The outlet of the probe uses clear flexible tube to connect to a barbed hose/female NPT coupler, in the same manner as the pitot probe in the injection cavity. This suction

tube connects to a Spectre Sensors Pressure/Temperature Transducer Model 1500 (0 – 29.5" HGV) with a J-type thermocouple. This sensor has a range designed for low pressure vacuum conditions. The T/C wire is not used in the suction cavity.

As the suction air enters the suction cavity from the slot, it travels downstream through the manifold and flexible hoses to the suction line. This pipe has a 3" (7.62 cm) diameter as it leaves the wind tunnel box and expands to 4" (10.16 cm) before it reaches the suction line pressure and temperature sensor. Similar to the injection line, the suction line requires a Spectre Sensors Model 1500 Pressure/Temperature Transducer (0 – 29.5" HGV). This sensor also has a male 1/4 NPT that is tapped into the line. This pressure and temperature are used to calculate the suction mass flow rate. The suction line needs a larger 4" Lambda Square Oripac Model 5300 Orifice Plate with connection to a Spectre Sensors Differential Pressure Transducer Model D150 (0-116.9" H₂O). This is the same set up as the injection line, just using different range transducers for vacuums. Also, 40" (101.6 cm) of straight pipe are necessary upstream of the orifice plate and 20" (50.8 cm) are needed downstream. From mass conservation, the suction cavity mass flow rate is also calculated by Eq. (4.1)-(4.5) using the values from the suction line pressures and temperature.

Downstream of the orifice plate, after the 20" of straight pipe, the line decreases again to a 3" (7.62 cm) diameter for the manual Bronze Gate Valve-Class 125, with a 3" NPT female fitting. This valve is from McMaster Carr and is used to control the flow on the suction side. Once the target mass flow rate is achieved with the electro-pneumatic valve, the gate valve is adjusted until the suction and injection mass flow rates are within 5% of each other. After this valve, the piping leads to the 600 gal. vacuum tank. A 4" (10.16 cm) diameter outlet on the tank leads the pipe to the vacuum pump which is exhausted to the outside of the lab. A full list of sensors and controllers used, with their locations, are given in table 4.1. A flowchart showing the locations of each sensor and controller is given in the appendix.

	Sensor	Reading	Location
1	Electro-pneumatic control valve	Open/Close Valve	Inj. line
2	(0-80 psia) Pres/temp transducer	p_s	Inj. line
3	Temperature transmitter	T	Inj. line
4	(0-267.7" WCD) Differential pressure	Δp	Inj. line
5	(0-80 psia) Pres/Temp transducer	p_o	Inj. cavity
6	Temperature transmitter	T	Inj. cavity
7	(0-17 psia) Pressure transducer	p_s	Test section
8	MKS Differential pressure	Δp	Test section
9	Thermocouple	T	Test section
10	(0-29.5" HGV) Pres/Temp transducer	p_o	Suc. cavity
11	(0-29.5" HGV) Pres/Temp transducer	p_s	Suc. line
12	Temperature transmitter	T	Suc. line
13	(0-116.9" H ₂ O) Differential pressure	Δp	Suc. line
14	AMTI force balance	F _x , F _y , M _z	Test section
15	Wind tunnel motor control	Hz of motor	Wind Tunnel

Table 4.1: Sensors and Controls

4.3.4 Data Acquisition System and *Labview*

The output of each sensor must be conditioned and the result needs to be converted to engineering units to be useful. The data acquisition system utilizes signal conditioning modules as the data is input into the *Labview* test stand. The entire experiment consists of 12 input signals and 2 outputs. The range of each sensor relates linearly to a 4-20 mA signal that is received by the DAQ (data acquisition system). From table 4.1, sensors 2-7 and 10-13 are input into signal conditioning current input modules from National Instruments (SCC-C120). Each module has 2 channels, so each module can accommodate 2 sensors. The modules are configured in a SC-2345 signal conditioning box, also from National Instruments. A PCI-6229 Data Acquisition Card from NI was needed for the test stand computer to read the signals from the sensors. Sensor 9 from the table uses a SCC-TC02 module that is designed to condition thermocouple wire directly. The MKS Differential Pressure Transducer (sensor 8) connects directly to the DAQ using a serial port. This module performs its own conditioning. An analog output module, SCC-A010, was used to control the wind tunnel motor frequency

from the test stand. The electro-pneumatic control valve used a SCC-C020 module to provide the valve with a 4-20 mA current output. All of the input sensors, with the exception of the test section Δp and temperature, were wired to a power supply from Advanced Technology Associates (model 24VDC 30W, 1.3 A). This provided the sensors with their required excitation voltages. Fig. 4.23 shows the signal conditioning modules, with their labels, in the SC-2345 box. Each sensor is wired to the power supply and to its signal conditioning module. The positive wire of the sensor goes to the positive terminal of the power supply and the negative wire of the sensor goes to the negative terminal of the conditioning module. The circuit is completed by a wire connecting the negative terminal of the module to the negative terminal of the power supply.



Figure 4.23: Signal Conditioning Modules

The *Labview* Program for the CFJ Wind Tunnel Laboratory was developed using the above equations by an outside company. Mark Schmitt from Precision Test and Automation is a Certified National Instruments Programmer and he worked with students and faculty to develop the program. Each wind tunnel test gathers data from every sensor and calculates the mass flow rates and jet velocities internally in real time. The data can be acquired at a range of frequencies from 2 Hz to 50 Hz. The slowest piece of equipment is the MKS differential pressure transducer at 2 Hz.

The other sensors, including the force balance can acquire at 50 Hz. The program was developed so that the slowest data collection is incorporated at the highest frequency, and shows no hindrance at that speed. The front panel of the test stand is displayed on two screens that are shown in Fig. 4.24 and 4.25. A detailed procedure for testing is included in the appendix.

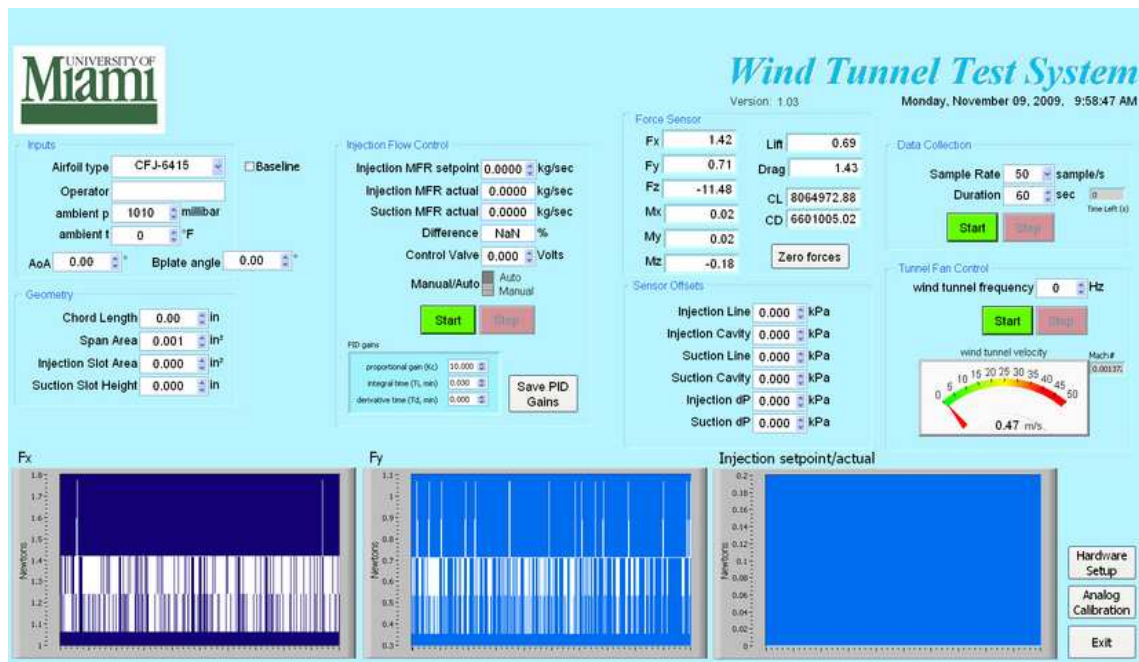


Figure 4.24: Front Panel of CFJ Wind Tunnel Laboratory Test Stand: Screen 1

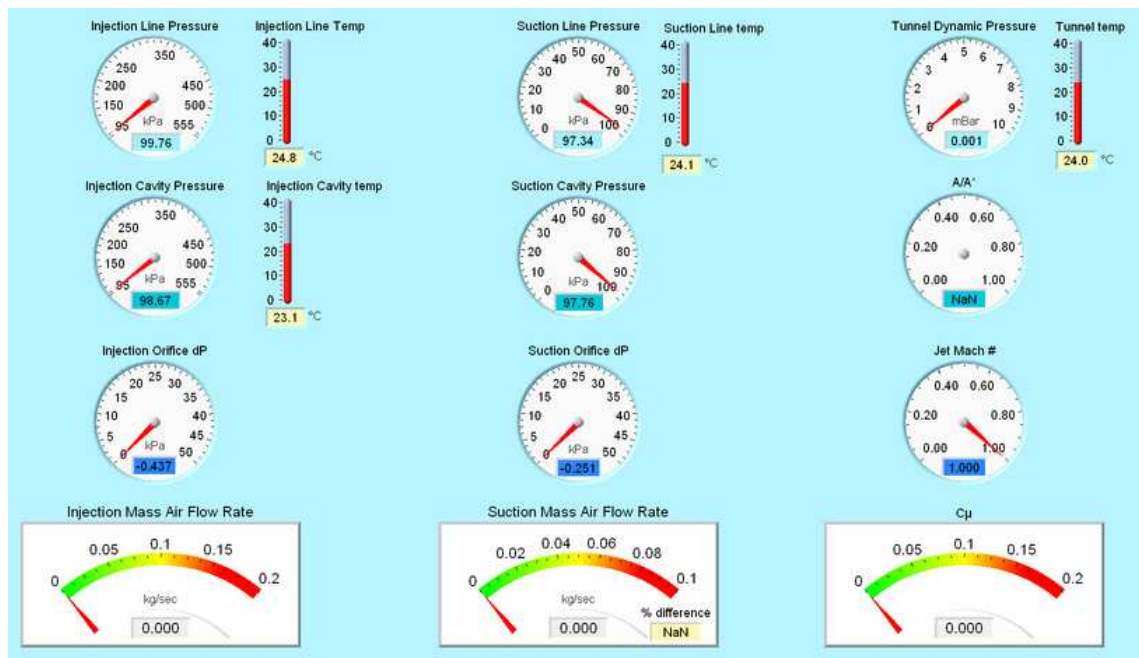


Figure 4.25: Front Panel of CFJ Wind Tunnel Laboratory Test Stand: Screen 2

4.4 Uncertainty Analysis

An uncertainty analysis was conducted for the experimental wind tunnel results. Each measured value acquired from the sensors has a given uncertainty. The resulting values discussed in Eq. (4.1)-(4.8) include the measured uncertainties of each sensor used in the calculation. The uncertainties, in percent, of each sensor are shown in table 4.2.

Sensor	Uncertainty
(0-80 psia) Pres/Temp Transducer	0.1%
Temperature Transmitter	0.1%
(0-267.7" WCD) Differential Pressure	0.5%
(0-17 psia) Pressure Transducer	0.1%
MKS Differential Pressure	0.5%
Thermocouple in Wind Tunnel	0.1%
(0-29.5" HGV) Pres/Temp Transducer	0.1%
(0-116.9" H ₂ O) Differential Pressure	0.5%
AMTI Force Balance, F _y	0.99%
AMTI Force Balance, F _x	0.20%

Table 4.2: Uncertainties of Sensor Equipment

The uncertainties for all sensors, except for the force balance, were provided by the manufacturers. Calibration tables for the AMTI force balance were provided by the company for a full scale 10-point loading range. Since the maximum load for the balance is 1000 lbs (4448.22 N), each load check was given in increments of 100 lbs (444.82 N). An additional calibration was required for a smaller range of applied loads used during testing of the baseline and CFJ airfoils. For this calibration procedure, known weights were applied in the +F_y, -F_y, +F_x, and -F_x directions. Then each load was applied three times and the readout values were averaged. This readout was compared to the known loads to obtain the uncertainty of the balance in the lower range. In each case, the line of best fit was 100% linear. Figures 4.26- 4.29 show the results of this calibration procedure.

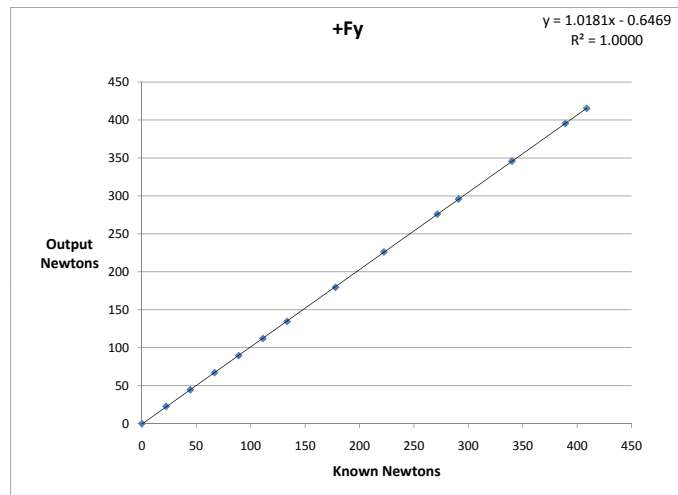


Figure 4.26: Force Balance Calibration Curve, +F_y Direction

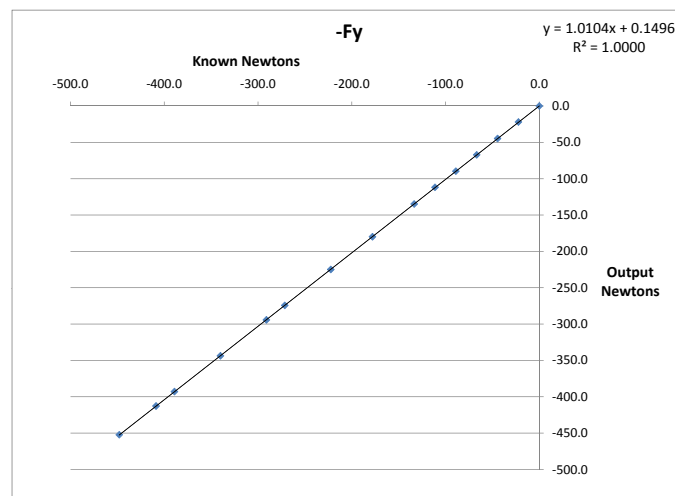


Figure 4.27: Force Balance Calibration Curve, -F_y Direction

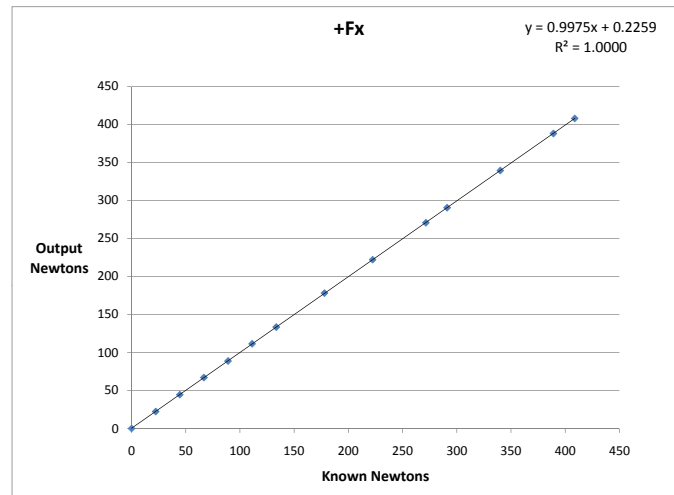


Figure 4.28: Force Balance Calibration Curve, +Fx Direction

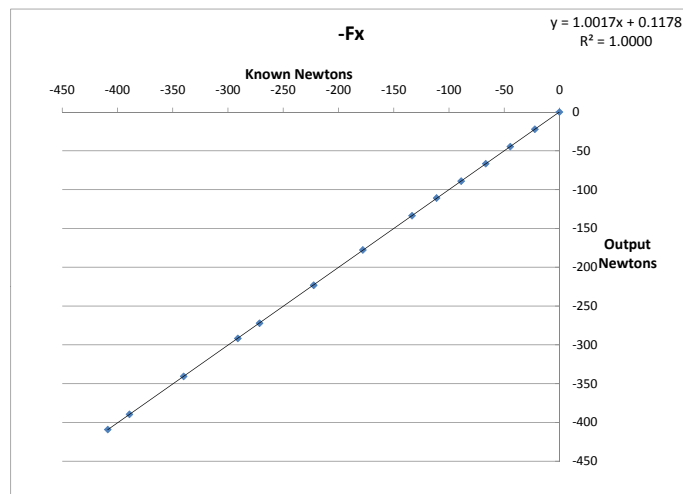


Figure 4.29: Force Balance Calibration Curve, -Fx Direction

The uncertainties in the Fy direction (taking values from the +Fy and -Fy loadings) range from 0.18% to 1.88% with the loadings shown in Fig. 4.26 and 4.27. The average of uncertainty is 0.99%. In the Fx direction, the range of uncertainty is from $8 \times 10^{-4}\%$ to 0.55% with an average of 0.20%, with the loadings shown in Fig. 4.28 and 4.29. For each experiment, the data is collected at 50 Hz for 60 seconds. This large amount of data, taken at each angle for each airfoil case, makes individual uncertainty analysis impractical. The uncertainty for the lift and drag coefficients will therefore be calculated using the average Fx and Fy uncertainty percents. This is reasonable because the range of uncertainty for each direction is very small. The standard deviations for experimental lift and drag coefficients are given in the *Results* chapter.

The uncertainty for any calculated value R is given in Eq. (4.12). Here, R is any equation with independent variables x_1, x_2, \dots, x_j . U_R is the uncertainty of value R , including the uncertainties of the independent variables $U_{x_1}, U_{x_2}, \dots, U_{x_j}$. These uncertainties for each variable are given in Table 4.2. Each uncertainty parameter (x) listed is a percentage determined as $\frac{\Delta x}{x}$. Each independent uncertainty variable given in an equation is weighted by its order in the equation [29,30]. For example, if $R = x^2y$ then $U_R = \sqrt{2(U_x)^2 + U_y^2}$. Equations 4.13- 4.20 follow this example.

$$U_R = \sqrt{U_{x_1}^2 + U_{x_2}^2 + \dots + U_{x_j}^2}$$

$$R = R(x_1, x_2, \dots, x_j) \quad (4.12)$$

Eq. (4.12) can be used to determine the uncertainties of the injection and suction mass flow rates, the C_μ value, and the lift and drag coefficients. In Eq. (4.1), used to calculate the mass flow rates, the measured values include the differential pressure, static pressure, and temperature in the injection line. Density comes from the state

equation, $(\rho = \frac{P}{RT})$, so the uncertainty of this density is shown in Eq. (4.13). Constant values do not have an uncertainty.

$$U_\rho = \sqrt{U_P^2 + U_T^2} \quad (4.13)$$

The mass flow calculation also includes the quantities C and e from Eq. (4.4) and (4.3). The uncertainty for the expansion coefficient (e) is given in Eq. (4.14).

$$U_e = \sqrt{U_{\Delta P}^2 + U_P^2} \quad (4.14)$$

The discharge coefficient includes the Re in the line. Viscosity, density, and velocity are needed to calculate Reynolds number. Viscosity comes from Sutherland's Law shown in Eq. (4.5) and its uncertainty is given in Eq. (4.15). Eq (4.16) shows the uncertainty of velocity which uses the dynamic pressure across the orifice plate and the density uncertainty is given above.

$$U_\mu = \sqrt{1.5(U_T)^2 + U_T^2} \quad (4.15)$$

$$U_V = \sqrt{0.5(U_{\Delta P})^2 + U_\rho^2} \quad (4.16)$$

From equations (4.13), (4.15), and (4.16), the Reynolds number uncertainty can be calculated using Eq. (4.17). With U_{Re} , the uncertainty for the discharge coefficient can be calculated and then the final uncertainty for mass flow rate is given in Eq. (4.18). The uncertainties for all parameters discussed are given in table 4.3. These values are the same for both the suction and injection mass flow rates since the measured uncertainties are the same for both sides.

$$U_{Re} = \sqrt{U_\rho^2 + U_\mu^2 + U_V^2} \quad (4.17)$$

$$U_{\dot{m}} = \sqrt{U_{\rho}^2 + U_C^2 + U_e^2 + 0.5(U_{\Delta P})^2 + 0.5(U_{\rho})^2} \quad (4.18)$$

Parameter	Uncertainty
U_{ρ}	0.1414%
U_e	0.5099%
U_{μ}	0.1581%
U_V	0.3674%
U_{Re}	0.4243%
U_C	0.6841%
$U_{\dot{m}}$	0.9397%

Table 4.3: Mass Flow Measurement Uncertainties

Along with the uncertainty of the mass flow measurements, the jet velocity uncertainty is also needed to calculate the total uncertainty of the C_{μ} values. Eq. (4.6) and (4.7) calculate the jet velocity using the total pressure and temperature readings from inside the injection cavity. Eq. (4.19) calculates the corresponding uncertainty of A/A^* . Since the Mach number was determined from interpolating the A/A^* function, its uncertainty is equal to the uncertainty of A/A^* . The jet velocity uncertainty can be found using the jet Mach uncertainty and the temperature in the cavity. This is shown in Eq. (4.20). Table 4.4 shows the uncertainties of each parameter used to calculate the total jet velocity uncertainty.

$$U_{A/A^*} = \sqrt{U_p^2 + 0.5(U_T)^2 + U_{\dot{m}}^2} \quad (4.19)$$

$$U_{V_{jet}} = \sqrt{0.5U_T^2 + U_M^2} \quad (4.20)$$

Uncertainties for the free stream density and velocity are the final values necessary to calculate the total uncertainty of C_{μ} . This velocity is determined using the differential pressure, static pressure, and temperature inside of the wind tunnel test section. Eq. (4.13) and 4.16 can be used to find these uncertainties using the input

Parameter	Uncertainty
U_{in}	0.9397%
$U_{A/A*}$	0.9476%
U_M	0.9476%
$U_{V_{jet}}$	0.9503%

Table 4.4: Jet Velocity Uncertainties

uncertainties of the wind tunnel parameters. The final uncertainty for C_μ can be determined from Eq. (4.21).

$$U_{C_\mu} = \sqrt{U_{in}^2 + U_{V_{jet}}^2 + 2(U_{V_\infty})^2 + U_{\rho_\infty}^2} \quad (4.21)$$

To determine the uncertainties of C_L and C_D , the uncertainties of lift and drag force must be determined first. For this calculation, the average uncertainty for F_y and F_x are used from table 4.2. Since the lift and drag forces are the sums of the vertical and horizontal force components, respectively, the uncertainties of each are derived from Eq. (4.9) and (4.10). Eq. (4.22) and (4.23) are used to determine uncertainties of lift and drag coefficients. Table 4.5 gives the final uncertainties for C_L , C_D , and C_μ . Standard deviations for each value are given in the *Results* chapter.

$$U_{C_L} = \sqrt{U_L^2 + U_{\rho_\infty}^2 + 2(U_{V_\infty})^2} \quad (4.22)$$

$$U_{C_D} = \sqrt{U_D^2 + U_{\rho_\infty}^2 + 2(U_{V_\infty})^2} \quad (4.23)$$

Parameter	Uncertainty
U_L	1.0100%
U_D	1.0100%
U_{C_L}	1.1446%
U_{C_D}	1.1446%
U_{C_μ}	1.1441%

Table 4.5: Final Uncertainties for C_L , C_D , and C_μ

Chapter 5

Results

5.1 Numerical Simulations

CFD analysis of a 3-dimensional NACA 6415 baseline and a CFJ 6415-065-142 airfoil show the significant performance enhancements provided by the co-flow jet flow control method. Two CFJ cases were simulated using a momentum coefficient of $C_\mu = 0.05$ and $C_\mu = 0.1$. For all three cases, non-dimensional lift and drag were determined for a full range of angles of attack up until stall. The jet reactionary forces, which provide a detriment to the lift, were included in the final results for the CFJ airfoil. CFD results from every AoA in the baseline and CFJ cases were processed after at least 30,000 time steps. Each case had a residual reduction of at least 3 orders of magnitude, with some cases reducing 5 orders. The lift and drag coefficients for the baseline case will be used as a comparison for C_L and C_D obtained from the CFJ simulations. Pressure and Mach contours with streamlines are also obtained from the CFD results. For the baseline case, 2-dimensional mach contours with streamlines and 3-dimensional surface pressure contours are shown before stall at $\alpha = 10^\circ$. The mach contours shown in Fig. 5.1 are from a cross section of the airfoil located at the midpoint of the span. Fig. 5.2 demonstrates that the simulated flow

has high 2-dimensionality. From these streamlines, no cross flow is visible along the span of the airfoil. This desired result is due to the boundary condition assignment done during pre-processing.

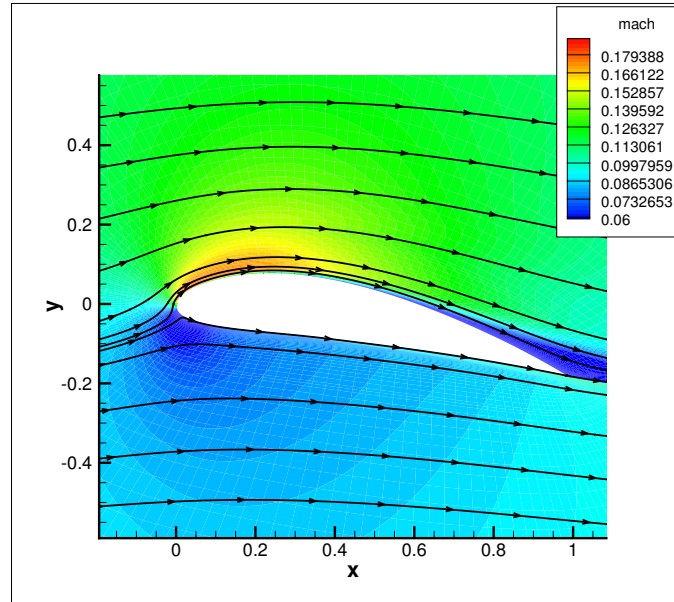


Figure 5.1: Baseline Mach Contours w/Streamlines, $\alpha = 10^\circ$

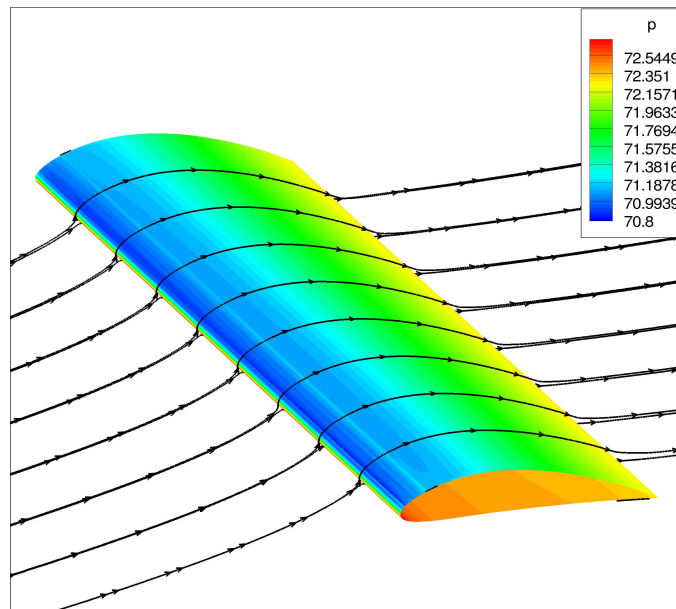


Figure 5.2: Baseline 3-D Surface Pressure, $\alpha = 10^\circ$

Streamlines at the stall angle, $\alpha = 15^\circ$, begin to separate along the suction surface of the baseline airfoil. Fig. 5.3 shows the surface pressures with streamlines and the 2-D cross section of mach contours. The streamlines begin to recirculate due to turbulent separation at stall and are more visible in the cross section of Fig. 5.4.

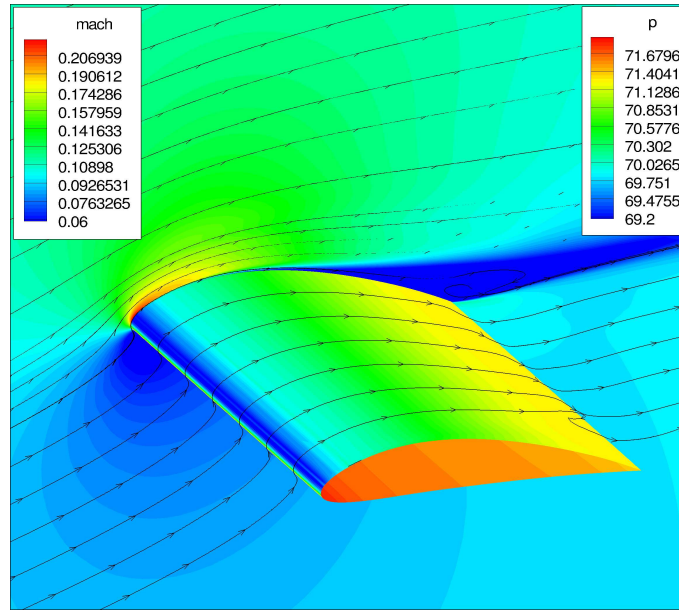


Figure 5.3: Baseline 3-D Surface Pressure and 2-D Mach Contours, $\alpha = 15^\circ$

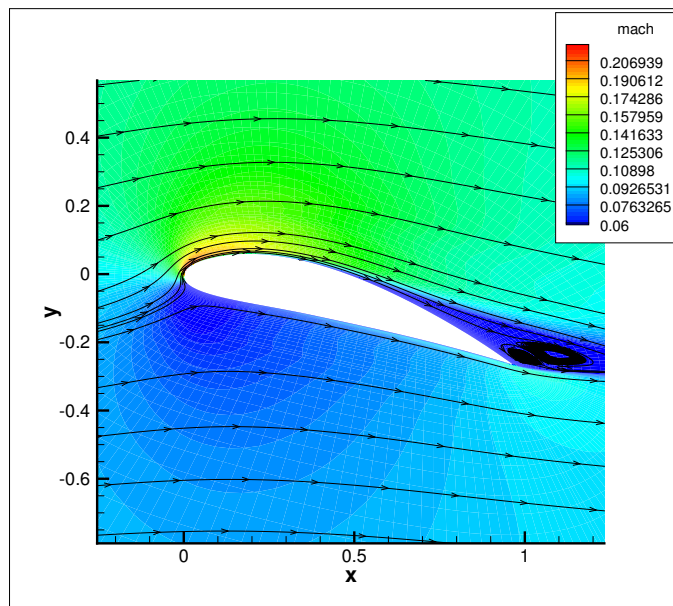


Figure 5.4: Baseline 2-D Mach Contours w/Streamlines, $\alpha = 15^\circ$

Using the baseline results as a control, the CFJ results certainly demonstrate the benefits of this flow control method. The C_L and C_D plots comparing the baseline, CFJ with $C_\mu = 0.05$, and CFJ with $C_\mu = 0.1$ are given in Fig. 5.5 and 5.6.

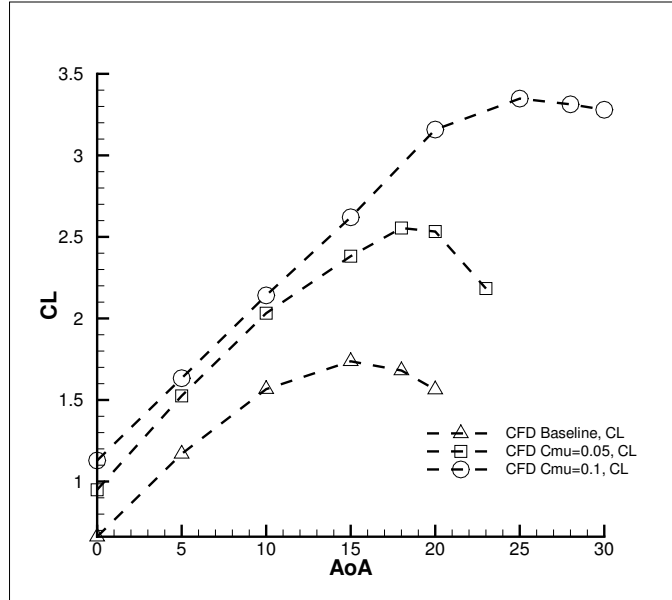


Figure 5.5: C_L vs. α for All CFD Cases

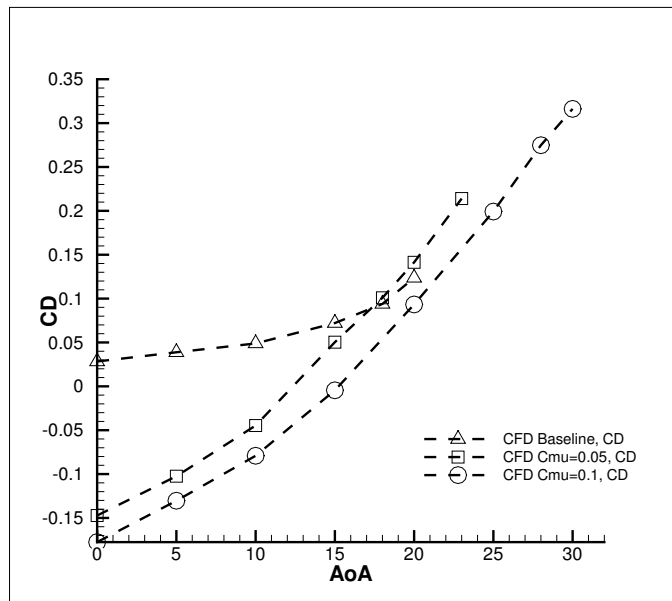


Figure 5.6: C_D vs. α for All CFD Cases

A significant increase in lift for the CFJ airfoil is evident at all angles. For the $C_\mu = 0.05$ case, C_{Lmax} increased 47.04% from the baseline airfoil, and for the $C_\mu = 0.1$ case the C_{Lmax} was augmented 92.74%. The drag coefficients from both CFJ cases shows a decrease from the baseline case. Due to the horizontal components of the jet's reactionary forces and the super suction near the leading edge at the injection jet exit, thrust is produced at low angles of attack. Negative drag, or thrust, is seen from $\alpha = 0^\circ$ to $\alpha = 10^\circ$ for the $C_\mu = 0.05$ case and from $\alpha = 0^\circ$ to $\alpha = 15^\circ$ for the $C_\mu = 0.1$ case. Drag coefficient at $\alpha = 0^\circ$ is reduced from 0.0284 for the baseline airfoil to -0.1472 for the CFJ case at $C_\mu = 0.05$. C_D is further decreased to -0.1775 for the CFJ case with $C_\mu = 0.1$. Stall margin for the CFJ airfoil was augmented from the baseline case and is considered as the angle where C_{Lmax} occurs before the lift curve drops. For $C_\mu = 0.05$, stall increased 20.00% to $\alpha = 18^\circ$ and for $C_\mu = 0.1$, the stall angle increased 66.67% to $\alpha = 25^\circ$.

For each CFJ case, the momentum coefficient was maintained as constant as possible. The value for C_μ is an output from the simulations and is only controlled by the total pressure in the injection cavity and the static pressure in the suction cavity. The mass flow rates and C_μ values produced by these pressures were periodically checked while each case was running and the pressures were adjusted as necessary. Due to this process, the momentum coefficient varies slightly from the case namesake of $C_\mu = 0.05$ or $C_\mu = 0.1$. Fig. 5.7 shows the actual C_μ values for both cases for the full range of angles tested.

Mach contours with streamlines are shown for all angles before stall for the $C_\mu = 0.05$ CFJ case in Fig. 5.8- 5.11. These plots are cross sections of the airfoil taken at the midpoint of the span. For $\alpha = 0^\circ$ to $\alpha = 10^\circ$, the flow remains smoothly attached with no vortex shedding in the wake. At $\alpha = 15^\circ$ the streamlines shown begin to separate slightly, however the lift is still increasing until stall at $\alpha = 18^\circ$. The separation in this case may be due to weaker suction at the trailing edge. Examination of the 3-D

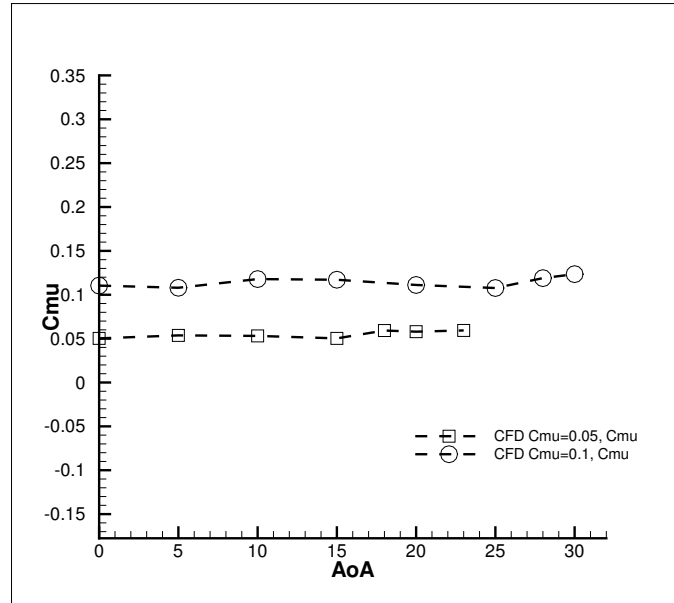


Figure 5.7: C_μ vs. α for All CFD Cases

streamlines for $\alpha = 15^\circ$ shows that the wake is not fully turbulent and C_{Lmax} will increase further until the stall angle, $\alpha = 18^\circ$.

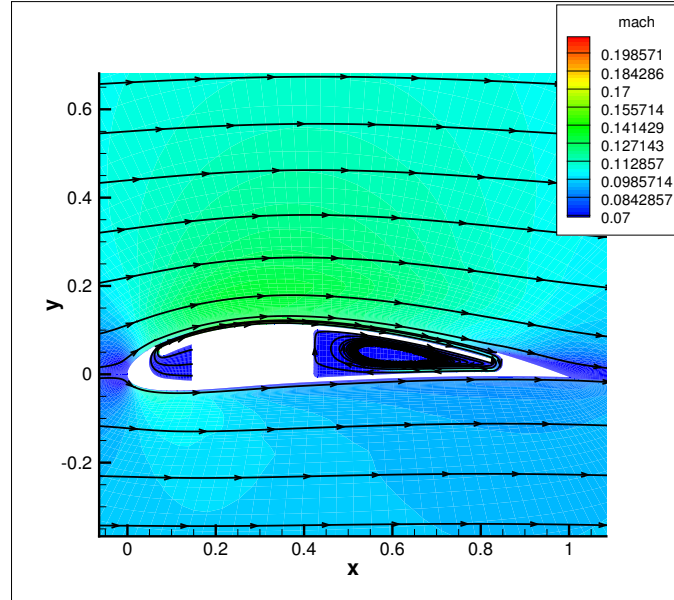


Figure 5.8: 2-D Mach Contours w/Streamlines, $C_\mu = 0.05$, $\alpha = 0^\circ$

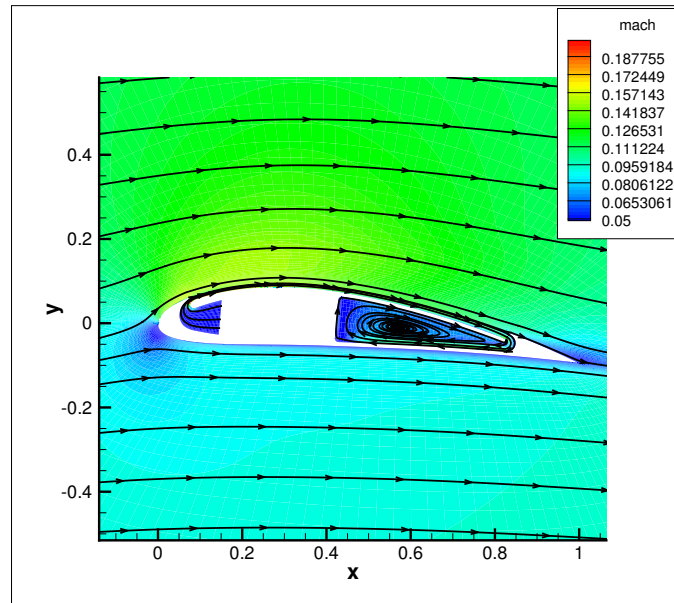


Figure 5.9: 2-D Mach Contours w/Streamlines, $C_\mu = 0.05$, $\alpha = 5^\circ$

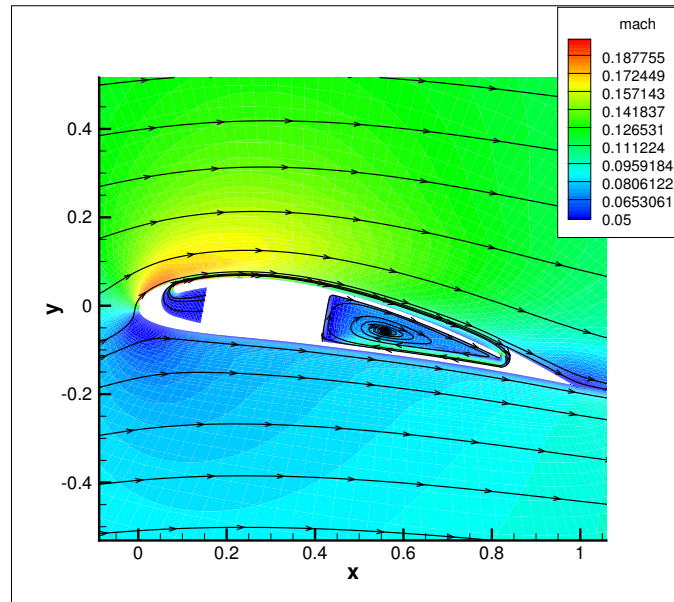


Figure 5.10: 2-D Mach Contours w/Streamlines, $C_\mu = 0.05$, $\alpha = 10^\circ$

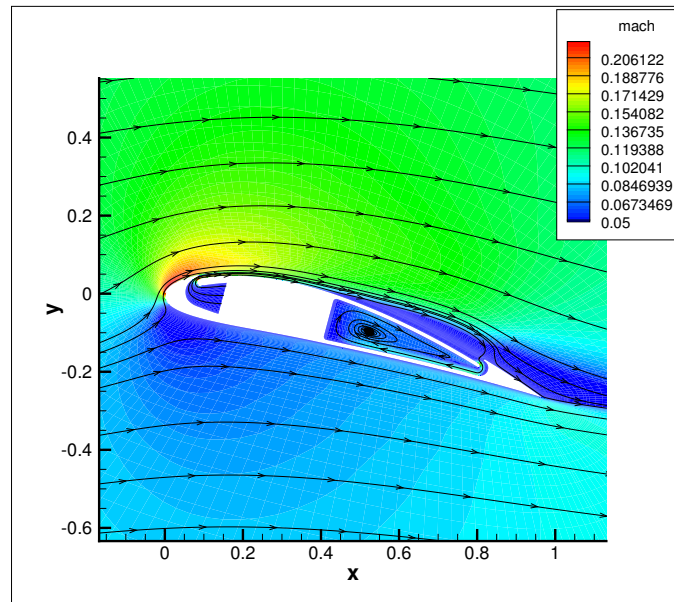


Figure 5.11: 2-D Mach Contours w/Streamlines, $C_\mu = 0.05$, $\alpha = 15^\circ$

From these plots, the high velocity jet can be seen as it exits the injection cavity. An additional figure showing a closer view of the injection jet exit enhances the mach contours in the region to show the jet more clearly. This is shown in Fig. 5.12. From Fig. 5.13, the pressure difference driving the co-flow jet is clearly visible. The 3-D pressure contour model in Fig. 5.14 shows the interior streamlines of the CFJ airfoil as they are injected along the span in the cavity and are removed at the side of the suction cavity. Again, this desired result more accurately simulates the wind tunnel experiment since the air is removed through the suction manifold on the side of the model. Finally, a plot with a combination of the Mach and pressure contours is given for the $\alpha = 15^\circ$ case in Fig. 5.15. Here, the 2-D mach contours are shown at the midpoint of the airfoil and the 3-D pressure contours are shown for the half of the airfoil on the opposite side of the suction source.

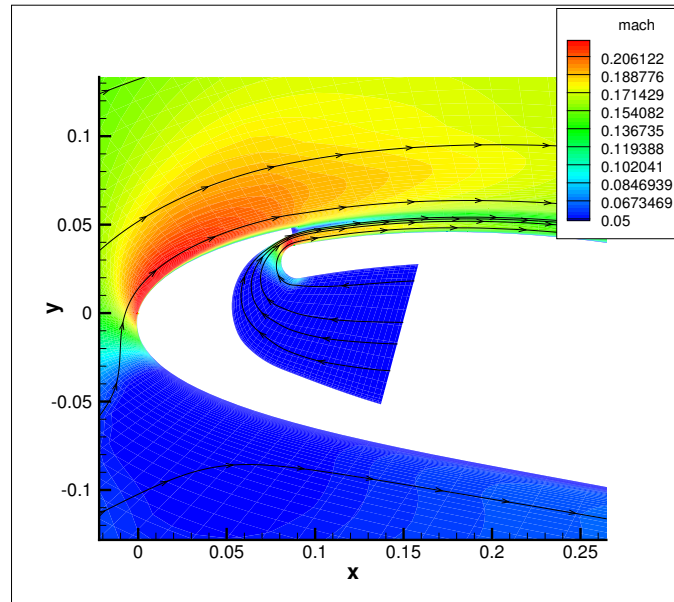


Figure 5.12: 2-D Mach Contours at Injection, $C_\mu = 0.05$, $\alpha = 15^\circ$

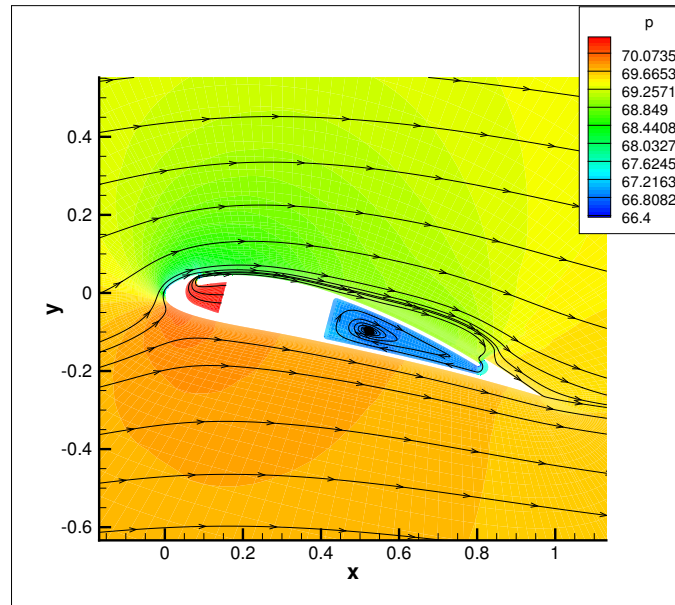


Figure 5.13: 2-D Pressure Contours w/Streamlines, $C_\mu = 0.05$, $\alpha = 15^\circ$

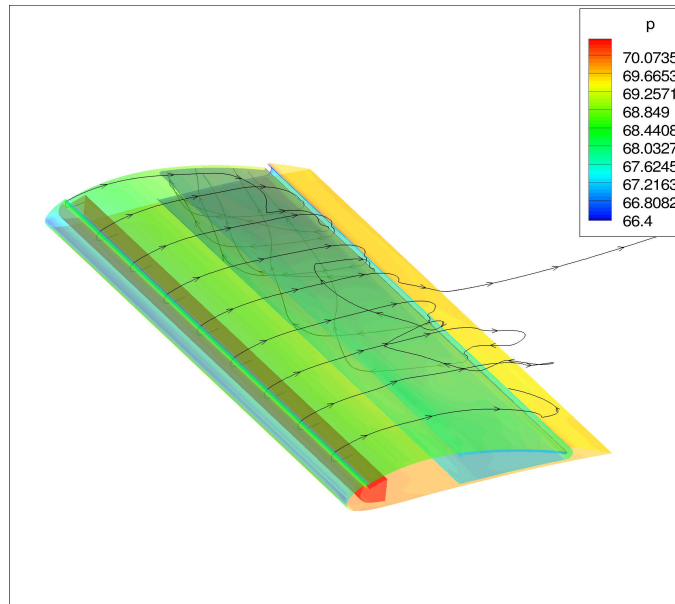


Figure 5.14: 3-D Pressure Contours w/ Interior Streamlines, $C_\mu = 0.05$, $\alpha = 15^\circ$

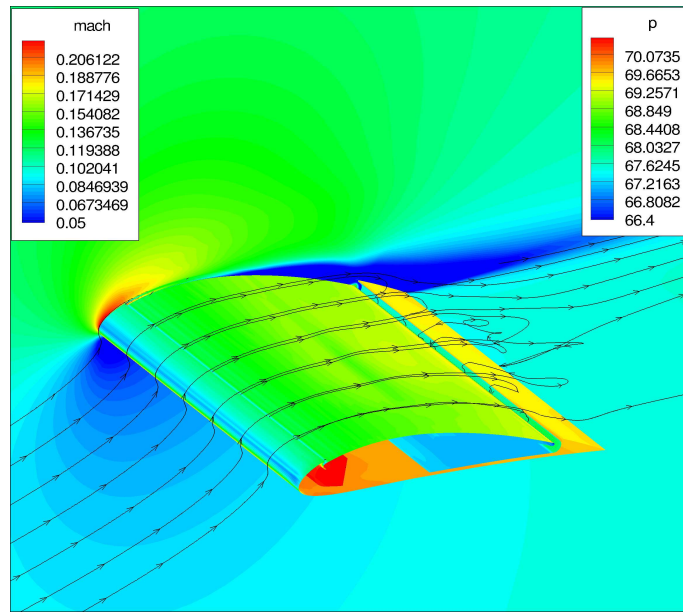


Figure 5.15: 3-D Surface Pressure and 2-D Mach Contours, $C_\mu = 0.05$, $\alpha = 15^\circ$

A fully separated case is shown with $\alpha = 18^\circ$ in Fig. 5.16. The largest separation occurs farther from the suction source. Therefore, a more uniform suction slot could produce more attached flow for this momentum coefficient.

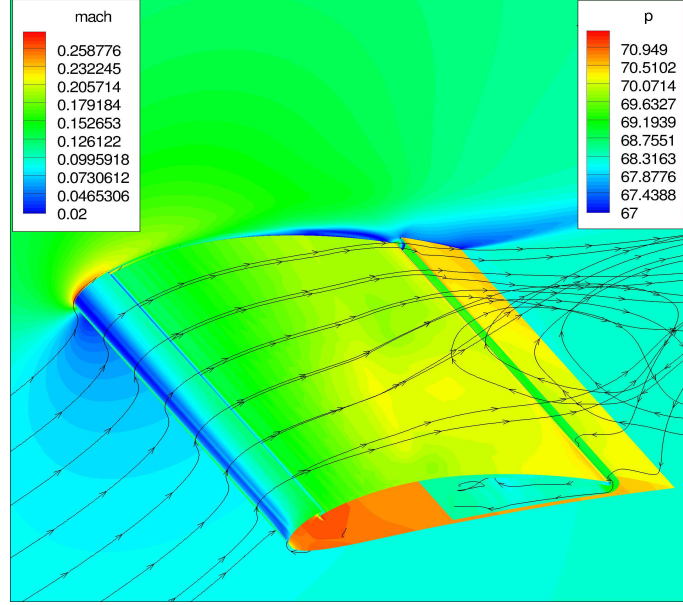


Figure 5.16: 2-D Mach Contours w/Streamlines, $C_\mu = 0.05$, $\alpha = 18^\circ$

The low momentum coefficient used for this first case shows slight improvements in flight performance. This is due to the lower jet velocity and mixing employed by the co-flow jet and this C_μ value. Examination of the $C_\mu = 0.1$ case will present more visual evidence of CFJ benefits in the streamline plots. Mach contours with streamlines are shown here for all AoA through stall for the $C_\mu = 0.1$ case in Fig. 5.17-5.21.

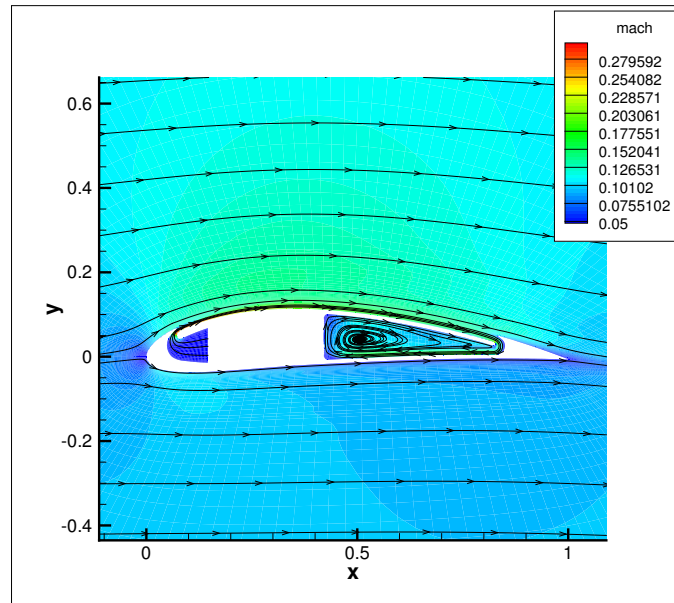


Figure 5.17: 2-D Mach Contours w/Streamlines, $C_\mu = 0.1$, $\alpha = 0^\circ$

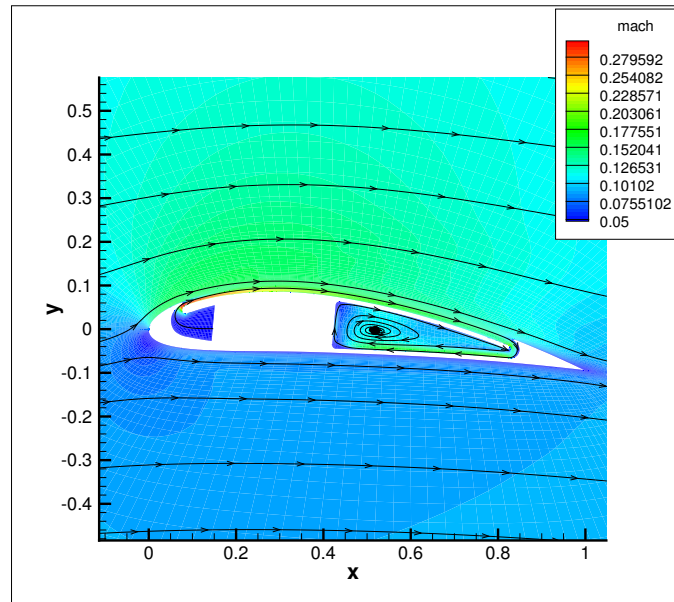


Figure 5.18: 2-D Mach Contours w/Streamlines, $C_\mu = 0.1$, $\alpha = 5^\circ$

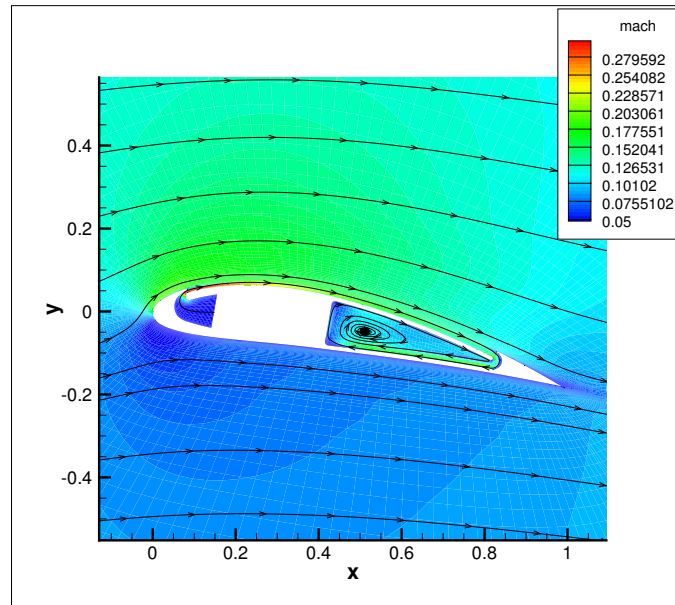


Figure 5.19: 2-D Mach Contours w/Streamlines, $C_\mu = 0.1$, $\alpha = 10^\circ$

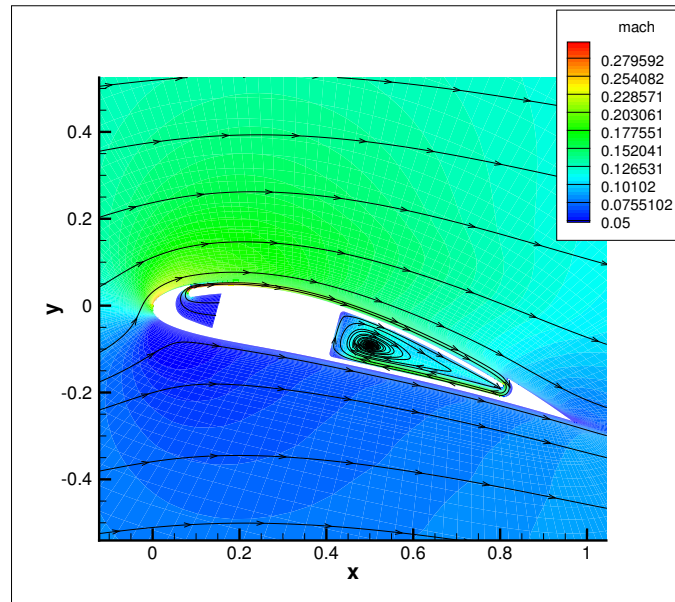


Figure 5.20: 2-D Mach Contours w/Streamlines, $C_\mu = 0.1$, $\alpha = 15^\circ$

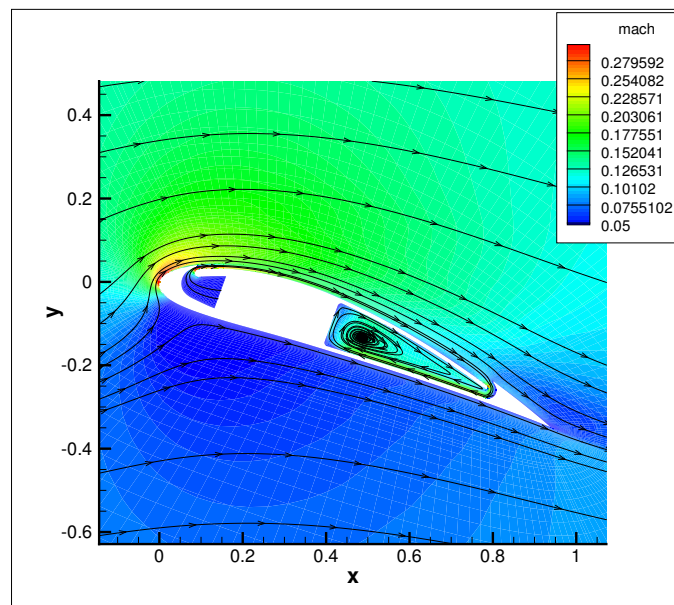


Figure 5.21: 2-D Mach Contours w/Streamlines, $C_\mu = 0.1$, $\alpha = 20^\circ$

From these plots, it is evident that the flow remains smoothly attached for angles $\alpha = 0^\circ$ to $\alpha = 20^\circ$. The 2-D Mach contours for the stall angle, $\alpha = 25^\circ$, are shown in Fig 5.22. These streamlines are shown from a 2-D cross section of the flow field at the midpoint of the airfoil. Figures 5.23- 5.26 show the 2- and 3-D pressure and mach contours with streamlines. Stall is defined as the angle where C_{Lmax} occurs. From the CFD post-processing code, with the inclusion of the jet effects, the largest C_L occurs at $\alpha = 25^\circ$. The 3-D view with streamlines shown in Fig. 5.26, illustrates separation that occurs at the far end of the airfoil opposite the suction source. At $\alpha = 28^\circ$, the separation is more visible from the 3-D view in Fig. 5.27.

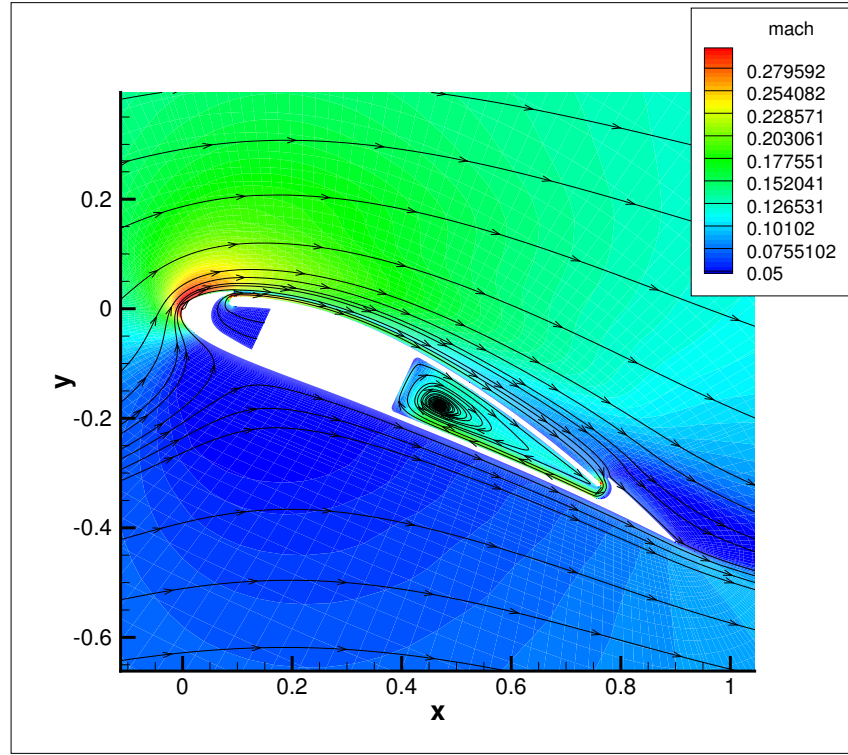


Figure 5.22: 2-D Mach Contours w/Streamlines, $C_\mu = 0.1$, $\alpha = 25^\circ$

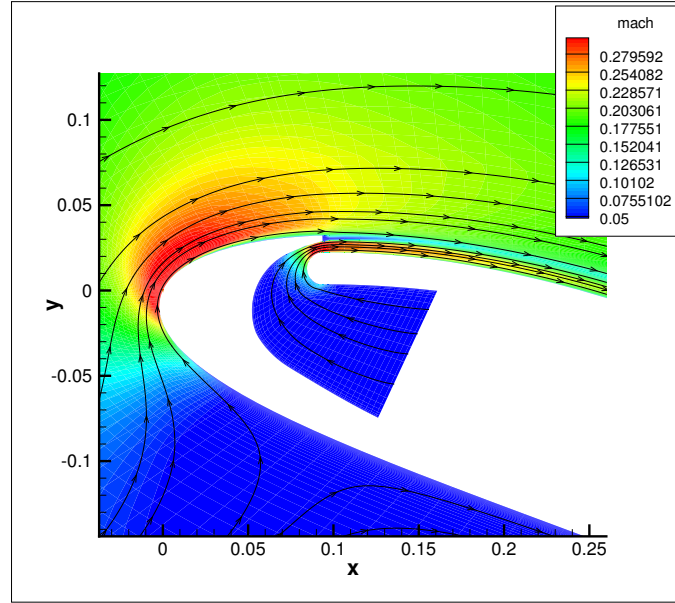


Figure 5.23: 2-D Mach Contours at Injection, $C_\mu = 0.1$, $\alpha = 25^\circ$

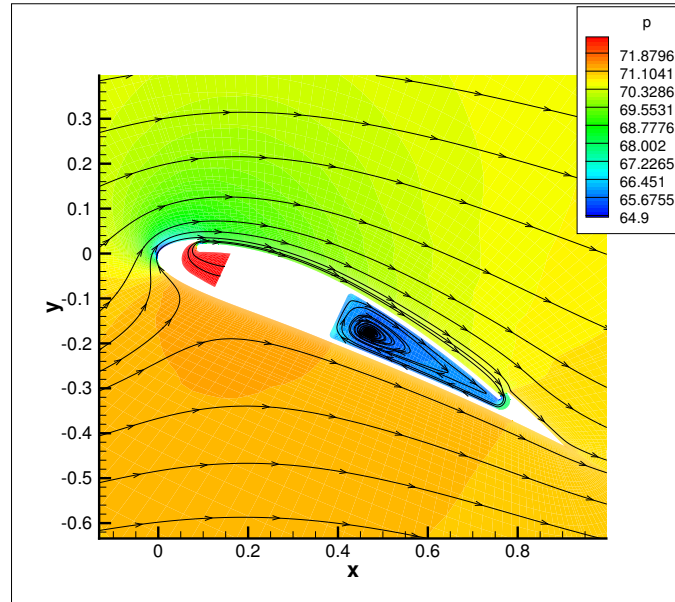


Figure 5.24: 2-D Pressure Contours w/Streamlines, $C_\mu = 0.1$, $\alpha = 25^\circ$

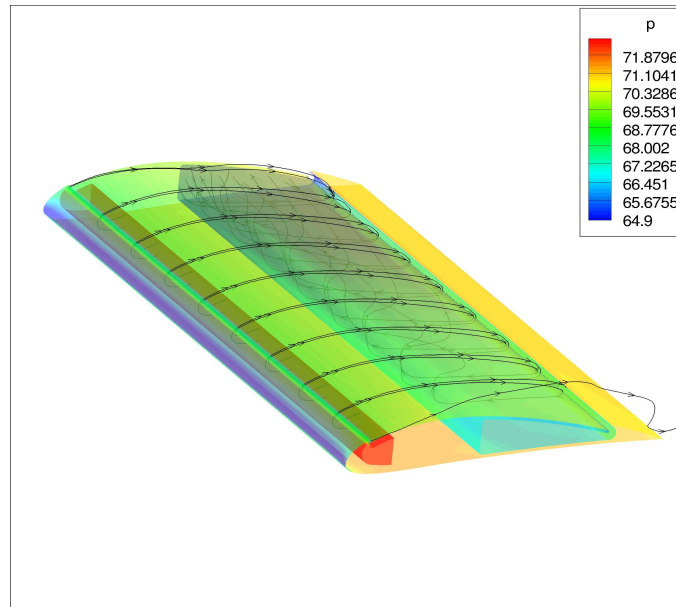


Figure 5.25: 3-D Pressure Contours w/ Interior Streamlines, $C_\mu = 0.1$, $\alpha = 25^\circ$

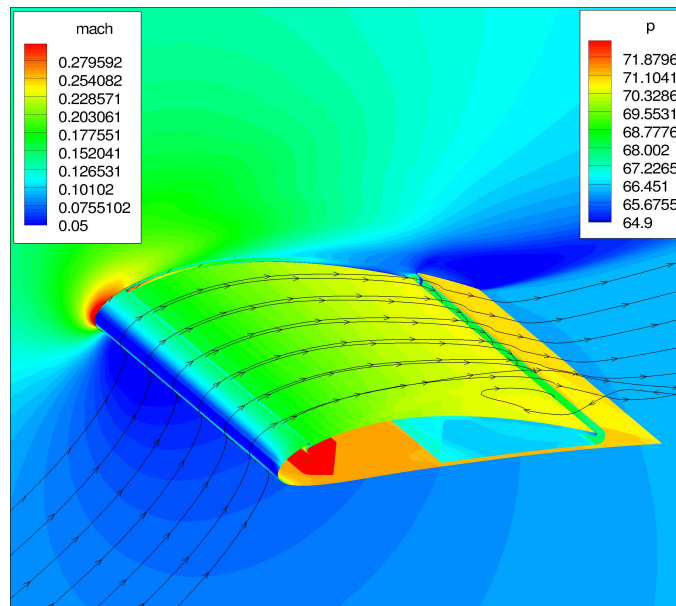


Figure 5.26: 3-D Surface Pressure and 2-D Mach Contours, $C_\mu = 0.1$, $\alpha = 25^\circ$

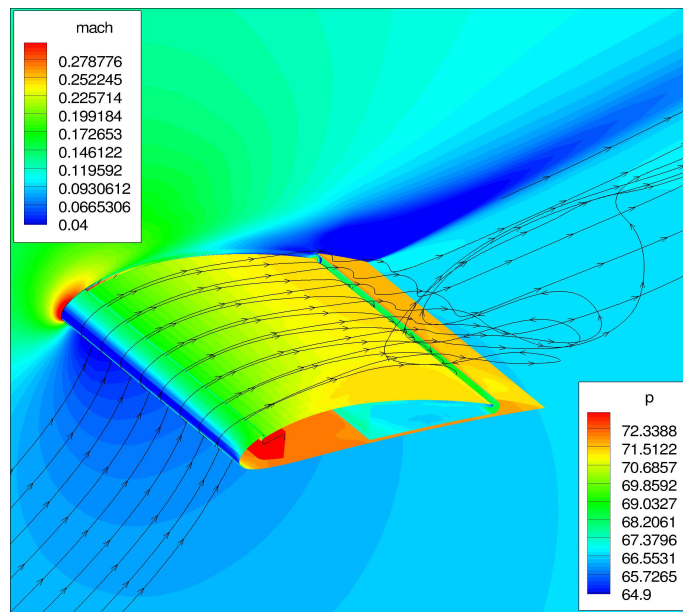


Figure 5.27: 2-D Mach Contours w/Streamlines, $C_\mu = 0.1$, $\alpha = 28^\circ$

A mesh refinement study was conducted to validate the mesh used for the above results. A larger, more refined, mesh was constructed and used with the FASIP code to compare the C_L and C_D results obtained for the baseline airfoil and for both cases of the CFJ airfoil. The number of cells of this mesh was increased by a factor of 1.5 in each direction, which is 3.375 times larger than the un-refined mesh. Simulations were run at $\alpha = 10^\circ$ and $\alpha = 20^\circ$ for all three cases. For angles with attached flow, the results matched well. As expected, the high angle results deviated more due to the separation and increased turbulence. Fig 5.28, 5.29, and 5.30 show the mesh refinement results for all cases.

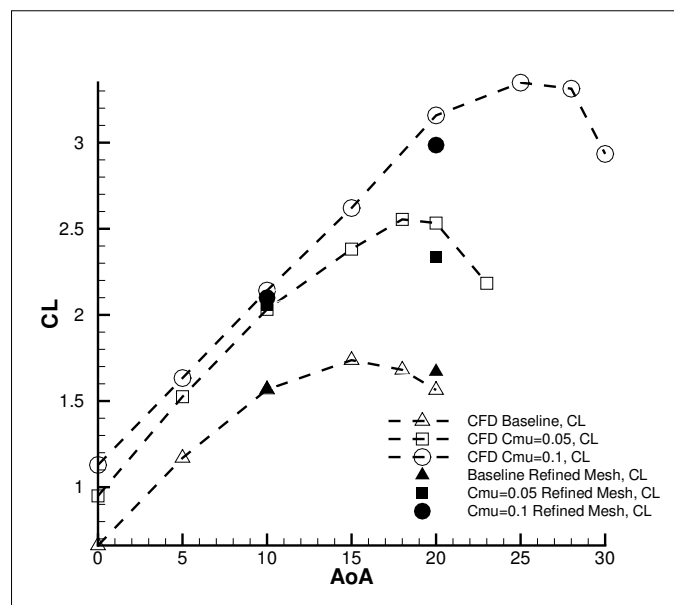


Figure 5.28: Mesh Refinement Results, α vs. C_L

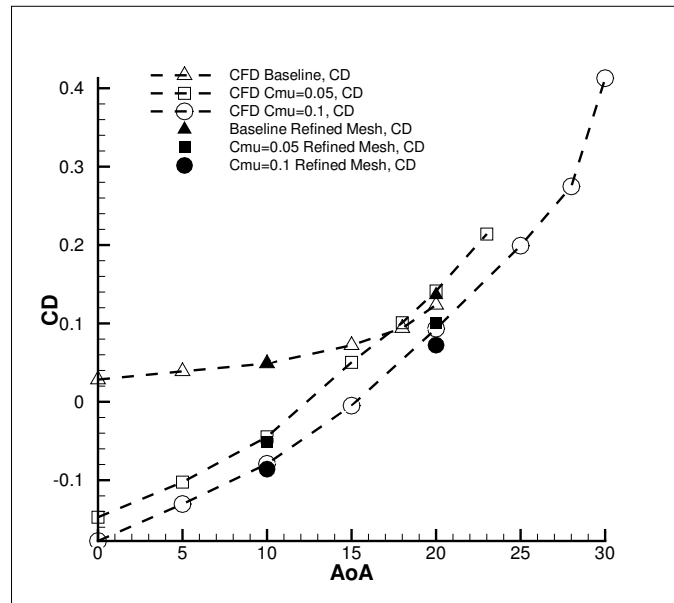


Figure 5.29: Mesh Refinement Results, α vs. C_D

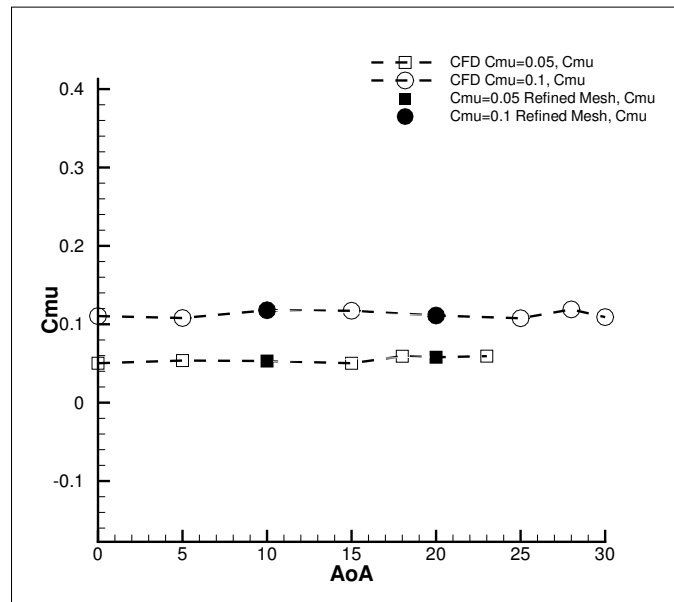


Figure 5.30: Mesh Refinement Results, α vs. C_{μ}

5.2 Experimental Results

Wind tunnel testing of the baseline and CFJ airfoils were conducted for a full range of angles until stall. The results of these tests are given in this section and a comparison analysis between the experimental and numerical results will follow in the next section. The benefits of the co-flow jet are also demonstrated experimentally. The lift and drag coefficients are based on the loads measured by the AMTI force balance and the free stream flow parameters measured inside the test section. Fig. 5.31 and 5.32 show the experimental results for lift and drag coefficient for the baseline, CFJ with $C_\mu = 0.05$, and CFJ with $C_\mu = 0.1$ cases.

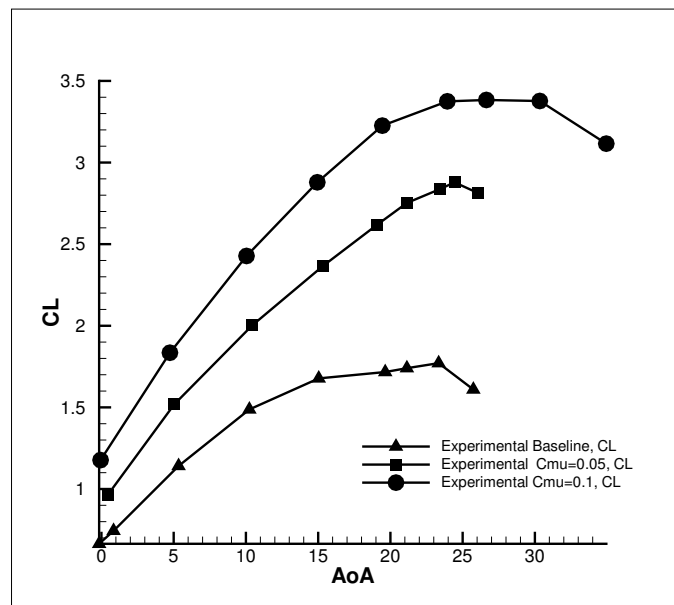


Figure 5.31: C_L vs. α for All Experimental Cases

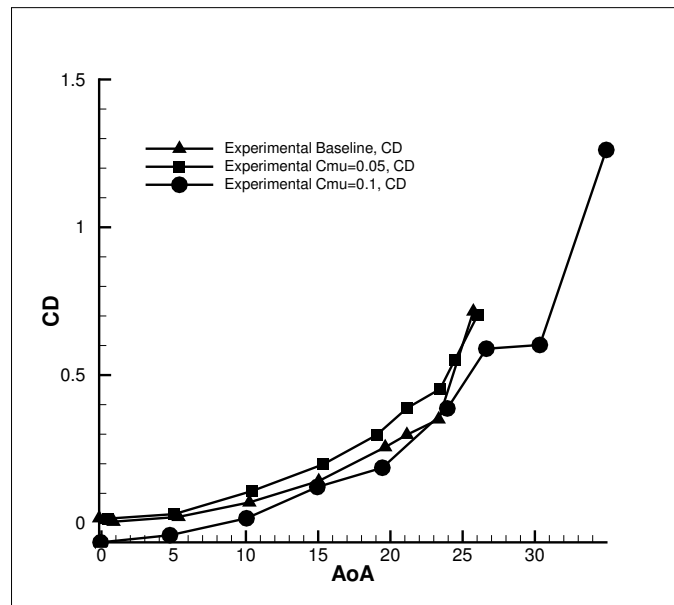


Figure 5.32: C_D vs. α for All Experimental Cases

Using the baseline case as a reference, C_{Lmax} increased 62.54% and 91.03% for the $C_\mu = 0.05$ and $C_\mu = 0.1$, respectively. A drag reduction occurred for the $C_\mu = 0.1$ case, as C_D went from 0.0041 at $\alpha = 0.85^\circ$ to -0.0658 at $\alpha = -0.06^\circ$. Drag remained negative for this case up until $\alpha = 4.74^\circ$. C_D for the $C_\mu = 0.05$ case resulted in 0.0144 at $\alpha = 0.44^\circ$. For this measured momentum coefficient, the strength of the jet and the turbulent mixing may not be enough to overcome the pressure drag induced by the geometry of the CFJ slot. As demonstrated with the CFD simulations, the suction source is located on the side of the model. This results in a non-uniform distribution of the suction across the span of the airfoil. If the CFJ model were tested without the use of the jet, the drag would be much larger than the baseline airfoil. If the jet, or the suction, is not strong enough to overcome the adverse affects of the CFJ geometry, the resulting drag may be larger than the baseline case. The present scenario is suspected for this mass flow rate because the increase in the jet momentum, as in $C_\mu = 0.1$ case, the drag is decreased from the baseline test and at low AoA it is negative. In the experimental tests, the stall margin increased 4.71% from $\alpha = 23.34^\circ$, in the baseline case, to $\alpha = 24.44^\circ$ in the $C_\mu = 0.05$ case. This value was further augmented 14.14% to $\alpha = 26.64^\circ$ in the $C_\mu = 0.1$ case. Fig 5.33 shows the momentum coefficients measured for both CFJ cases.

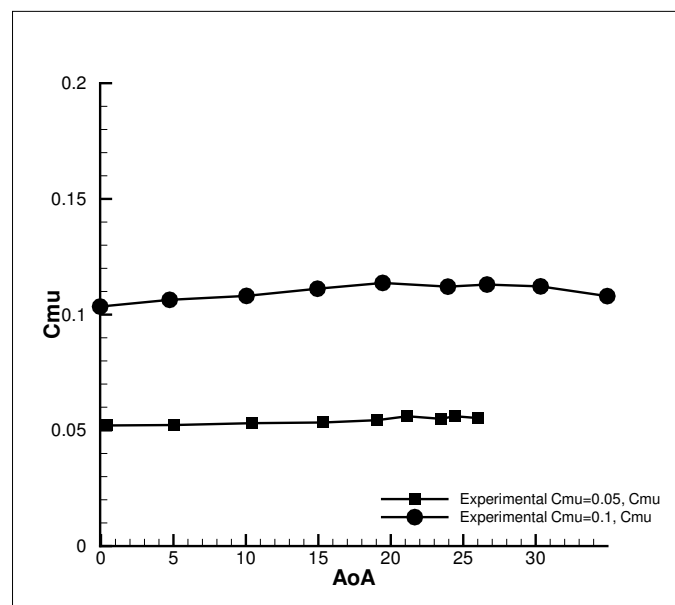


Figure 5.33: C_μ vs. α for All Experimental Cases

As the angle of attack was increased during testing, the fluctuation of the cantilevered airfoil model increased as well. As the model approached stall angles, for all three cases, vortex shedding occurred and caused oscillations, or flutter. This phenomenon resulted in larger deviations for the high angles. Fig. 5.34 and 5.35 show the error bars of one standard deviation for the average C_L and C_D values obtained. The standard deviations for each case and angle are given in tables 5.1- 5.3.

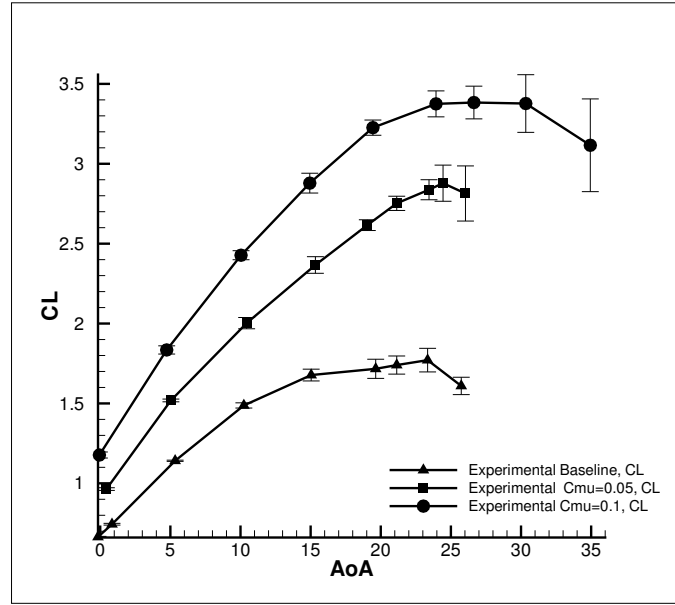
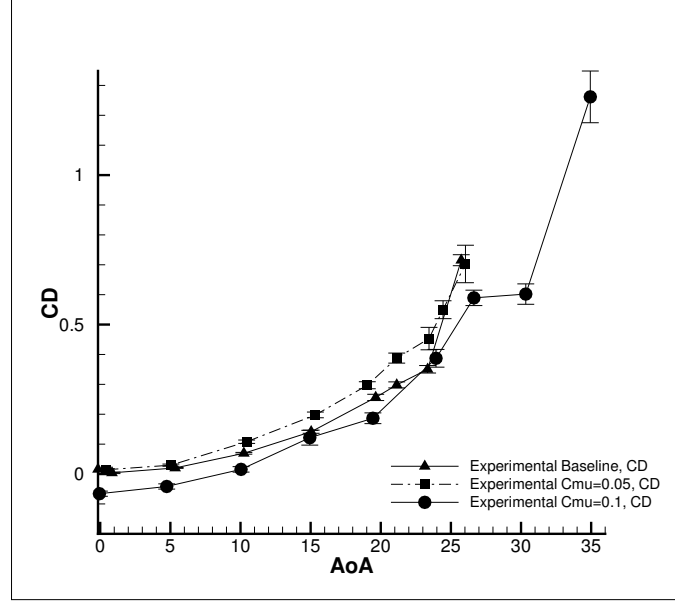


Figure 5.34: C_L vs. α with Error Bars

α	σ of C_L	σ of C_D
-0.16	0.0036	0.00161
0.84	0.0055	0.0026
5.34	0.0039	0.0014
10.24	0.0163	0.0030
15.04	0.0369	0.0053
19.64	0.0600	0.0105
21.14	0.0568	0.0101
23.34	0.0739	0.0125
25.74	0.0544	0.0184

Table 5.1: Standard Deviations of C_L & C_D , Baseline

Figure 5.35: C_D vs. α with Error Bars

α	σ of C_L	σ of C_D
0.44	0.0083	0.0035
5.04	0.0086	0.0036
10.44	0.0353	0.0057
15.34	0.0521	0.0095
19.04	0.0336	0.0117
21.14	0.0446	0.0168
23.44	0.0627	0.0375
24.44	0.1130	0.0300
26.04	0.1725	0.0627

Table 5.2: Standard Deviations of C_L & C_D , $C_\mu = 0.05$

α	σ of C_L	σ of C_D
-0.06	0.0189	0.0087
4.74	0.0257	0.0087
10.04	0.0283	0.0091
14.94	0.0620	0.0247
19.44	0.0476	0.0180
23.94	0.0812	0.0297
26.64	0.1024	0.0258
30.34	0.1805	0.03413
34.94	0.2902	0.0865

Table 5.3: Standard Deviations of C_L & C_D , $C_\mu = 0.1$

5.2.1 Comparison of Numerical and Experimental Results

A comparison of numerical and experimental results reveals that lift coefficients, in all cases, match well as shown in Fig. 5.36. Figures 5.37, 5.38, and 5.39 are presented for clarity. The FASIP simulations model the lift coefficients accurately. The stall angles differ between the numerical and experimental results, which may be due to the inadequate turbulent simulations at high angles of attack. The Baldwin-Lomax turbulence model, used in this research, does not model separation well. The task of accurately simulating high turbulence and separation is a complex issue. Also, during the experiments, large fluctuations occurred at AoA near stall, thus generating oscillating force patterns that were averaged for final results.

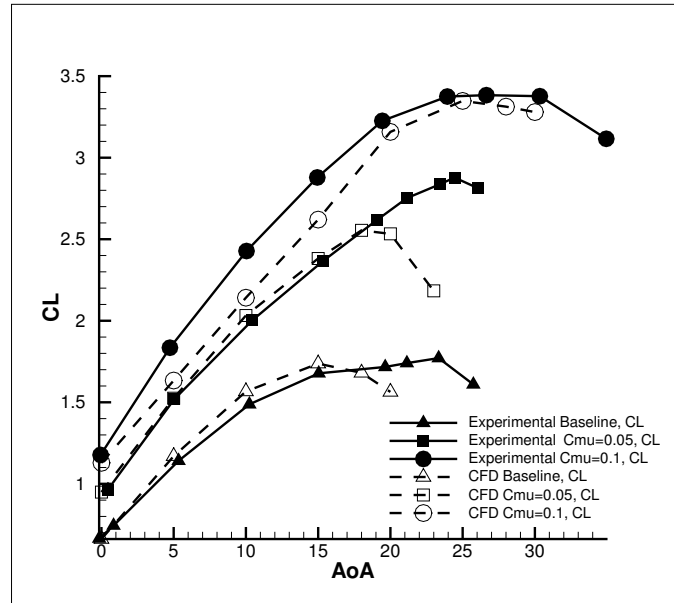


Figure 5.36: Numerical and Experimental Comparison of All Cases, C_L

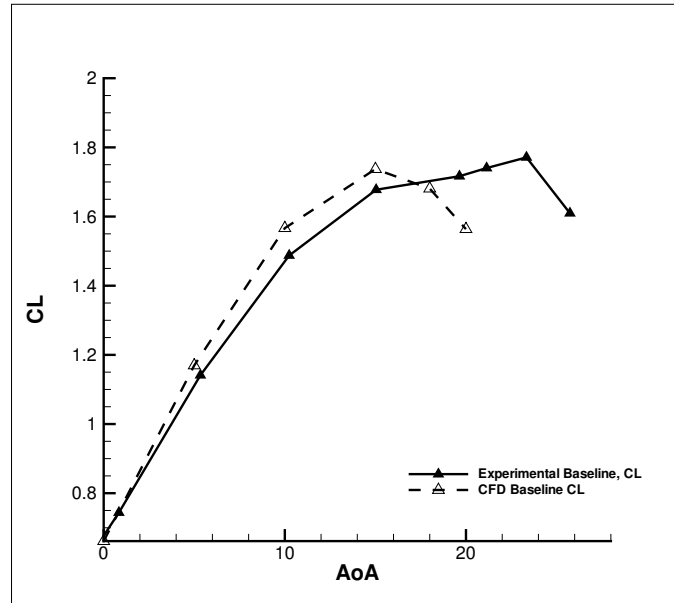


Figure 5.37: Numerical and Experimental Comparison Baseline Case, C_L

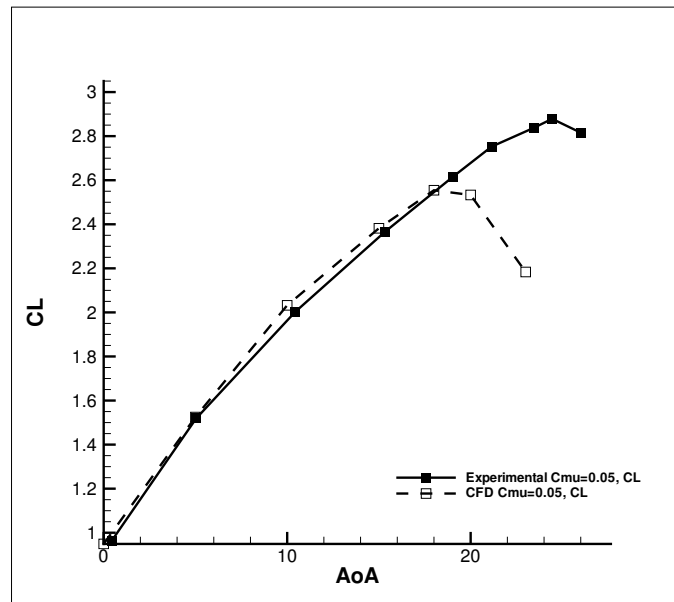


Figure 5.38: Numerical and Experimental Comparison of $C_{\mu} = 0.05$ Case, C_L

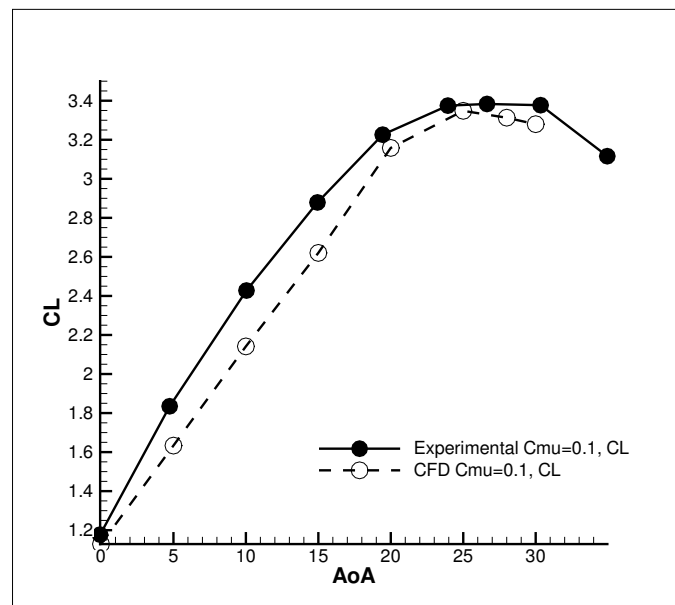


Figure 5.39: Numerical and Experimental Comparison of $C_{\mu} = 0.1$ Case, C_L

A comparison of numerical and experimental drag is presented in Fig. 5.40- 5.43. Simulated drag is under predicted compared to experimental results. The RANS (Reynolds Averaged Navier Stokes) equations used within the code do not model drag or mixing accurately [24]. Wind tunnel drag also includes some features that were not modeled in the CFD simulation. The air delivery and sensor connections, located on the side of the airfoil, utilized openings in the test section wall. As flow moves past these sections, the boundary layer is disturbed and has increased turbulence much earlier than expected with the CFD analysis. The wall effects could therefore attribute to the higher drag forces measured in the experiment. Furthermore, small gaps between the model and the test section walls were necessary so that the airfoil would not receive any unwanted forces. These gaps are not included in the mesh for the FASIP code. This localized low pressure zone could be inducing more drag on the airfoil.

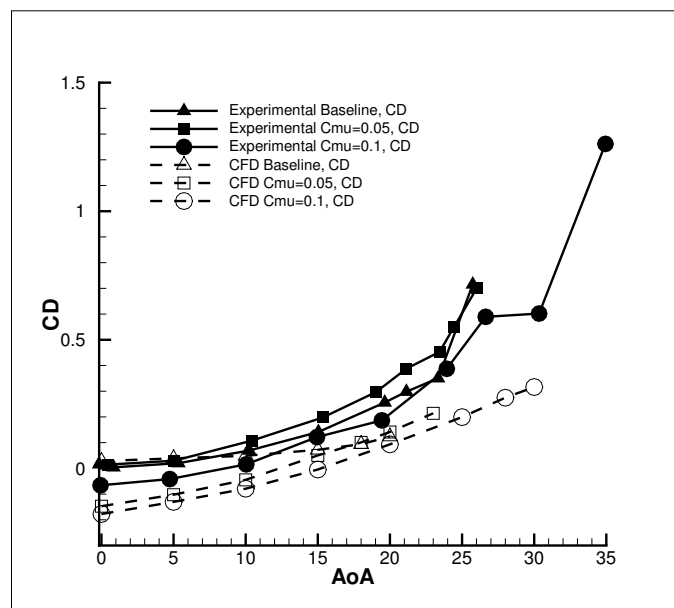


Figure 5.40: Numerical and Experimental Comparison of All Cases, C_D

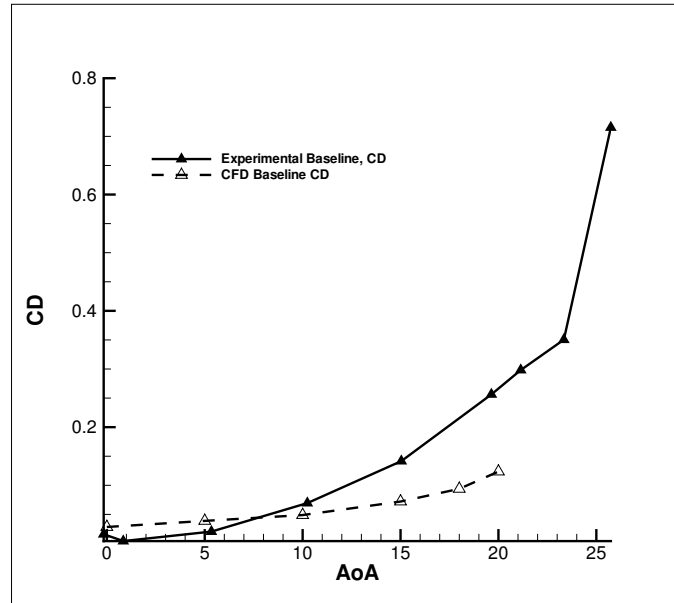


Figure 5.41: Numerical and Experimental Comparison of Baseline Case, C_D

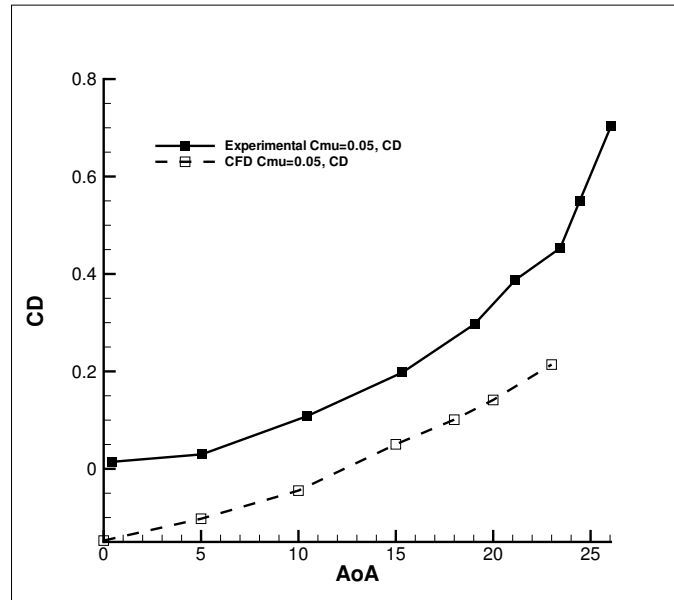


Figure 5.42: Numerical and Experimental Comparison of $C_{\mu} = 0.05$ Case, C_D

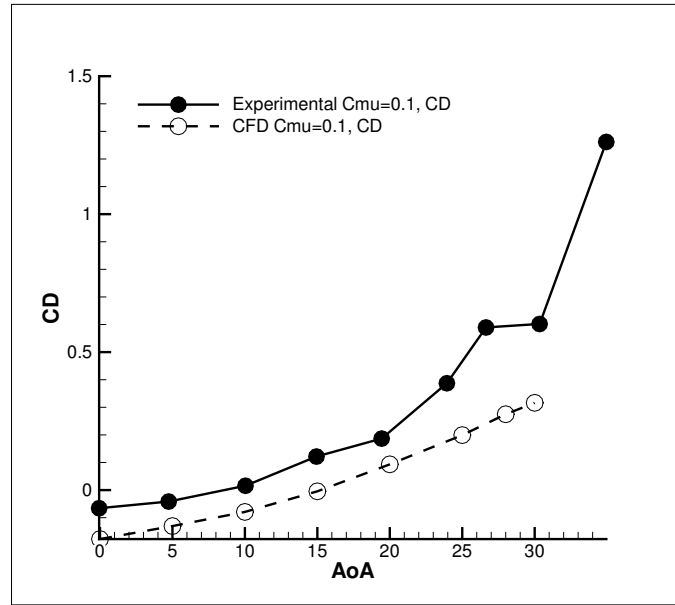


Figure 5.43: Numerical and Experimental Comparison of $C_\mu = 0.1$ Case, C_D

A comparison of the momentum coefficient values is shown in Fig. 5.44 and 5.45. The results for both cases have similar values for C_μ .

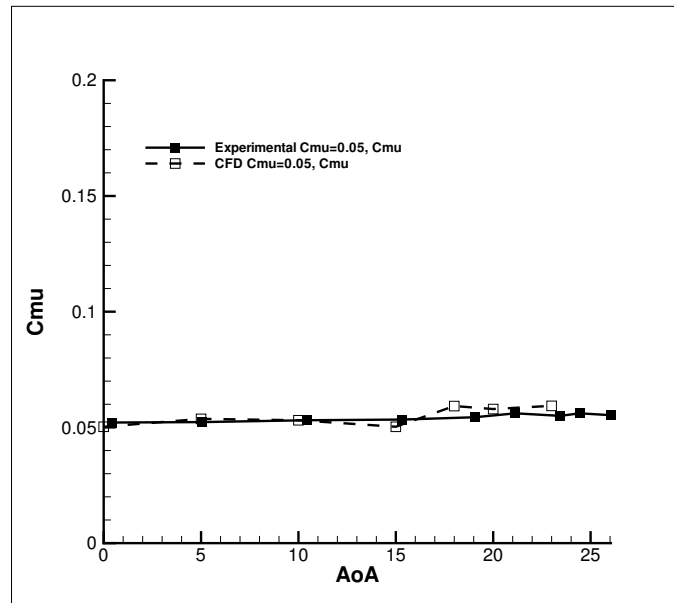


Figure 5.44: Numerical and Experimental Comparison of $C_\mu = 0.05$ Case, C_μ

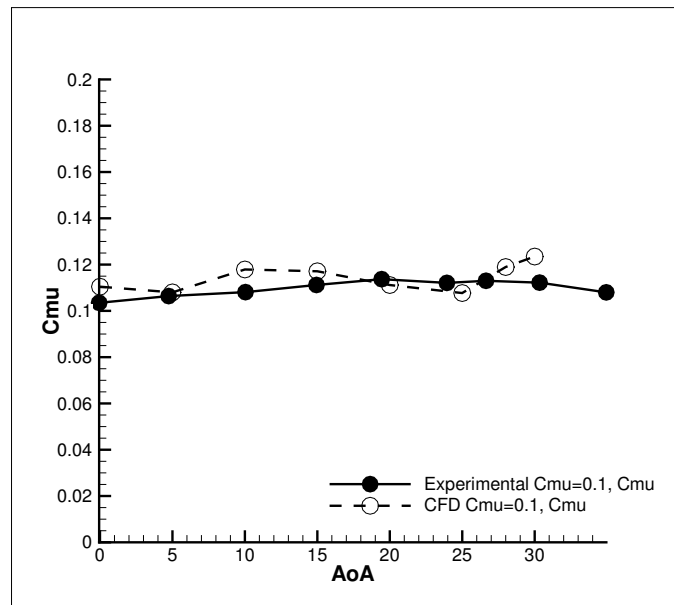


Figure 5.45: Numerical and Experimental Comparison of $C_\mu = 0.1$ Case, C_μ

Finally, the drag polar plots for the wind tunnel tests and the CFD simulations are shown in Fig. 5.46 and 5.47.

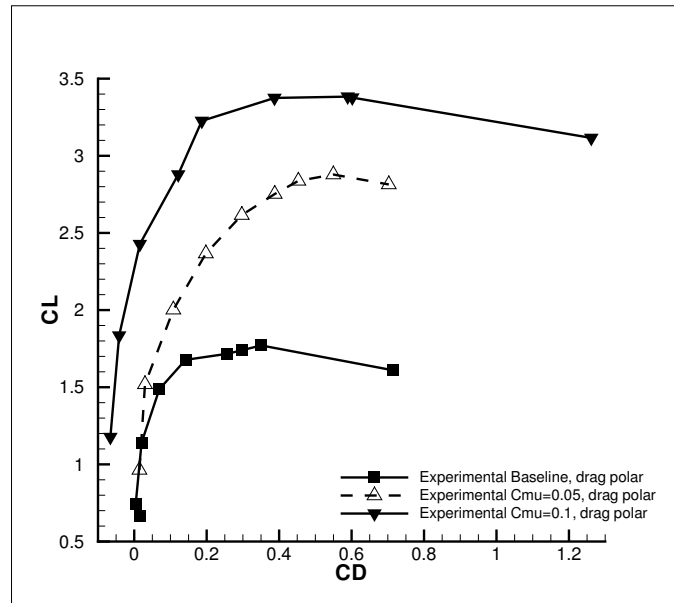


Figure 5.46: Experimental Drag Polar for All Cases

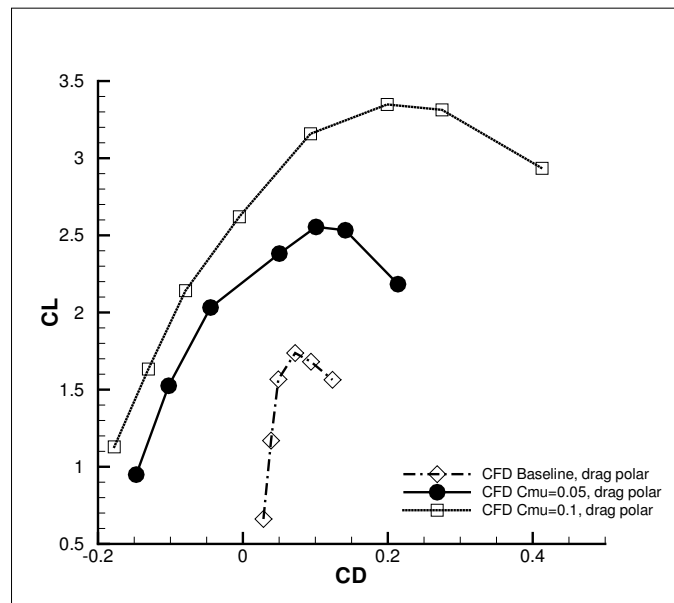


Figure 5.47: Numerical Drag Polar for All Cases

5.2.2 Future Work

Further validation of the CFJ flow control method should include testing with higher energy jets. By increasing the momentum coefficients beyond $C_\mu = 0.1$, even greater performance enhancements could be achieved. For the present research, co-flow jet benefits have only been observed for one injection and suction slot size. Future studies should include comparison of various slot sizes to optimize this flow control method. Also, uniformity of the jet during experimental testing should be verified with PIV (particle image velocimetry) analysis. This methodology will also provide streamline visualization of attached and separated flow. Currently, graduate students and faculty are continuing this work.

Chapter 6

Conclusions

This research thoroughly examined the performance enhancements of a thin co-flow jet airfoil with a 15% thickness to chord ratio. Wind tunnel testing and CFD simulations provided both experimental and numerical results. At high angles of attack the flow remains attached, even under the large pressure gradient, due to the enhancement of circulation with an outcome of augmented stall margin. Leading edge super suction and horizontal jet reactionary forces provide drag reduction for the CFJ airfoil. At low angles of attack, the drag becomes negative and thrust is produced. These benefits were observed through numerical analysis and experimental wind tunnel testing of a NACA 6415 baseline and a CFJ 6415-065-142 airfoil.

Use of the FASIP CFD code provided steady state simulations which demonstrated these improvements. A 92% increase in C_{Lmax} from the baseline airfoil, and a stall margin increase of 66% was achieved with a momentum coefficient of 0.1. Additionally, CFJ drag reduction was observed at all angles and thrust was produced from $\alpha = 0^\circ$ to $\alpha = 15^\circ$ for $C_\mu = 0.1$. These results were obtained using a 3rd order implicit E-CUSP vector splitting scheme and the Baldwin-Lomax turbulence model.

To acquire aerodynamic loading results, an adjustable slot size CFJ and a conventional baseline airfoil were designed and manufactured. Furthermore, the CFJ Wind

Tunnel Laboratory was constructed during the course of this research to supply the co-flow jet airfoil with proper air delivery and removal systems and measurement apparatus. Experimental results show a 91% increase in C_{Lmax} and a 14% augmentation in stall margin at $C_\mu = 0.1$. Drag was also reduced for this momentum coefficient and thrust generation occurred from $\alpha = 0^\circ$ to $\alpha = 5^\circ$.

This flow control method demonstrates dramatic flight improvements over a conventional cambered airfoil design. Implementation of this method into commercial or military aircraft could provide solutions to long standing problems. Fuel consumption and cost would drastically decrease due to drag reduction and thrust benefits. Increased lift and stall margin would multiply safety factors by orders of magnitude and allow for shorter take off and landing distances. From these performance enhancements, the co-flow jet flow control method has the potential to significantly increase flight efficiency and safety.

Appendix A

Coordinate Generation for Baseline and CFJ Airfoils

The following tables list the x and y coordinates of a NACA 6415 baseline and a CFJ 6415-065-142 airfoil.

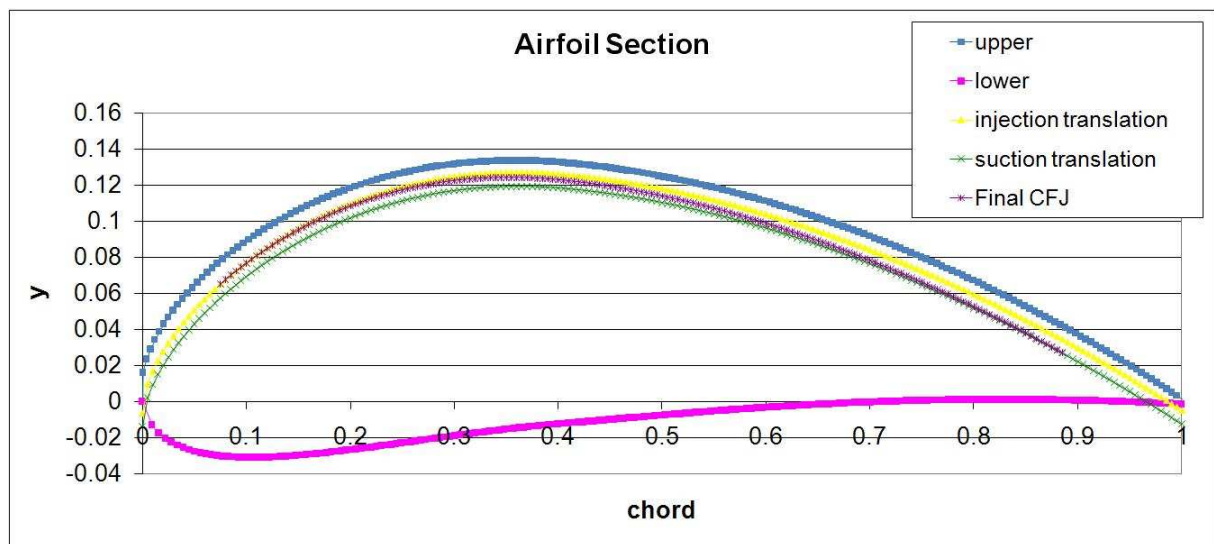
Coordinate Generation for Baseline NACA 6415 and CFJ 6415-065-142 Airfoils

m 0.06 **theta** -0.00934
p 0.4
t 0.15
c 1

					Baseline Coordinates				Y-coordinates for CFJ		
X	y _c	y _t	dy/dx	θ	x-upper	y-upper	x-lower	y-lower	Inj. translation	Suc. translation	Final CFJ
0	0	0	0.3	0.291457	0	0	0	0	-0.0065	-0.0142	
0.005	0.001490625	0.015266	0.29625	0.288013	0.000664	0.016128	0.009336	-0.01315	0.009628238	0.001928238	
0.01	0.0029625	0.021296	0.2925	0.284562	0.004021	0.023402	0.015979	-0.01748	0.016902404	0.009202404	
0.015	0.004415625	0.025796	0.28875	0.281104	0.007844	0.029199	0.022156	-0.02037	0.02269902	0.01499902	
0.02	0.00585	0.029497	0.285	0.277639	0.011915	0.034218	0.028085	-0.02252	0.027717624	0.020017624	
0.025	0.007265625	0.032684	0.28125	0.274167	0.016151	0.038729	0.033849	-0.0242	0.032228907	0.024528907	
0.03	0.0086625	0.035502	0.2775	0.270689	0.020507	0.042872	0.039493	-0.02555	0.036371576	0.028671576	
0.035	0.010040625	0.038037	0.27375	0.267204	0.024957	0.046728	0.045043	-0.02665	0.040227972	0.032527972	
0.04	0.0114	0.040347	0.27	0.263712	0.029483	0.050352	0.050517	-0.02755	0.043851715	0.036151715	
0.045	0.012740625	0.042469	0.26625	0.260213	0.034073	0.053378	0.055927	-0.0283	0.047280033	0.039580033	
0.05	0.0140625	0.044434	0.2625	0.256708	0.038718	0.05704	0.061282	-0.02892	0.050540026	0.042840026	
0.055	0.015365625	0.046262	0.25875	0.253197	0.043411	0.060152	0.066589	-0.02942	0.053652152	0.045952152	
0.06	0.01665	0.04797	0.255	0.249679	0.048147	0.063132	0.071853	-0.02983	0.056632307	0.048932307	
0.065	0.017915625	0.049572	0.25125	0.246155	0.052921	0.065993	0.077079	-0.03016	0.059493136	0.051793136	
0.07	0.0191625	0.051078	0.2475	0.242624	0.057728	0.068745	0.082272	-0.03042	0.0622449	0.0545449	
0.075	0.020390625	0.052499	0.24375	0.239088	0.062567	0.071396	0.087433	-0.03061	0.06489606	0.05719606	0.06489606
0.08	0.0216	0.05384	0.24	0.235545	0.067435	0.073954	0.092565	-0.03075	0.067453696	0.059753696	0.06740813
0.085	0.022790625	0.05511	0.23625	0.231996	0.072329	0.076424	0.097671	-0.03084	0.069923805	0.062223805	0.06983244
0.09	0.0239625	0.056312	0.2325	0.228441	0.077248	0.078812	0.102752	-0.03089	0.072311521	0.064611521	0.07217412
0.095	0.025115625	0.057452	0.22875	0.224881	0.082189	0.081121	0.107811	-0.03089	0.074621281	0.066921281	0.07443765
0.1	0.02625	0.058535	0.225	0.221314	0.087151	0.083357	0.112849	-0.03086	0.076856956	0.069156956	0.07662689
0.105	0.027365625	0.059563	0.22125	0.217742	0.092133	0.085522	0.117867	-0.03079	0.079021945	0.071321945	0.07874527
0.11	0.0284625	0.06054	0.2175	0.214164	0.097133	0.087619	0.122867	-0.03069	0.081119255	0.073419255	0.08079579
0.115	0.029540625	0.061469	0.21375	0.210581	0.102151	0.089652	0.127849	-0.03057	0.083151564	0.075451564	0.08278116
0.12	0.0306	0.062352	0.21	0.206992	0.107186	0.091621	0.132814	-0.03042	0.085121267	0.077421267	0.08470377
0.125	0.031640625	0.063193	0.20625	0.203398	0.112235	0.093351	0.137765	-0.03025	0.087030524	0.079330524	0.08656579
0.13	0.0326625	0.063992	0.2025	0.199798	0.117299	0.095381	0.142701	-0.03006	0.088881284	0.081181284	0.08836919
0.135	0.033665625	0.064752	0.19875	0.196193	0.122377	0.097175	0.147623	-0.02984	0.090675323	0.082975323	0.09011573
0.14	0.03465	0.065475	0.195	0.192583	0.127468	0.098914	0.152532	-0.02961	0.092414256	0.084714256	0.09180705
0.145	0.035615625	0.066162	0.19125	0.188968	0.132572	0.1006	0.157428	-0.02937	0.094099567	0.086399567	0.09344464
0.15	0.0365625	0.066815	0.1875	0.185348	0.137687	0.102233	0.162313	-0.02911	0.095732616	0.088032616	0.09502985
0.155	0.037490625	0.067434	0.18375	0.181723	0.142813	0.103815	0.167187	-0.02883	0.097314662	0.089614662	0.09656397
0.16	0.0384	0.068023	0.18	0.178093	0.14795	0.105347	0.17205	-0.02855	0.098846866	0.091146866	0.09804814
0.165	0.039290625	0.068581	0.17625	0.174458	0.153096	0.10683	0.176904	-0.02825	0.100330309	0.092630309	0.09948346
0.17	0.0401625	0.069109	0.1725	0.170819	0.158252	0.108266	0.181748	-0.02794	0.101765994	0.094065994	0.10087094
0.175	0.041015625	0.06961	0.16875	0.167175	0.163417	0.109655	0.186583	-0.02762	0.10315486	0.09545486	0.10221152
0.18	0.04185	0.070083	0.165	0.163527	0.168591	0.110998	0.191409	-0.0273	0.104497783	0.096797783	0.10350608
0.185	0.042665625	0.070529	0.16125	0.159874	0.173772	0.112296	0.196228	-0.02696	0.105795588	0.098095588	0.10475544
0.19	0.0434625	0.070951	0.1575	0.156217	0.178961	0.113549	0.201039	-0.02662	0.107049049	0.099349049	0.1059604
0.195	0.044240625	0.071347	0.15375	0.152555	0.184158	0.114759	0.205842	-0.02628	0.108258893	0.100558893	0.10712167
0.2	0.045	0.071719	0.15	0.14889	0.189361	0.115926	0.210639	-0.02593	0.10942581	0.10172581	0.10823995
0.205	0.045740625	0.072068	0.14625	0.14522	0.194571	0.11705	0.215429	-0.02557	0.110550452	0.102850452	0.1093159
0.21	0.0464625	0.072395	0.1425	0.141547	0.199787	0.118133	0.220213	-0.02521	0.111633435	0.103933435	0.11035013
0.215	0.047165625	0.0727	0.13875	0.13787	0.205009	0.119175	0.224991	-0.02484	0.112675347	0.104975347	0.11134324
0.22	0.04785	0.072983	0.135	0.134189	0.210236	0.120177	0.229764	-0.02448	0.113676744	0.105976744	0.11229578
0.225	0.048515625	0.073245	0.13125	0.130504	0.215468	0.121138	0.234532	-0.02411	0.114638158	0.106938158	0.1132083
0.23	0.0491625	0.073488	0.1275	0.126816	0.220706	0.12206	0.239294	-0.02374	0.115560096	0.107860096	0.11408129
0.235	0.049790625	0.07371	0.12375	0.123124	0.225947	0.122943	0.244053	-0.02336	0.116443043	0.108743043	0.11491526
0.24	0.0504	0.073914	0.12	0.119429	0.231194	0.123787	0.248806	-0.02299	0.117287463	0.109587463	0.11571065
0.245	0.050990625	0.074099	0.11625	0.115731	0.236444	0.124594	0.253556	-0.02261	0.118093799	0.110393799	0.11646793
0.25	0.0515625	0.074266	0.1125	0.112029	0.241698	0.125362	0.258302	-0.02224	0.11886248	0.11116248	0.11718752
0.255	0.052115625	0.074414	0.10875	0.108324	0.246955	0.126094	0.263045	-0.02186	0.119593915	0.111893915	0.11786984
0.26	0.05265	0.074546	0.105	0.104617	0.252215	0.126788	0.267785	-0.02149	0.120288498	0.112588498	0.11851527
0.265	0.053165625	0.074661	0.10125	0.100906	0.257479	0.127447	0.272521	-0.02112	0.12094661	0.11324661	0.1191242
0.27	0.0536625	0.074759	0.0975	0.097193	0.262745	0.128069	0.277255	-0.02074	0.121568617	0.113868617	0.11969701
0.275	0.054140625	0.074841	0.09375	0.093477	0.268014	0.128655	0.281986	-0.02037	0.122154873	0.114454873	0.12023404
0.28	0.0546	0.074907	0.09	0.089758	0.273285	0.129206	0.286715	-0.02001	0.122705719	0.115005719	0.12073565
0.285	0.055040625	0.074958	0.08625	0.086037	0.278559	0.129721	0.291441	-0.01964	0.123221487	0.115521487	0.12120215
0.29	0.0554625	0.074994	0.0825	0.082314	0.283834	0.130202	0.296166	-0.01928	0.123702496	0.116002496	0.12163388
0.295	0.055865625	0.075015	0.07875	0.078588	0.289111	0.130649	0.300889	-0.01892	0.124149057	0.116449057	0.12203115
0.3	0.05625	0.075022	0.075	0.07486	0.294389	0.131061	0.305611	-0.01856	0.124561471	0.116861471	0.12239426

X	y _c	y _t	dy _c /dx	θ	Baseline Coordinates				Y-coordinates for CFJ		
					x-upper	y-upper	x-lower	y-lower	Inj. translation	Suc. translation	Final CFJ
0.305	0.056615625	0.075014	0.07125	0.07113	0.299669	0.13144	0.310331	-0.01821	0.12494003	0.11724003	0.12272351
0.31	0.0569625	0.074993	0.0675	0.067398	0.304949	0.131785	0.315051	-0.01786	0.125285017	0.117585017	0.12301917
0.315	0.057290625	0.074958	0.06375	0.063664	0.310231	0.132097	0.319769	-0.01752	0.12559671	0.11789671	0.12328153
0.32	0.0576	0.07491	0.06	0.059928	0.315513	0.132375	0.324487	-0.01718	0.125875376	0.118175376	0.12351086
0.325	0.057890625	0.074849	0.05625	0.056191	0.320796	0.132621	0.329204	-0.01684	0.126121276	0.118421276	0.12370743
0.33	0.0581625	0.074775	0.0525	0.052452	0.32608	0.132835	0.33392	-0.01651	0.126334666	0.118634666	0.12387147
0.335	0.058415625	0.074689	0.04875	0.048711	0.331363	0.133016	0.338637	-0.01618	0.126515795	0.118815795	0.12400326
0.34	0.05865	0.07459	0.045	0.04497	0.336647	0.133165	0.343353	-0.01586	0.126664903	0.118964903	0.12410303
0.345	0.058865625	0.07448	0.04125	0.041227	0.34193	0.133282	0.34807	-0.01555	0.126782228	0.119082228	0.12417101
0.35	0.0590625	0.074358	0.0375	0.037482	0.347214	0.133368	0.352786	-0.01524	0.126868	0.119168	0.12420745
0.355	0.059240625	0.074224	0.03375	0.033737	0.352496	0.133422	0.357504	-0.01494	0.126922446	0.119222446	0.12421257
0.36	0.0594	0.074079	0.03	0.029991	0.357779	0.133446	0.362221	-0.01465	0.126945785	0.119245785	0.12418658
0.365	0.059540625	0.073923	0.02625	0.026244	0.36306	0.133438	0.36694	-0.01436	0.126938234	0.119238234	0.12412972
0.37	0.0596625	0.073756	0.0225	0.022496	0.368341	0.1334	0.371659	-0.01408	0.126900003	0.119200003	0.12404218
0.375	0.059765625	0.073579	0.01875	0.018748	0.373621	0.133331	0.376379	-0.0138	0.1268313	0.1191313	0.12392418
0.38	0.05985	0.073391	0.015	0.014999	0.378899	0.133232	0.381101	-0.01353	0.126732326	0.119032326	0.12377592
0.385	0.059915625	0.073192	0.01125	0.01125	0.384177	0.133103	0.385823	-0.01327	0.126603281	0.118903281	0.1235976
0.39	0.0599625	0.072984	0.0075	0.0075	0.389453	0.132944	0.390547	-0.01302	0.126444357	0.118744357	0.12338942
0.395	0.059990625	0.072766	0.00375	0.00375	0.394727	0.132756	0.395273	-0.01277	0.126255747	0.118555747	0.12315157
0.4	0.06	0.072538	0	0	0.4	0.132538	0.4	-0.01254	0.126037636	0.118337636	0.12288424
0.405	0.059995833	0.0723	-0.00167	-0.00167	0.40512	0.132296	0.40488	-0.0123	0.125795824	0.118095824	0.12259462
0.41	0.059983333	0.072053	-0.00333	-0.00333	0.41024	0.132036	0.40976	-0.01207	0.125536102	0.117836102	0.12228711
0.415	0.0599625	0.071797	-0.005	-0.005	0.415359	0.131759	0.414641	-0.01183	0.125258637	0.117558637	0.12196186
0.42	0.059933333	0.071532	-0.00667	-0.00667	0.420477	0.131464	0.419523	-0.0116	0.124963593	0.117263593	0.12161904
0.425	0.059895833	0.071258	-0.00833	-0.00833	0.425594	0.131151	0.424406	-0.01136	0.124651129	0.116951129	0.12125881
0.43	0.05985	0.070975	-0.01	-0.01	0.43071	0.130821	0.42929	-0.01112	0.124321402	0.116621402	0.12088133
0.435	0.059795833	0.070684	-0.01167	-0.01167	0.435825	0.130475	0.434175	-0.01088	0.123974563	0.116274563	0.12048675
0.44	0.059733333	0.070384	-0.01333	-0.01333	0.440938	0.130111	0.439062	-0.01064	0.123610763	0.115910763	0.12007521
0.445	0.0596625	0.070076	-0.015	-0.015	0.446051	0.12973	0.443949	-0.01041	0.123230146	0.115530146	0.11964687
0.45	0.059583333	0.069759	-0.01667	-0.01667	0.451162	0.129333	0.448838	-0.01017	0.122832855	0.115132855	0.11920187
0.455	0.059495833	0.069435	-0.01833	-0.01833	0.456273	0.128919	0.453727	-0.00993	0.122419028	0.114719028	0.11874035
0.46	0.0594	0.069103	-0.02	-0.02	0.461382	0.128489	0.458618	-0.00969	0.121988802	0.114288802	0.11826243
0.465	0.059295833	0.068763	-0.02167	-0.02166	0.46649	0.128042	0.46351	-0.00945	0.121542308	0.113842308	0.11776827
0.47	0.059183333	0.068415	-0.02333	-0.02333	0.471596	0.12758	0.468404	-0.00921	0.121079678	0.113379678	0.11725798
0.475	0.0590625	0.06806	-0.025	-0.02499	0.476701	0.127101	0.473299	-0.00898	0.120601037	0.112901037	0.11673169
0.48	0.058933333	0.067697	-0.02667	-0.02666	0.481805	0.126607	0.478195	-0.00874	0.120106509	0.112406509	0.11618953
0.485	0.058795833	0.067327	-0.02833	-0.02833	0.486907	0.126096	0.483093	-0.0085	0.119596216	0.111896216	0.11563161
0.49	0.05865	0.06695	-0.03	-0.02999	0.492008	0.12557	0.487992	-0.00827	0.119070276	0.111370276	0.11505807
0.495	0.058495833	0.066566	-0.03167	-0.03166	0.497107	0.125029	0.492893	-0.00804	0.118528805	0.110828805	0.11446901
0.5	0.058333333	0.066175	-0.03333	-0.03332	0.502205	0.124472	0.497795	-0.00781	0.117971915	0.110271915	0.11386454
0.505	0.0581625	0.065777	-0.035	-0.03499	0.507301	0.1239	0.502699	-0.00757	0.117399717	0.109699717	0.11324479
0.51	0.057983333	0.065373	-0.03667	-0.03665	0.512395	0.123312	0.507605	-0.00735	0.11681232	0.10911232	0.11260984
0.515	0.057795833	0.064962	-0.03833	-0.03831	0.517488	0.12271	0.512512	-0.00712	0.116209829	0.108509829	0.11195982
0.52	0.0576	0.064544	-0.04	-0.03998	0.52258	0.122092	0.51742	-0.00689	0.115592346	0.107892346	0.11129483
0.525	0.057395833	0.06412	-0.04167	-0.04164	0.527669	0.12146	0.522331	-0.00667	0.114959973	0.107259973	0.11061496
0.53	0.057183333	0.063689	-0.04333	-0.04331	0.532757	0.120813	0.527243	-0.00645	0.114312807	0.106612807	0.10992031
0.535	0.0569625	0.063252	-0.045	-0.04497	0.537843	0.120151	0.532157	-0.00623	0.113650945	0.105950945	0.10921099
0.54	0.056733333	0.062809	-0.04667	-0.04663	0.542928	0.119474	0.537072	-0.00601	0.112974481	0.105274481	0.10848708
0.545	0.056495833	0.06236	-0.04833	-0.0483	0.548011	0.118784	0.541989	-0.00579	0.112283506	0.104583506	0.10774867
0.55	0.05625	0.061905	-0.05	-0.04996	0.553091	0.118078	0.546909	-0.00558	0.111578109	0.103878109	0.10699587
0.555	0.055995833	0.061444	-0.05167	-0.05162	0.55817	0.117358	0.55183	-0.00537	0.110858378	0.103158378	0.10622874
0.56	0.055733333	0.060978	-0.05333	-0.05328	0.563248	0.116624	0.556752	-0.00516	0.110124397	0.102424397	0.10544739
0.565	0.0554625	0.060505	-0.055	-0.05494	0.568323	0.115876	0.561677	-0.00495	0.109376251	0.101676251	0.10465188
0.57	0.055183333	0.060027	-0.05667	-0.05661	0.573396	0.115114	0.566604	-0.00475	0.108614018	0.100914018	0.10384231
0.575	0.054895833	0.059543	-0.05833	-0.05827	0.578467	0.114338	0.571533	-0.00455	0.107837779	0.100137779	0.10301876
0.58	0.0546	0.059054	-0.06	-0.05993	0.583537	0.113548	0.576463	-0.00435	0.107047611	0.099347611	0.10218129
0.585	0.054295833	0.058559	-0.06167	-0.06159	0.588604	0.112744	0.581396	-0.00415	0.106243587	0.098543587	0.10132998
0.59	0.053983333	0.058059	-0.06333	-0.06325	0.59367	0.111926	0.58633	-0.00396	0.105425782	0.097725782	0.10046491
0.595	0.0536625	0.057553	-0.065	-0.06491	0.598733	0.111094	0.591267	-0.00377	0.104594266	0.096894266	0.09958615
0.6	0.053333333	0.057042	-0.06667	-0.06657	0.603794	0.110249	0.596206	-0.00358	0.103749107	0.096049107	0.09869377
0.605	0.052995833	0.056526	-0.06833	-0.06823	0.608854	0.10939	0.601146	-0.0034	0.102890374	0.095190374	0.09778784
0.61	0.05265	0.056005	-0.07	-0.06989	0.613911	0.108518	0.606089	-0.00322	0.102018132	0.094318132	0.09686841
0.615	0.052295833	0.055479	-0.07167	-0.07154	0.618966	0.107632	0.611034	-0.00304	0.101132444	0.093432444	0.09593556
0.62	0.051933333	0.054947	-0.07333	-0.0732	0.624019	0.106733	0.615981	-0.00287	0.100233372	0.092533372	0.09498935
0.625	0.0515625	0.054411	-0.075	-0.07486	0.629069	0.105821	0.620931	-0.0027	0.099320976	0.091620976	0.09402983
0.63	0.051183333	0.05387	-0.07667	-0.07652	0.634118	0.104895	0.625882	-0.00253	0.098395313	0.090695313	0.09305707
0.635	0.050795833	0.053323	-0.07833	-0.07817	0.639164	0.103956	0.630836	-0.00236	0.097456441	0.089756441	0.09207112
0.64	0.0504	0.052772	-0.08	-0.07983	0.644208	0.103004	0.635792	-0.0022	0.096504413	0.088804413	0.09107204
0.645	0.049995833	0.052217	-0.08167	-0.08149	0.64925	0.102039	0.64075	-0.00205	0.095539283	0.087839283	0.09005987
0.65	0.049583333	0.051656	-0.08333	-0.08314	0.65429	0.101061	0.64571	-0.00189	0.094561102	0.086861102	0.08903467

X	y _c	y _t	dy _c /dx	θ	Baseline Coordinates				Y-coordinates for CFJ		
					x-upper	y-upper	x-lower	y-lower	Inj. translation	Suc. translation	Final CFJ
0.655	0.0491625	0.051091	-0.085	-0.0848	0.659327	0.10007	0.650673	-0.00174	0.093569919	0.085869919	0.0879965
0.66	0.048733333	0.050521	-0.08667	-0.08645	0.664362	0.099066	0.655638	-0.0016	0.092565783	0.084865783	0.08694539
0.665	0.048295833	0.049947	-0.08833	-0.0881	0.669395	0.098049	0.660605	-0.00146	0.091548738	0.083848738	0.0858814
0.67	0.04785	0.049368	-0.09	-0.08976	0.674425	0.097019	0.665575	-0.00132	0.090518831	0.082818831	0.08480457
0.675	0.047395833	0.048784	-0.09167	-0.09141	0.679453	0.095976	0.670547	-0.00118	0.089476102	0.081776102	0.08371494
0.68	0.046933333	0.048196	-0.09333	-0.09306	0.684479	0.094921	0.675521	-0.00105	0.088420595	0.080720595	0.08261255
0.685	0.0464625	0.047603	-0.095	-0.09472	0.689502	0.093852	0.680498	-0.00093	0.087352348	0.079652348	0.08149745
0.69	0.045983333	0.047006	-0.09667	-0.09637	0.694523	0.092771	0.685477	-0.0008	0.0862714	0.0785714	0.08036966
0.695	0.045495833	0.046405	-0.09833	-0.09802	0.699541	0.091678	0.690459	-0.00069	0.085177787	0.077477787	0.07922924
0.7	0.045	0.045799	-0.1	-0.09967	0.704557	0.090572	0.695443	-0.00057	0.084071543	0.076371543	0.07807621
0.705	0.044495833	0.045189	-0.10167	-0.10132	0.709571	0.089453	0.700429	-0.00046	0.082952703	0.075252703	0.0769106
0.71	0.043983333	0.044574	-0.10333	-0.10297	0.714582	0.088321	0.705418	-0.00035	0.081821297	0.074121297	0.07573246
0.715	0.0434625	0.043955	-0.105	-0.10462	0.71959	0.087177	0.71041	-0.00025	0.080677357	0.072977357	0.0745418
0.72	0.042933333	0.043332	-0.10667	-0.10626	0.724596	0.086021	0.715404	-0.00015	0.079520911	0.071820911	0.07333866
0.725	0.042395833	0.042705	-0.10833	-0.10791	0.729599	0.084852	0.720401	-6E-05	0.078351986	0.070651986	0.07212307
0.73	0.04185	0.042073	-0.11	-0.10956	0.7346	0.083671	0.7254	2.94E-05	0.077170608	0.069470608	0.07089505
0.735	0.041295833	0.041437	-0.11167	-0.11121	0.739599	0.082477	0.730401	0.000115	0.075976802	0.068276802	0.06965462
0.74	0.040733333	0.040797	-0.11333	-0.11285	0.744594	0.081271	0.735406	0.000196	0.074770589	0.067070589	0.06840182
0.745	0.0401625	0.040152	-0.115	-0.1145	0.749587	0.080052	0.740413	0.000273	0.073551992	0.065851992	0.06713665
0.75	0.039583333	0.039504	-0.11667	-0.11614	0.754578	0.078821	0.745422	0.000346	0.072321029	0.064621029	0.06585915
0.755	0.038995833	0.038851	-0.11833	-0.11779	0.759566	0.077578	0.750434	0.000414	0.071077721	0.063377721	0.06456932
0.76	0.0384	0.038194	-0.12	-0.11943	0.764551	0.076322	0.755449	0.000478	0.069822083	0.062122083	0.06326719
0.765	0.037795833	0.037533	-0.12167	-0.12107	0.769533	0.075054	0.760467	0.000538	0.06855413	0.06085413	0.06195277
0.77	0.037183333	0.036868	-0.12333	-0.12271	0.774513	0.073774	0.765487	0.000593	0.067273878	0.059573878	0.06062607
0.775	0.0365625	0.036198	-0.125	-0.12435	0.77949	0.072481	0.77051	0.000644	0.065981339	0.058281339	0.05928712
0.78	0.035933333	0.035525	-0.12667	-0.126	0.784464	0.071177	0.775536	0.00069	0.064676524	0.056976524	0.05793591
0.785	0.035295833	0.034847	-0.12833	-0.12764	0.789436	0.069859	0.780564	0.000732	0.063359442	0.055659442	0.05657247
0.79	0.03465	0.034165	-0.13	-0.12928	0.794404	0.06853	0.785596	0.00077	0.062030103	0.054330103	0.05519679
0.795	0.033995833	0.033479	-0.13167	-0.13091	0.79937	0.067189	0.79063	0.000803	0.060688514	0.052988514	0.05380889
0.8	0.033333333	0.032789	-0.13333	-0.13255	0.804334	0.065835	0.795666	0.000832	0.05933468	0.05163468	0.05240877
0.805	0.0326625	0.032095	-0.135	-0.13419	0.809294	0.064469	0.800706	0.000856	0.057968606	0.050268606	0.05099644
0.81	0.031983333	0.031396	-0.13667	-0.13583	0.814251	0.06309	0.805749	0.000876	0.056590294	0.048890294	0.0495719
0.815	0.031295833	0.030693	-0.13833	-0.13746	0.819206	0.0617	0.810794	0.000892	0.055199746	0.047499746	0.04813515
0.82	0.0306	0.029987	-0.14	-0.1391	0.824158	0.060297	0.815842	0.000903	0.053796963	0.046096963	0.04668619
0.825	0.029895833	0.029276	-0.14167	-0.14073	0.829106	0.058882	0.820894	0.00091	0.052381944	0.044681944	0.04522503
0.83	0.029183333	0.02856	-0.14333	-0.14236	0.834052	0.057455	0.825948	0.000912	0.050954686	0.043254686	0.04375165
0.835	0.0284625	0.027841	-0.145	-0.144	0.838995	0.056015	0.831005	0.00091	0.049515186	0.041815186	0.04226606
0.84	0.027733333	0.027117	-0.14667	-0.14563	0.843935	0.054563	0.836065	0.000903	0.048063438	0.040363438	0.04076825
0.845	0.026995833	0.026389	-0.14833	-0.14726	0.848872	0.053099	0.841128	0.000892	0.046599436	0.038899436	0.03925821
0.85	0.02625	0.025657	-0.15	-0.14889	0.853806	0.051623	0.846194	0.000877	0.045123173	0.037423173	0.03773594
0.855	0.025495833	0.024921	-0.15167	-0.15052	0.858737	0.050135	0.851263	0.000857	0.04363464	0.03593464	0.03620143
0.86	0.024733333	0.02418	-0.15333	-0.15215	0.863665	0.048634	0.856335	0.000833	0.042133826	0.034433826	0.03465467
0.865	0.0239625	0.023435	-0.155	-0.15378	0.86859	0.047121	0.86141	0.000804	0.040620721	0.032920721	0.03309565
0.87	0.023183333	0.022685	-0.15667	-0.1554	0.873511	0.045595	0.866489	0.000771	0.039095311	0.031395311	0.03152435
0.875	0.022395833	0.021932	-0.15833	-0.15703	0.87843	0.044058	0.87157	0.000734	0.037557582	0.029857582	0.02994076
0.88	0.0216	0.021173	-0.16	-0.15866	0.883345	0.042508	0.876655	0.000692	0.036007519	0.028307519	0.02834487
0.885	0.020795833	0.020411	-0.16167	-0.16028	0.888257	0.040945	0.881743	0.000647	0.034445105	0.026745105	0.0267367
0.89	0.019983333	0.019644	-0.16333	-0.1619	0.893167	0.03937	0.886833	0.000596	0.032870323	0.025170323	
0.895	0.0191625	0.018872	-0.165	-0.16353	0.898072	0.037783	0.891928	0.000542	0.031283154	0.023583154	
0.9	0.018333333	0.018096	-0.16667	-0.16515	0.902975	0.036184	0.897025	0.000483	0.029683577	0.021983577	
0.905	0.017495833	0.017316	-0.16833	-0.16677	0.907874	0.034572	0.902126	0.00042	0.028071571	0.020371571	
0.91	0.01665	0.016531	-0.17	-0.16839	0.912771	0.032947	0.907229	0.000353	0.026447113	0.018747113	
0.915	0.015795833	0.015741	-0.17167	-0.17001	0.917663	0.03131	0.912337	0.000281	0.024810179	0.017110179	
0.92	0.014933333	0.014947	-0.17333	-0.17163	0.922553	0.029661	0.917447	0.000206	0.023160744	0.015460744	
0.925	0.0140625	0.014148	-0.175	-0.17325	0.927439	0.027999	0.922561	0.000126	0.021498781	0.013798781	
0.93	0.013183333	0.013344	-0.17667	-0.17486	0.932322	0.026324	0.927678	4.24E-05	0.019824263	0.012124263	
0.935	0.012295833	0.012536	-0.17833	-0.17648	0.937201	0.024637	0.932799	-4.5E-05	0.018137161	0.010437161	
0.94	0.0114	0.011723	-0.18	-0.17809	0.942077	0.022937	0.937923	-0.00014	0.016437445	0.008737445	
0.945	0.010495833	0.010905	-0.18167	-0.17971	0.946949	0.021225	0.943051	-0.00023	0.014725083	0.007025083	
0.95	0.009583333	0.010082	-0.18333	-0.18132	0.951818	0.0195	0.948182	-0.00033	0.013000044	0.005300044	
0.955	0.0086625	0.009254	-0.185	-0.18293	0.956683	0.017762	0.953317	-0.00044	0.011262294	0.003562294	
0.96	0.007733333	0.008421	-0.18667	-0.18454	0.961545	0.016012	0.958455	-0.00055	0.009511797	0.001811797	
0.965	0.006795833	0.007584	-0.18833	-0.18615	0.966404	0.014249	0.963596	-0.00066	0.007748519	4.85188E-05	
0.97	0.00585	0.006741	-0.19	-0.18776	0.971258	0.012472	0.968742	-0.00077	0.005972421	-0.001727579	
0.975	0.004895833	0.005893	-0.19167	-0.18937	0.976109	0.010683	0.973891	-0.00089	0.004183467	-0.003516533	
0.98	0.003933333	0.00504	-0.19333	-0.19098	0.980957	0.008882	0.979043	-0.00101	0.002381615	-0.005318385	
0.985	0.0029625	0.004182	-0.195	-0.19258	0.9858	0.007067	0.9842	-0.00114	0.000566827	-0.007133173	
0.99	0.001983333	0.003318	-0.19667	-0.19419	0.99064	0.005239	0.98936	-0.00127	-0.001260941	-0.008960941	
0.995	0.000995833	0.002449	-0.19833	-0.19579	0.995476	0.003398	0.994524	-0.00141	-0.00310173	-0.01080173	
1	0	0.001575	-0.2	-0.1974	1.000309	0.001544	0.999691	-0.00154	-0.004955585	-0.012655585	



Appendix B

Sample Input Files for FASIP code

B.1 *datain* File

```
&consts
delta      = 0.0d+00, 0.0d+00, 0.0d+00, 0.0d+00, 0.0d+00,! Entropy cut-off
                                     ! for rho, rhou, rhov, rhow and rhoe respectively
epsfactor  = 1.00d-06, ! epsilon used in linear reconstruction
gamma      = 1.40d+00, ! Ratio of specific heats
prandtl    = 0.72d0,   ! Molecular Prandtl number
prt         = .9d0,    ! turbulent prandtl number
suther     = T,        ! = T: Sutherlands Law. = F: mu = T
tref       = 0.368006d0, ! Non-dimensional ref temperature in Sutherland

flows
blen        = 3,        ! the number of halo layers for block boundaries.
                                     ! =2, under 3rd scheme;
                                     ! =3, 5th scheme;
                                     ! =4, 7th scheme
idimen      = 3,        ! = 1: 1-D, = 2: 2-D, = 3: 3-D
nl          = 5,        ! No. of eqs. =5, Laminar or BL model;
                                     ! =6, SA model or DES
angl1       = 0.0d0,    ! inlet angle 1
angl2       = 0.d0,     ! inlet angle 2
inviscid    = F,        ! = T: inviscid; = F: viscous
machinf     = 0.1d0,    ! Mach no. based on U_infinity and a_infinity
```

```

poutlet      = 68.9286 ! outlet static pressure
ptotal       = 69.4287, ! Total pressure at inlet
reynolds     = 674960.68d0, ! Reynolds number
tintvl       = .05, ! unsteady time interval
ttotal       = 1.000, ! Total temperature at inlet
turb         = 1 ! =0, Laminar flow or LES
               ! =1 (nl=5), BL turbulence model;
               ! =1 (nl=6), SA turbulence model or DES

/
&comp
choice       = 'y', ! ='y': from rstore. ='n': from initial value
cfl          = 1.00d0, ! CFL number
checksteps   = 1, ! print out status every # steps for monitoring
dual_t       = 0, ! 1: unsteady, 0: steady
eps          = 1.d-12, ! residual limit
gcl          = 0, ! geometry conservation in moving grid
               ! =0, disabled; =1, enabled
integrate    = 4, ! =1, AF; =2, R-K; 3, Euler;
               ! =4, GS; =5, LU-SGS; =6, LU-GSLR
intersteps   = 50, ! save results every # steps in computation
iter_gs      = 2, ! number of Gauss-Seidel sweeps
kfactor      = 0.33333d0, ! factor in linear reconstruction
lhs_order    = 0, ! =0, 1st order MUSCL for LHS matrices;
               ! =1, 2nd or 3rd order.
lhs_scheme   = 4, ! =1, Roe; =2, Zha;=3, none, =4, Van Leer
(when RHS is not Roe scheme)
limiter      = 1, ! =0, no limiter; =1, MINMOD ; =2, SUPERBEE;
=3, A-T-VL
moving       = 0, ! moving grid, 0-stationary, 1-fixed, 2-induced
nrbc_ex      = 0, ! =0: no NRBC at exit;
               ! =3: use Euler Method non-reflective BC(NRBC)
               at exit
nstep        = 10000, ! No. of time steps
rhs_order    = 1, ! =0, 1st order MUSCL (blen>=2);
               ! =1, 2nd or 3rd order (blen>=2);
               ! =4, 3rd-WENO (blen>=2);
               ! =5, 5th order fixed stencil (blen=>3);
               ! =6, 5th-WENO (blen=>3);
               ! =7, 7th order fixed stencil (blen=>4);
               ! =8, 7th-WENO (blen=>4)
rhs_scheme   = 3, ! =1,Roe; 2,Zha2; 3,Zha3; 4, Van Leer;
               ! 5,Edwards; 6,Zha6; 7,AUSM+; 8:Zha;
               ! 9:AUSMV; 10: AUSMD; 11: VAN LEER-HANEL
strtp        = 0, ! 0-no structure; 1-cylinder; 2-airfoil
tsteps       = 20, ! unsteady time marching stes using dual-

```

```

time stepping
unidt      = 0,          ! >0, Uniform time interval in whole domain
                        ! =0, Local time step
vis_order  = 1,          ! The order of the viscous term.
                        !   =1, 2nd order(blen=2);
                        !   =3, 4th order(blen=3);
                        !   =5, 6th order(blen=4)
velinit    = 1.d0,       ! dimensionless velocity initial value
strm_dir   = 1,          ! main flow direction
theta      = 0.d0,       ! initial velocity angle
twpar      = 2,          ! 1<=twpar<=10, initial for omega when nl=7
tkpar      = 5           ! 2<=tkpar<=5, initial for k when nl=7
varepsilon  = 1e-2,       ! for WENO scheme
wall_order = 1,          ! 1----1st order; 3----3rd order
rotide     = 0,          ! =0, no rotating
                        ! =1, rotating
/

&coef1eq
ides       = 0,          ! =0, 1EQ; =1, DES
cdes       = 0.65d0,     ! parameter used in DES
iblnu      = 1,          ! block number in which trip is placed
ipt        = 1,          ! index of trip point in i-direction
jpt        = 1,          ! index of trip point in j-direction
kpt        = 1,          ! index of trip point in k-direction
ic1        = 1,          ! ic1, ic2 and ic3 represent the i, j, k grid
ic2        = 0,          ! spacing along the wall at the trip.
ic3        = 0,          ! =0, no the direction; =1, along the direction
tko        = 0.66666667d0, ! constant used in SA 1EQ turbulence model
cb1        = 0.1355d0,    ! constant used in SA 1EQ turbulence model
cb2        = 0.622d0,     ! constant used in SA 1EQ turbulence model
cap_k      = 0.41d0,      ! constant used in SA 1EQ turbulence model
cw2        = 0.3d0,       ! constant used in SA 1EQ turbulence model
cw3        = 2.d0,        ! constant used in SA 1EQ turbulence model
cv1        = 7.1d0,       ! constant used in SA 1EQ turbulence model
ct1        = 0.0d0,       ! constant used in SA 1EQ turbulence model
ct2        = 0.0d0,       ! constant used in SA 1EQ turbulence model
ct3        = 0.0d0,       ! constant used in SA 1EQ turbulence model
ct4        = 0.0d0 /      ! constant used in SA 1EQ turbulence model

&mvgrid2
lref       = 1.d0,        ! reference length
aref       = 1.d0,        ! reference area
xctr       = 0.d0,        ! x-coordinate of central point in grid re-
                        construction

```

```

yctr      = 0.d0,          ! y-coordinate of central point in grid re-
      construction
xref      = -1.0d0,        ! x-coordinate of reference point
yref      = 0.d0,          ! y-coordinate of reference point
jfx       = 76,            ! index for grid re-construction (when j>jfx)
beta      = 1.05d0 /       ! grid ratio used in grid re-construction

&strct_cyl
cs         = 0.1583d0, ! parameters for induced vibration of cylinder
mus        = 12.732395d0, ! parameters for induced vibration of
cylinder
ub         = 1.5915494d0 ! parameters for induced vibration of
cylinder
/

&strct_af
kc         = 0.06663197154765449d0, ! parameter for induced vibration of airfoil
nfp        = 629, ! parameter for induced vibration of airfoil
walf       = 41.5054817741115d0, ! parameter for induced vibration of airfoil
uinf       = 311.453201894433d0 ! parameter for induced vibration of airfoil
/

&rotor
rotalp     = 10.d0,          ! angle between the rotating periodic boundary faces
ronum      = 0.195256d0,    ! rossby number = 0 no frame rotating (0.895256d0)
xrst       = -0.0264d0      ! starting index for moving part on hub
xred       = 0.4521d0       ! ending index for moving part on hub
/

&strct_wng
kc         = 0.774401182147045d0, ! parameter for wing
ust        = 2.419402425548856E-002, ! parameter for wing
omega      = 0.195181305d0,          ! parameter for wing
nfp        = 322,                    ! parameter for wing
nmode      = 5                       ! parameter for wing
/

&source_g
rayleigh   = 1.0e3,      ! rayleigh number
froude     = 1.0d0,      ! froude number
epsilon    = 0.6,        ! parameter  $(T_h - T_c)/(T_h + T_c)$ 
/

&bcdef bcdir='xie',block=1,bctype=7,start=1,1,1,end=1,40,59,
      iblock=6,istart=27,1,1,iend=27,40,59,order=1,2,3/

```

```

&bcdef bcdire='xie',block=1,bctype=7,start=27,1,1,end=27,40,59,
        iblock=2,istart=1,1,1,iend=1,40,59,order=1,2,3/
&bcdef bcdire='eta',block=1,bctype=7,start=1,1,1,end=27,1,59,
        iblock=10,istart=1,39,1,iend=27,39,59,order=1,2,3/
&bcdef bcdire='eta',block=1,bctype=6,start=1,40,1,end=27,40,59/
&bcdef bcdire='zta',block=1,bctype=3,start=1,1,1,end=27,40,1/
&bcdef bcdire='zta',block=1,bctype=3,start=1,1,59,end=27,40,59/

&bcdef bcdire='eta',block=10,bctype=3,start=1,1,1,end=27,1,59/
&bcdef bcdire='xie',block=10,bctype=7,start=1,1,1,end=1,39,59,
        iblock=15,istart=27,1,1,iend=27,39,59,order=1,2,3/
&bcdef bcdire='xie',block=10,bctype=7,start=27,1,1,end=27,39,59,
        iblock=11,istart=1,1,1,iend=1,39,59,order=1,2,3/
&bcdef bcdire='zta',block=10,bctype=3,start=1,1,1,end=27,39,1/
&bcdef bcdire='zta',block=10,bctype=3,start=1,1,59,end=27,39,59/

&bcdef bcdire='xie',block=2,bctype=7,start=54,1,1,end=54,40,59,
        iblock=3,istart=1,1,1,iend=1,40,59,order=1,2,3/
&bcdef bcdire='eta',block=2,bctype=7,start=1,1,1,end=54,1,59,
        iblock=11,istart=1,39,1,iend=54,39,59,order=1,2,3/
&bcdef bcdire='eta',block=2,bctype=6,start=1,40,1,end=21,40,59/
&bcdef bcdire='eta',block=2,bctype=11,start=22,40,1,end=54,40,59/
&bcdef bcdire='zta',block=2,bctype=3,start=1,1,1,end=54,40,1/
&bcdef bcdire='zta',block=2,bctype=3,start=1,1,59,end=54,40,59/

&bcdef bcdire='eta',block=11,bctype=7,start=1,1,1,end=54,1,59,
        iblock=9,istart=1,40,1,iend=54,40,59,order=1,2,3/
&bcdef bcdire='xie',block=11,bctype=7,start=54,1,1,end=54,39,59,
        iblock=12,istart=1,1,1,iend=1,39,59,order=1,2,3/
&bcdef bcdire='zta',block=11,bctype=3,start=1,1,1,end=54,39,1/
&bcdef bcdire='zta',block=11,bctype=3,start=1,1,59,end=54,39,59/

&bcdef bcdire='xie',block=3,bctype=7,start=27,1,1,end=27,40,59,
        iblock=4,istart=1,1,1,iend=1,40,59,order=1,2,3/
&bcdef bcdire='eta',block=3,bctype=7,start=1,1,1,end=27,1,59,
        iblock=12,istart=1,39,1,iend=27,39,59,order=1,2,3/
&bcdef bcdire='eta',block=3,bctype=11,start=1,40,1,end=27,40,59/
&bcdef bcdire='zta',block=3,bctype=3,start=1,1,1,end=27,40,1/
&bcdef bcdire='zta',block=3,bctype=3,start=1,1,59,end=27,40,59/

&bcdef bcdire='eta',block=12,bctype=3,start=1,1,1,end=27,1,59/
&bcdef bcdire='xie',block=12,bctype=7,start=27,1,1,end=27,39,59,
        iblock=13,istart=1,1,1,iend=1,39,59,order=1,2,3/
&bcdef bcdire='zta',block=12,bctype=3,start=1,1,1,end=27,39,1/
&bcdef bcdire='zta',block=12,bctype=3,start=1,1,59,end=27,39,59/

```

```

&bcdef bcdire='xie',block=4,bctype=7,start=27,1,1,end=27,40,59,
        iblock=5,istart=1,1,1,iend=1,40,59,order=1,2,3/
&bcdef bcdire='eta',block=4,bctype=7,start=1,1,1,end=27,1,59,
        iblock=13,istart=1,39,1,iend=27,39,59,order=1,2,3/
&bcdef bcdire='eta',block=4,bctype=11,start=1,27,1,end=27,40,59/
&bcdef bcdire='zta',block=4,bctype=3,start=1,1,1,end=27,40,1/
&bcdef bcdire='zta',block=4,bctype=3,start=1,1,59,end=27,40,59/

&bcdef bcdire='eta',block=13,bctype=3,start=1,1,1,end=27,1,59/
&bcdef bcdire='xie',block=13,bctype=7,start=27,1,1,end=27,39,59,
        iblock=14,istart=1,1,1,iend=1,39,59,order=1,2,3/
&bcdef bcdire='zta',block=13,bctype=3,start=1,1,1,end=27,39,1/
&bcdef bcdire='zta',block=13,bctype=3,start=1,1,59,end=27,39,59/

&bcdef bcdire='xie',block=5,bctype=7,start=54,1,1,end=54,40,59,
        iblock=6,istart=1,1,1,iend=1,40,59,order=1,2,3/
&bcdef bcdire='eta',block=5,bctype=7,start=1,1,1,end=54,1,59,
        iblock=14,istart=1,39,1,iend=54,39,59,order=1,2,3/
&bcdef bcdire='eta',block=5,bctype=11,start=1,40,1,end=21,40,59/
&bcdef bcdire='eta',block=5,bctype=6,start=22,40,1,end=54,40,59/
&bcdef bcdire='zta',block=5,bctype=3,start=1,1,1,end=54,40,1/
&bcdef bcdire='zta',block=5,bctype=3,start=1,1,59,end=54,40,59/

&bcdef bcdire='eta',block=14,bctype=3,start=1,1,1,end=54,1,59/
&bcdef bcdire='xie',block=14,bctype=7,start=54,1,1,end=54,39,59,
        iblock=15,istart=1,1,1,iend=1,39,59,order=1,2,3/
&bcdef bcdire='zta',block=14,bctype=3,start=1,1,1,end=54,39,1/
&bcdef bcdire='zta',block=14,bctype=3,start=1,1,59,end=54,39,59/

&bcdef bcdire='eta',block=6,bctype=7,start=1,1,1,end=27,1,59,
        iblock=15,istart=1,39,1,iend=27,39,59,order=1,2,3/
&bcdef bcdire='eta',block=6,bctype=6,start=1,40,1,end=27,40,59/
&bcdef bcdire='zta',block=6,bctype=3,start=1,1,1,end=27,40,1/
&bcdef bcdire='zta',block=6,bctype=3,start=1,1,59,end=27,40,59/

&bcdef bcdire='eta',block=15,bctype=3,start=1,1,1,end=27,1,59/
&bcdef bcdire='zta',block=15,bctype=3,start=1,1,1,end=27,39,1/
&bcdef bcdire='zta',block=15,bctype=3,start=1,1,59,end=27,39,59/

&bcdef bcdire='xie',block=7,bctype=9,start=1,1,1,end=1,20,59/
&bcdef bcdire='xie',block=7,bctype=7,start=47,1,1,end=47,20,59,
        iblock=9,istart=1,1,1,iend=1,20,59,order=1,2,3/
&bcdef bcdire='eta',block=7,bctype=3,start=1,1,1,end=47,1,59/
&bcdef bcdire='eta',block=7,bctype=3,start=1,20,1,end=47,20,59/

```



```

&bcdef bcdire='zta',block=7,bctype=3,start=1,1,1,end=47,20,1/
&bcdef bcdire='zta',block=7,bctype=3,start=1,1,59,end=47,20,59/

&bcdef bcdire='xie',block=8,bctype=7,start=1,1,1,end=1,20,59,
      iblock=9,istart=54,1,1,iend=54,20,59,order=1,2,3/
&bcdef bcdire='xie',block=8,bctype=3,start=89,1,1,end=89,20,59/
&bcdef bcdire='eta',block=8,bctype=3,start=1,1,1,end=89,1,59/
&bcdef bcdire='eta',block=8,bctype=3,start=1,20,1,end=89,20,59/
&bcdef bcdire='zta',block=8,bctype=5,start=1,1,1,end=89,20,1/
&bcdef bcdire='zta',block=8,bctype=3,start=1,1,59,end=89,20,59/

&bcdef bcdire='xie',block=9,bctype=3,start=1,21,1,end=1,40,59/
&bcdef bcdire='xie',block=9,bctype=3,start=54,21,1,end=54,40,59/
&bcdef bcdire='eta',block=9,bctype=3,start=1,1,1,end=54,1,59/
&bcdef bcdire='zta',block=9,bctype=3,start=1,1,1,end=54,40,1/
&bcdef bcdire='zta',block=9,bctype=3,start=1,1,59,end=54,40,59/

&bcdef bcdire='end'/

&bcwake wbcdir='eta',wblock=11,wface=1,wbctype=0/
&bcwake wbcdir='eta',wblock=1,wface=2,wbctype=0/
&bcwake wbcdir='end'/

```

Note: Boundary conditions

- 1 zero gradient
- 2 supersonic inflow
- 3 no slip adiabatic wall boundary
- 4 zero gradient with $w = 0$
- 5 subsonic outflow, fixed static pressure (poutlet in datain)
- 6 subsonic inflow, fixed ρ , u , v , w at inlet
- 7 inner boundary for mpi
- 8 symmetry boundary
- 9 subsonic inlet BC with fixed total pressure and temperature
- 10 periodic boundary condition
- 11 subsonic outflow, fixed static pressure (computed in code)
- 20 periodic boundary condition for flow variables only

B.2 *init.input* File

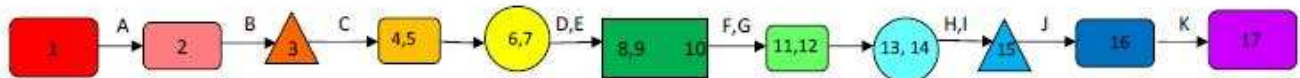
```

200          !bc_max  the maximum of the BCs number defined in problem
15          !nb  the total number of blocks
27,40,59    !il,jl,kl  the density of the grid of each block
54,40,59    !il,jl,kl  the density of the grid of each block
27,40,59    !il,jl,kl  the density of the grid of each block
27,40,59    !il,jl,kl  the density of the grid of each block
54,40,59    !il,jl,kl  the density of the grid of each block
27,40,59    !il,jl,kl  the density of the grid of each block
47,20,59    !il,jl,kl  the density of the grid of each block
89,20,59    !il,jl,kl  the density of the grid of each block
54,40,59    !il,jl,kl  the density of the grid of each block
27,39,59    !il,jl,kl  the density of the grid of each block
54,39,59    !il,jl,kl  the density of the grid of each block
27,39,59    !il,jl,kl  the density of the grid of each block
27,39,59    !il,jl,kl  the density of the grid of each block
54,39,59    !il,jl,kl  the density of the grid of each block
27,39,59    !il,jl,kl  the density of the grid of each block
2          !The number of additional poutlet condition
7,1,66.4000,70.2000,0.81248  !The block number,flow direction (for bctype=9)
8,1,66.4000,70.2000,0.81248  !The block number,poutlet,ptotal and tttotal

```

Appendix C

Flowchart for Lab Equipment, Piping, and Sensors



1. Ingersoll Rand UP6-15cTAS-150 Compressor
2. 2000 gal. high pressure tank
3. Koso Hammel Dahl electro-pneumatic control valve
4. ¼ NPT tap for Spectre Sensors Model 1500 (0-80 psia) Pressure and Temperature Transducer
5. Devar SM815 Isolated T/C Transmitter
6. Oripac Model 5300 2" orifice plate
7. Spectre Sensors Model D150 Differential Pressure Transducer (0-267.7" WCD)
8. Injection cavity of airfoil in test section, Spectre Sensors Model 1500 (0-80 psia) Pressure and Temperature Transducer
9. Devar SM815 Isolated T/C Transmitter
10. Suction cavity of airfoil in test section, Spectre Sensors Model 1500 (0-29.5" HGV) Pressure and Temperature Transducer, only pressure is used
11. ¼ NPT tap for Spectre Sensors Model 1500 (0-29.5" HGV) Pressure and Temperature Transducer
12. Devar SM815 Isolated T/C Transmitter
13. Oripac Model 5300 4" orifice plate
14. Spectre Sensors Model D150 Differential Pressure Transducer (0-116.9" H₂O)
15. Manual gate valve
16. 600 gal. vacuum tank
17. 60 HP Dekker V-Max vacuum system
- A. ¾" pipe out of compressor to 3" pipe into 2000 gal. tank
- B. 3" out of tank to 2" into electro-pneumatic control valve
- C. 2" pipe, 20" of straight pipe before orifice plate
- D. 2" pipe, 10 " straight pipe after orifice plate
- E. Decrease to 1" pipe for injection hook-up on wind tunnel box
- F. 3" pipe out of suction hook-up on wind tunnel box to 4" for flow measurement
- G. 40" straight pipe before orifice plate
- H. 20" straight pipe after orifice plate
- I. 4" pipe decreased to 3" for gate valve
- J. 3" out of gate valve increased to 4" for 600 gal. tank
- K. 4" out of tank increased to 5" to vacuum pump

Appendix D

CFJ Wind Tunnel Laboratory

Testing Procedure

The following procedure describes how to conduct a wind tunnel experiment and collect data. During all testing, or for any wind tunnel work, please use caution with all equipment and common sense. NEVER stand at the outlet of the wind tunnel while it is running and NEVER use your hand or any other item to check high pressure flow from the tank or the strength of the vacuum. Both machines are powerful and any debris in the line could cause injury. Read the entire procedure before beginning a test.

1. Make sure that the wind tunnel lab doors are closed.
2. With all parts of the model securely in place, loosen the 4 set screws around the sting coupler on the endplate of the airfoil.
3. Lead the thermocouple wire and injection cavity tube through the hole in the wind tunnel wall and slide airfoil over sting extrusion. Rotate inner and outer circle until airfoil locks in place with grooves. Rotate to desired AoA.
4. Tighten the 4 set screws evenly until the airfoil is snug in place and does not rotate about the sting. Insure that the screws connecting the sting to the balance and the balance to the back plate are secure. Tighten the screws for the sting support.
5. Make sure thermocouple wire and pressure probe are connected properly to the sensors inside of the box.
6. Measure the AoA of the airfoil at the flat part of the endplate from the inside of the box. Also, measure the flat part of the square flange on the back plate.

Record each of these values in the front panel of the Labview program as "AoA" and "Bplate angle". The back plate angle will have to be input again in the data sheet produced after the data is collected.

7. Connect suction manifold and tubing to suction opening in the endplate and seal with electrical tape.
8. Close doors to the box and seal with electrical tape.
9. Close test section door and secure with spring clamps.
10. For CFJ tests, open valve at 2000 gal. tank exit half way. Make sure gate valve in the suction line is open. Open small valve with yellow handle that leads to the pneumatic chamber of the computer controlled valve. Make sure vacuum is reset by pushing the "Alarm Condition Reset" button.
11. On program front panel, enter airfoil geometry and ambient pressure and temperature read from barometer.
12. Zero balance using "Zero forces" button on front panel. Zero MKS differential pressure transducer.
13. Select sample rate frequency and test duration time on front panel
NOTE: Baseline tests will only use force balance data, so the computer controlled valve and vacuum will not be used. Steps 14-20 are for baseline testing only.
14. **DOUBLE CHECK THAT EVERYTHING IS SECURE AND NO STEP HAS BEEN OVERLOOKED!!**
15. To begin test, increase wind tunnel frequency to 3 Hz and click "Start" in the Tunnel Fan Control box on the front panel. At any point if something goes wrong, click the "Stop" immediately. The wind tunnel can also be turned off at the key pad next to the test section.
16. Slowly increase the frequency, using arrow keys, until desired wind tunnel speed is reached. This can be viewed on the front panel. At high angles, the airfoil can oscillate very violently. Please use your discretion whether to continue the test. If the fluctuations are extreme, the airfoil is probably stalled. Turn off the wind tunnel and check that everything is secured properly.
17. Once the desired speed is reached, click "Start" in the Data Collection box on the front panel. The timer will begin to count down the testing time.
18. **NEVER LEAVE TEST STAND WHILE EXPERIMENT IS RUNNING! BE READY TO CLICK STOP IN CASE OF A PROBLEM!**
19. Once the time is up, click "Stop" to turn off the wind tunnel fan.

20. The data collected from the current test will pop up in an excel spread sheet. Enter the back plate angle on the first page of the data sheet in the appropriate cell. The data template has already done all of the calculations necessary and the final results of aerodynamic coefficients and all other data collected is in the file.
21. For CFJ tests, adjust values in the Sensor Offsets box on the front panel until the ambient pressure is reached for the pressure sensors and the differential pressure sensors read zero. Ambient pressure is found with the barometer.
22. Use ear protection while equipment is running.
23. DOUBLE CHECK THAT EVERYTHING IS SECURE AND NO STEP HAS BEEN OVERLOOKED!!
24. Make sure toggle in the Injection Flow Control box is set to MANUAL and "Injection MFR Setpoint" is set to 0.0400.
25. To begin test, increase wind tunnel frequency to 3 Hz and click "Start" in the Tunnel Fan Control box on the front panel. At any point if something goes wrong, click the "Stop" immediately. The wind tunnel can also be turned off at the key pad next to the test section.
26. Slowly increase the frequency, using arrow keys, to about 10 Hz.
27. To begin CFJ test, set "Control Valve Volts" to 3.000 V and click start. This will open the computer controlled valve. If airfoil vibrates violently, click "Stop" and turn off the wind tunnel. Then check to see that the model is secure.
28. MAKE SURE "INJECTION MFR SETPOINT" IS 0.0400, if the flow rate is too high the valve will open too fast and there can be a ram effect of air entering the airfoil. This could cause damage to the model or the wind tunnel.
29. With "Injection MFR Setpoint" at 0.0400, switch the toggle to "Auto". Now the valve is operating based on the input of the desired mass flow rate in the injection line.
30. MAKE SURE the cursor is between the hundredths and thousandths place so that the flow rate will increase in increments of 0.01. Use arrow keys to SLOWLY ramp up the injection mass flow rate and open the valve.
31. When the mass flow rate reaches about 0.07 kg/s, have another person turn on the vacuum by pushing the "Start" button on the vacuum. The vacuum will be very loud. The vacuum operator should stay near the vacuum to turn it off in case of a problem. Also, they will adjust the gate valve for the suction flow rate.

32. Continue increasing mass flow rate in increments of 0.01 kg/s and increase the wind tunnel frequency slowly. Keep a watch on the model to make sure everything is in place and that it doesn't flutter violently.
33. Increase mass flow rate slowly until desired MFR is reached.
34. Use the arrow sign to signal to the vacuum operator to open or close the valve. Clockwise closes the valve and decreases mass flow. Counter-clockwise opens the valve and increases mass flow. Adjust the valve slowly. NEVER CLOSE VALVE COMPLETELY!
35. Use the "MFR actual" reading on the front panel and on the second screen to read mass flow rates. Adjust suction valve until the injection and suction mass flow rate match within 5% of each other.
36. Once mass flow rates are matched at the desired testing level and the wind tunnel velocity is at the speed required, click "Start" in the Data Collection Box on the front panel. The timer will begin to count down the testing time.
37. NEVER LEAVE TEST STAND WHILE EXPERIMENT IS RUNNING! BE READY TO CLICK STOP IN CASE OF A PROBLEM!
38. Once the time is up, turn the vacuum off by pressing "Stop" on the vacuum. Turn off the injection air by clicking "Stop" in the Injection Flow Control box on the front panel. Turn off the wind tunnel by clicking "Stop" in the Tunnel Fan Control box on the front panel.
39. The data collected from the current test will pop up in an excel spread sheet. Enter the back plate angle on the first page of the data sheet in the appropriate cell. The data template has already done all of the calculations necessary and the final results of aerodynamic coefficients and all other data collected is in the file.

Appendix E

Wind Tunnel Equipment Operation and Maintenance

E.0.1 Compressor: *Ingersoll Rand UP6-15c TAS-150*

Operation:

1. Make sure electrical breaker is on
2. Check to ensure that all valves are in the correct position, depending on which part of the system you want to supply air to.
3. Open black panel with supplied keys. Adjust valve shown below from constant operation to start-stop operation.



-Valve Open= Constant fill (pump will constantly run until max pressures are held, then air will discharge from valve if system is closed)

-Valve Closed= Automatic start-stop (pump will turn on when tank reaches 125 psi, and stop when it reaches 150 psi) The yellow light indicates automatic operation, meaning pump can turn on at any time

*Notes:

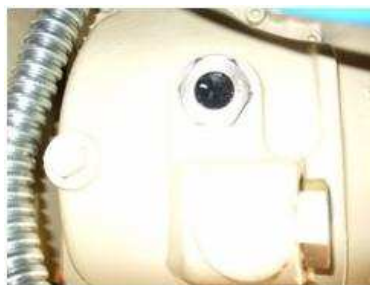
1. Check Red/Green/Blue indicator - Red = Pump off - Green = Pump on - Blue = Dryer has frozen/ too cold (Turn off equipment and call Arle Compressors)
2. Expect 4 psi less when running the pump constantly then with start-stop operation

Maintenance:

1. Change oil filter below after 150 hr. the 1st time using replacement filter provided. After the 1st time, change oil filter every 3000 hrs.



2. Check oil thru small glass, shown here, when compressor is off. If oil is low in the window, add special oil that can be purchased at Arle Compressors. DO NOT USE ANY OTHER OIL!



3. Change oil every 9000 hrs, or once a year. Open lower bolt to drain, add oil same as above.
4. Change air filter (left of figure below) every 3000 hrs.
5. Change separator (right of figure below) every 3000 hrs.



6. Warranty: 1 year for parts, 2 years for pump. Warranty began 9/16/08.

*Notes: - All accessories, oil, filters, etc should be purchased at Arle Compressors

E.0.2 Vacuum: *Dekker V-max 60 HP VMX1003K*

Operation:

1. Make sure system is open, otherwise vacuum will be reached very quickly and the motor will begin to over-heat.
2. Turn on breaker
3. Open Manual gate valve about half way, about 2 turns. Do not fully open valve until system is running.
4. Turn on vacuum via start button
5. Check pressure gauge on tank and on vacuum, they should be similar.
6. Alarm for high temperature may go off in the beginning. Turn off alarm with alarm button.
7. Temperature should always be between $140^{\circ}F - 180^{\circ}F$. If temperature exceeds this and begins to climb to $200^{\circ}F$, turn off system and let the vacuum cool down. Check that system is fully open. If high temperature persists, contact Arle Compressors. **If temperature becomes too high, the vacuum motor will trip and will have to be reset, try to avoid this through constant observation of temperature gauge.*

Maintenance:

1. Clean oil filter every 3000 hr. Shut down equipment. Make sure both valves are closed around filter. Take out and clean with mineral spirits. This filter is just cleaned, not replaced. Filter is located as shown in the figure below.
2. The separator is located in the tank. Check the gauge, green = good operation, red = poor operation. Contact Arle if gauge is red.



3. Check inlet filter after the 1st 8 hrs, then every 500 hrs. Shut down equipment. If a new one is needed, contact Arle Compressors for purchase. **If there is a difference in pressure from the tank to the vacuum, then the inlet filter is probably dirty.*
4. Make sure oil is at center line when equipment is off. Only add special oil from Arle Compressors. Fill where yellow decal is located. See figure below.



5. Change oil every 10,000 hrs. Only use designated oil from Arle Compressors.
6. Check oil pressure gauge, it should be near 20, if the pressure becomes too low, contact Arle for service. Pressure gauge shown below.



For any other matters, questions, or for more detail, please refer to the service manuals for the compressor and vacuum, located in the lab.

Appendix F

List of Vendors

1. AMTI: 6-Component Force Balance
Tony Lima
Sales Order & Production Coordinator
176 Waltham Street
Watertown, MA 02472
Tel: (617) 926-6700 ext. 342
Fax: (617) 926-5045
E-mail: tonyl@amtimail.com
2. Arle Compressors: Ingersoll Rand UP6-15c TAS-150 Compressor, 2000 gal. tank, 600 gal. tank, Dekker Vacuum Pump
Robert P. Geiger
Ingersoll Rand - Arle Compressor Systems Corp.
10650 N.W. South River Drive
Medley, FL 33178
Phone: 305-888-8978 ext. 211
Fax: 305-88209122
3. Cypress Tools Corporation: CNC machined aluminum wall and wind tunnel box parts
Juan Seoane
305.318.6625
jcseoane@bellsouth.net
4. Engineering Laboratory Design, Inc.: 24" Open Circuit Wind Tunnel
P.O. Box 278, 2021 South Highway 61

Lake City Minnesota 55041
 800-795-8536
 Fax 651-345-5095
www.elding.com

5. ERG Materials and Aerospace Corporation: Duocel Aluminum Foam
 Garrick Bornkamp, Design Engineer
 ERG Materials and Aerospace Corporation
 900 Stanford Avenue
 Oakland, CA 94608
 Phone: (510) 658-9785 FAX: (510) 658-7428
GBornkamp@ergaerospace.com
www.ergaerospace.com

6. FlowKenetics: pitot and kiel probes
 528 Helena St.
 Bryan, TX 77801
 979-680-0659

7. Koso Hammel Dahl Control Valves: IMO-G110-1 computer controlled valve
 Koso America, Inc.
 4 Manley St.
 West Bridgewater, MA 02379
 phone: 508.584.1199, fax: 508.584.2525

8. Lambda Square: Orifice Plates
 71 Deer Park Ave.
 Babylon, NY 11702
 631-587-1000

9. McMaster-Carr Supplier: all fasteners, hoses and connectors, tubes, 0.012" stainless shims, piping couplers, gate valve, all other miscellaneous lab equipment
www.mcmaster.com

10. National Instruments: SC-2345, all signal conditioning modules, PCI-6229
 National Instruments Sales Office
 11500 N Mopac Expwy.
 Austin, TX 78759-3504 U.S.A
 Tel: 512-683-0100 Fax: 512-683-5794

11. Precision Design and Automation, Labview Programmer
Mark Schmitt
561-322-9433 (cell)
msschmitt@comcast.net

12. ProCo: all Spectre Sensors, Devar thermocouple transmitters, DC power supply
J.C. Rabuini
Manager South Florida Region
PRO-CO Inc. - www.pro-co.com
MIAMI OFFICE MAIN OFFICE
O: 305.207.3678 O: 407.830.6969
C: 305.968.6969 F: 407.830.6011
F: 305.207.3679
JCrabuini@pro-co.com

13. SolidConcepts: CNC machined and SLA airfoil model parts
Scott Lubell
Sr. Project Engineer
28309 Avenue Crocker
Valencia, CA 91355
Tel 661-295-4418
Fax 661-257-9311

Appendix G

Drawings for Airfoil Model and Wind Tunnel Modifications

All part drawings are included in a supplementary CD.

References

- [1] F. C. Kelly, *The Wright Brothers: A Biography Authorized by Orville Wright*. Dover Publications, 1943, re-published in 1989.
- [2] G.-C. Zha and C. Paxton, “A Novel Airfoil Circulation Augment Flow Control Method Using Co-Flow Jet.” AIAA Paper 2004-2208, 2004.
- [3] G.-C. Zha, C. D. Paxton, and C. A. Conley, “Effect of Injection Slot Size on the Performance of Coflow Jet Airfoil,” *Journal of Aircraft*, vol. 43, pp. 987–995, 2006.
- [4] G.-C. Zha and C. D. Paxton, “Novel Flow Control Method for Airfoil Performance Enhancement Using Co-Flow Jet,” *Applications of Circulation Control Technologies, AIAA Book Series, Progress in Aeronautics and Astronautics*, vol. 214, pp. Chapter 10, p. 293–314, 2006.
- [5] G.-C. Zha, B. F. Carroll, C. Paxton, C. A. Conley, and A. Wells, “High-Performance Airfoil Using Coflow Jet Flow Control,” *AIAA Journal*, vol. 45, No. 8, pp. 2087–2090, 2007.
- [6] G.-C. Zha, W. Gao, and C. D. Paxton, “Jet Effects on Coflow Jet Airfoil Performance,” *AIAA Journal*, vol. 45, No. 6, pp. 1222–1231, 2007.
- [7] G.-C. Zha and W. Gao, “Analysis of jet effect on co-flow jet airfoil performance with integrated propulsion system.” AIAA Paper 2006-0102, 2006.
- [8] G.-C. Zha, B. F. Carroll, C. Paxton, C. A. Conley, and A. Wells, “High performance airfoil using co-flow jet flow control.” AIAA Paper 2005-1260, 2005.
- [9] G.-C. Zha, W. Gao, and C. Paxton, “Numerical simulation of co-flow jet airfoil flows.” AIAA Paper 2006-1060, 2006.
- [10] R. J. Englar, “Circulation Control for High Lift and Drag Generation on STOL Aircraft,” *Journal of Aircraft*, vol. 12, No. 5, pp. 457–463, 1975.
- [11] A. J. Wells, “Experimental Investigation of An Airfoil with Co-Flow Jet Flow Control,” Master’s thesis, University of Florida, 2005.
- [12] Y.-Q. Shen and G.-C. Zha, “Improvement of the WENO Scheme Smoothness Estimator,” *International Journal for Numerical Methods in Fluids*, 2009.

- [13] Y.-Q. Shen, G.-C. Zha, and B.-Y. Wang, "Improvement of Stability and Accuracy of Implicit WENO Scheme," *AIAA Journal*, vol. 47 No. 2, pp. 331–344, 2009.
- [14] B.-Y. Wang and G.-C. Zha, "A General Sub-Domain Boundary Mapping Procedure For Structured Grid CFD Parallel Computation," *AIAA Journal of Aerospace Computing, Information, and Communication*, vol. 5 No. 11, pp. 425–447, 2008.
- [15] X. Chen and G.-C. Zha, "Implicit Application of Non-Reflective Boundary Conditions for Navier-Stokes Equations in Generalized Coordinates," *International Journal for Numerical Methods in Fluids*, vol. 50 No. 7, pp. 767–793, 2006.
- [16] X. Chen and G.-C. Zha, "Fully Coupled Fluid-Structural Interactions Using an Efficient High Solution Upwind Scheme," *Journal of Fluid and Structure*, vol. 20 No. 8, pp. 1105–1125, 2005.
- [17] X. Chen and G.-C. Zha, "Fully Coupled Fluid-Structural Interactions Using an Efficient High Solution Upwind Scheme," *Journal of Fluid and Structure*, vol. 20 No. 8, pp. 1105–1125, 2005.
- [18] G.-C. Zha, "A Low Diffusion Efficient Upwind Scheme," *AIAA Journal*, vol. Vol.43, No.5, pp. 1137–1140, 2005.
- [19] Z. Hu and G.-C. Zha, "Calculations of 3D Compressible Using an Efficient Low Diffusion Upwind Scheme," *International Journal for Numerical Methods in Fluids*, vol. Vol.47, pp. 253–269, 2004.
- [20] G.-C. Zha, "Boundary Layer Loss Mechanism and Justification of Wall Functions for Turbulence Modeling," *AIAA Journal*, vol. Vol.42 No. 11, pp. 2387–2390, 2004.
- [21] Y. Shen and G.-C. Zha, "Simulation of flows at all speeds with high- order weno schemes and preconditioning." AIAA Paper 2009-1312, 2009.
- [22] Y. Shen and G.-C. Zha, "High order finite differencing schemes and their accuracy for cfd." AIAA Paper 2009-1137, 2009.
- [23] B. Wang and G.-C. Zha, "Comparison of a low diffusion e-cusp and the roe scheme for rans calculation." AIAA Paper 2008-0596, 2008.
- [24] B.-Y. Wang, B. Haddoukessouni, J. Levy, and G.-C. Zha, "Numerical Investigations of Injection Slot Size Effect on the Performance of Co-Flow Jet Airfoil," *AIAA Journal of Aircraft*, vol. Vol.45 No. 6, pp. 2084–2091, 2008.
- [25] I. H. Abbott and A. E. V. Doenhoff, *Theory of Wing Sections*. Dover Publications, Inc., 1959.
- [26] J. Aguirre, "Study of 3-dimensional co-flow jet airplane and high-rise building flow using cfd simulation," Master's thesis, University of Miami, 2008.

- [27] G.-C. Zha, “Computational fluid dynamics class notes.” MEN 614, Department of Mechanical and Aerospace Engineering, University of Miami, Spring 2007.
- [28] K. A. Hoffmann and S. T. Chiang, *Computational Fluid Dynamics Volume 1, 4th Edition*. Engineering Education System, 2004.
- [29] D. E. Simanek, “Error analysis (non-calculus),” 1996.
<http://www.lhup.edu/~dsimanek/errors.htm>.
- [30] F. L. H. Wolfs, “Error analysis.”
http://teacher.nsr1.rochester.edu/Phy_labs/AppendixB/AppendixB.html.